**CENTRO DE INVESTIGACIÓN Y DE ESTUDIOS AVANZADOS
DEL INSTITUTO POLITÉCNICO NACIONAL**

UNIDAD MÉRIDA
DEPARTAMENTO DE FÍSICA APLICADA

First principles study of the electron-phonon interaction in superconducting intermetallic alloys

A Dissertation by

Omar De la Peña Seaman

Submitted in partial fulfillment of
the requirements for the degree of

Doctor of Philosophy

in the specialty of

Theoretical Physics

Advisors

Dr. Romeo Humberto de Coss Gómez

Dr. Klaus-Peter Bohnen

Mérida, Yucatán, México   January 2008

**CENTRO DE INVESTIGACIÓN Y DE ESTUDIOS AVANZADOS
DEL INSTITUTO POLITÉCNICO NACIONAL**

UNIDAD MÉRIDA
DEPARTAMENTO DE FÍSICA APLICADA

Estudio de primeros principios de la interacción electrón-fonón en aleaciones intermetálicas superconductoras

Tesis que presenta

Omar De la Peña Seaman

para obtener el Grado de

Doctor en Ciencias

en la especialidad de

Física Teórica

Director de Tesis

Dr. Romeo Humberto de Coss Gómez

Dr. Klaus-Peter Bohnen

Mérida, Yucatán, México   Enero de 2008

J.V.R.L.
M.E.S.R.
C.D.C.
R.C.G.
K.-P.B.
R.H.

Acknowledgments

Agradecimientos

ABSTRACT

We have studied two different superconducting intermetallic alloy systems, the first is the $Nb_{1-x}Mo_x$ binary alloy, and the second system corresponds to MgB_2 doped with Al on Mg-site and C on B-site, giving as a result the $Mg_{1-x}Al_xB_2$ and $MgB_{2(1-x)}C_{2x}$ ternary alloys. We have calculated the structural, electronic, vibrational, electron-phonon and superconducting properties of these systems within the framework of the density functional theory using the self-consistent virtual-crystal approximation (VCA). For the three studied alloys, the structural properties, electronic band structure, and selected high-symmetry phonon frequencies have been calculated for a large number of concentrations, comparing two implementations of the VCA in the all-electron (LAPW) and the pseudopotential (MBPP) method. The complete phonon dispersion, electron-phonon and superconducting properties of these alloys where obtained within the framework of density functional perturbation theory using the MBPP method. For the Nb-Mo alloy, we found very good agreement between both methodologies for all the calculated properties, independent of the approximation used for the exchange-correlation functional (LDA and GGA). We identified an electronic topological transition for this alloy at around 30% of Mo-content. The calculated phonon dispersions bands as a function of x are in good agreement with the experimental data. For the Eliashberg function $\alpha^2F(\omega)$, we found a shift of weight to higher frequencies as well as an overall reduction with increasing x up to $x \approx 0.7$, however for $x = 1$ (pure Mo) the spectral weight for $\alpha^2F(\omega)$ increases again. The evolution of the electron-phonon average coupling strength $\lambda(x)$ closely follows the variation of the electronic density of states at E_F. All experimental values of the superconducting critical temperature $T_c(x)$ were well reproduced using a proper interpolation scheme for the Coulomb pseudopotential $\mu^*(x)$. For all the calculated properties, we found good agreement with experimental results, indicating the applicability of the VCA on $Nb_{1-x}Mo_x$. According to the other systems studied in this thesis, from previous works in the past it is well known that the harmonic calculations of the full phonon dispersion for MgB_2 are in very good agreement with measurements, suggesting that the anharmonic effects are not very crucial for the MgB_2-based alloy systems. From the analysis of the full phonon dispersion evolution as a function of x, we found strong renormalization of the E_{2g}-phonon mode for both Al- and C-doped MgB_2, and also a strong reduction of the E_{2g}-band dispersion with the filling of the σ-band was observed. For both systems, $\alpha^2F(\omega)$ and λ were calculated applying the two band model (σ,π) for several concentrations. Using $\alpha_{ij}^2F(\omega)$ and a diagonal expression for $\mu^*(\omega_c)$, we solved the Eliashberg gap equations in the two band model neglecting interband scattering $\Gamma_{\sigma\pi}$. We found good agreement of $\Delta_\sigma(x)$, $\Delta_\pi(x)$, and $T_c(x)$ with experimental data and no gap merging at any x is predicted. Based on those results, we may say that $\Gamma_{\sigma\pi}$, if present, is small and their effects on the reduction of T_c in the $Mg_{1-x}Al_xB_2$ and $MgB_{2(1-x)}C_{2x}$ systems are negligible and masked by the σ-band filling effect.

RESUMEN

Hemos estudiado dos diferentes sistemas de aleaciones intermetálicas superconductoras, la aleación binaria $Nb_{1-x}Mo_x$ y un sistema que corresponde a aleaciones ternarias basadas en MgB_2: $Mg_{1-x}Al_xB_2$ y $MgB_{2(1-x)}C_{2x}$. Se han calculado las propiedades estructurales, electrónicas, vibracionales, de acoplamiento electrón-fonón y superconductoras de estas aleaciones dentro del marco de la teoría del funcional de la densidad usando la aproximación auto-consistente del cristal virtual (VCA). Para los tres sistemas, los parámetros estructurales, la estructura electrónica y las frecuencias fonónicas en puntos de alta simetría han sido calculados para varias x, comparando las implementaciones de VCA en el método de todos los electrones (LAPW) y el de pseudopotenciales (MBPP). Las bandas completas de dispersión fonónicas, el acoplamiento electrón-fonón y las propiedades superconductoras fueron obtenidas dentro del marco de la teoría perturbativa del funcional de la densidad en el método de pseudopotenciales. En el sistema Nb-Mo encontramos en muy buen acuerdo entre ambos métodos en todas las propiedades calculadas, independientemente de la aproximación usada para el funcional de intercambio-correlación (xc), LDA o GGA. Identificamos una transición topológica electrónica en una concentración crítica de $\approx 30\%$ de Mo. Las bandas de dispersión fonónicas calculadas como función de x están en buen acuerdo con datos experimentales. Para la función de Eliashberg $\alpha^2 F(\omega)$ encontramos un corrimiento del espectro a frecuencias mayores así como también una reducción generalizada conforme se incrementa x hasta $x \approx 0.7$, incrementándose ligeramente para $x = 1$ (Mo). La evolución de la constante de acoplamiento $\lambda(x)$ sigue muy de cerca el comportamiento de la densidad de estados al nivel de Fermi $N(E_F)$. Los valores experimentales y la tendencia de $T_c(x)$ son reproducidos por los cálculos utilizando un esquema de interpolación adecuado para el potencial Coulómbico $\mu^*(x)$. Para todas las propiedades calculadas, encontramos en general muy buen acuerdo con datos experimentales, indicando la aplicabilidad del VCA en $Nb_{1-x}Mo_x$. En las aleaciones basadas en el MgB_2 (con Al y C), obtuvimos las bandas de dispersión fonónicas armónicas para diferentes concentraciones. Comparando el cálculo del MgB_2 con datos experimentales encontramos muy buen acuerdo, indicando que los efectos anarmónicos no juegan un papel importante en este material. Del análisis de la evolución de las bandas fonónicas en función de x se observa una fuerte reducción de la dispersión de la banda relacionada con el modo E_{2g} a medida que la banda σ se va saturando. Para ambos sistemas, $\alpha^2 F(\omega)$ y λ se calcularon aplicando el modelo de dos bandas σ y π. Usando $\alpha_{ij}^2 F(\omega)$ y una expresión de matriz diagonal para $\mu^*(\omega_c)$, resolvimos las ecuaciones de Eliashberg para la brecha superconductora en el modelo de dos bandas sin considerar el término de dispersión interbandas $\Gamma_{\sigma\pi}$. Encontramos muy buen acuerdo de $\Delta_\sigma(x)$, $\Delta_\pi(x)$, t $T_c(x)$ calculados con resultados experimentales, además de no observar el colapso de las dos brechas a ninguna x en ambos casos. Por tanto, se puede decir que $\Gamma_{\sigma\pi}$ en caso de estar presente, es pequeño y sus efectos en la reducción de las brechas y T_c en $Mg_{1-x}Al_xB_2$ y $MgB_{2(1-x)}C_{2x}$ son despreciables y encubiertos por el efecto del llenado de la banda σ.

Contents

Introduction

The effects of the electron-phonon interaction in metals are evident in many quantities that could be measured from experiments. Just to mention some of them, it contributes to thermal and electrical resistivities, it also generate the enhancement of the effective electron mass as measured in the electronic heat capacity, and additionally, plays an important role in superconductivity. Specifically for the last mentioned, within the Eliashberg theory the superconducting temperature T_c, among other properties, depend just on two quantities, the Coulomb pseudopotential μ^* and the Eliashberg or electron-phonon spectral function $\alpha^2 F(\omega)$ [1–4]. This quantity basically measures the effectiveness of phonons of energy $\hbar\omega$ to scatter electrons from one part of the Fermi surface to another.

The electron-phonon coupling could be obtained by tunneling measurements across metal-insulator-superconductor junctions [5]. Structure in the tunneling conductance reflects structure in the superconducting gap function that arises from the interaction between electrons and phonons. Applying a tunneling inversion procedure, the McMillan-Rowell scheme [6] that consists in solving iteratively the Eliashberg equations, an $\alpha^2 F(\omega)$ is obtained that accurately reproduces the measured tunneling conductance. Nevertheless, this method is not always applicable to all systems, particularly to those for which junction construction is difficult and also systems where the coupling is so weak that the phonon structure in the tunneling data is complicated to extract [5].

The usefulness of the simulation approach, enters then at this point, since it can help to analyze and study systems and materials where experimental data are limited or difficult to extract. First principles calculations can provide useful information about the electron-phonon coupling, but the knowledge of the electronic excitation spectra, the full-phonon dispersion, and the self-consistent response of the electronic system to lattice vibrations is needed. Recently, the linear response theory within the framework of density functional theory [7,8] has shown to be a powerful method for calculating lattice dynamical properties and electron-phonon coupling parameters in solids [9,10]. Superconducting metals for which good tunneling data are available have been used as test cases for demonstrating the accuracy of the method [11,12].

Nevertheless, for the case of alloys, there is not too much information in the literature, especially from the theoretical point of view, neither for the vibrational nor the electron-phonon coupling properties. For example the $Nb_{1-x}Mo_x$ alloy, a very widely studied system from the experimental point of view, presents non-monotonic behavior for T_c and the phonon frequency at the high symmetry points in the Brillouin zone, as a function of Mo-content [13–18]. The origins of these features is not yet completely understood despite of the efforts to study the alloy theoretically. This is due in part to the lack of a suitable and computationally non-expensive approximation to study the evolution of different properties as a function of concentration, without losing information such as the crystal structure or symmetry, among others. For example, the evolution of the electronic and elastic properties of the $Nb_{1-x}Mo_x$ alloy as a function of x has been studied using quasi-random structures [19], the coherent potential approximation (CPA) [20–22], and the Korringa-Kohn-Rostoker coherent potential approximation (KKR-CPA) [23, 24] approaches. However, these studies have been limited to only a few Mo concentrations, because these calculations are very difficult to interpret and computationally very demanding, especially if one is interested in very low (close to Nb) or high concentrations (close to Mo). Thus, the $Nb_{1-x}Mo_x$ system is a perfect case to test the applicability of a different approach, the self-consistent virtual-crystal approximation [25–29], and it's usefulness on the calculation of vibrational properties, electron-phonon coupling, and superconductivity.

Another interesting and widely studied system, because of it's superconducting properties observed in 2001, is MgB_2 and related alloys. The intermetallic compound MgB_2 has a $T_c \approx 39$ K [30] and it is now generally accepted as a phonon-mediated BCS/Eliashberg superconductor with multiple gaps and strong electron-phonon (e-ph) coupling. The coupling takes place mainly between the σ Fermi surface sheets, coming from the boron $p_x - p_y$ orbitals, with one specific type of phonon, the B-B bond stretching modes with E_{2g} symmetry at the Γ point [31–34]. As soon as MgB_2 was discovered as a superconductor material, the scientific community started to search for a possible family of superconductors related to this compound. The first studies in this direction were the substitution of constitutive elements by other similar ones, such as Mg by Al and B by C, giving rise to the $Mg_{1-x}Al_xB_2$ [35–38] and the $MgB_{2(1-x)}C_{2x}$ [39–43] alloys, respectively. The superconducting properties of the alloys, like e-ph coupling and T_c, are influenced by doping in several ways, due to the change in the electronic structure that has direct impact on them through, for example, the change in the electronic density of states. The result is a reduction of the e-ph coupling, T_c, and the superconducting gaps, among other quantities, as a function of Al or C-content [35–51]. Further, the change in the e-ph coupling also influences the phonon properties, like the renormalization of the E_{2g} phonon frequency in

$Mg_{1-x}Al_xB_2$, that has been demonstrated by Raman scattering measurements, which was found a frequency increment (hardening) as a function of x, from ≈ 73 meV for MgB_2 until 123 meV in AlB_2 [32,52,53]. In the case of the C-doped system, unfortunately so far there are no frequency measurements (neither Raman nor IXS) available as a function of x.

The main aim of this thesis was to study the electron-phonon coupling and superconducting properties of the $Nb_{1-x}Mo_x$, $Mg_{1-x}Al_xB_2$, and $MgB_{2(1-x)}C_{2x}$ alloys by means of first principles calculations, using for this purpose the self-consistent virtual-crystal approximation for the simulation of the alloy systems. We also performed calculations of the structural, electronic, and vibrational properties for each concentration (x), since they represent the required input data for the calculations of the e-ph coupling and superconducting properties. The evolution of the studied properties is analyzed as a function of x, and the effects of the electronic topological transitions on vibrational and superconducting properties are also discussed.

For this computational study we used numerical calculations within the framework of density functional theory (DFT) [7,8] using the self-consistent virtual-crystal approximation (VCA) [25–29]. We performed the calculations of the structural, electronic and some frequencies at high symmetry points in the Brillouin zone, using the full-potential linearized augmented plane-wave method (LAPW) [54–56] as implemented in the Wien2k code [57] for which the VCA has already been tested previously [26–29]. In addition, we investigated the same properties using our implementation of the VCA within the mixed-basis pseudopotential (MBPP) method [58]. The current MBPP code incorporates an implementation of the very efficient linear response [9,32,59–61] approach to lattice dynamical properties, which is currently not available in the Wien2k code. Thus, vibrational properties as well as the electron-phonon coupling were obtained with the linear response theory. Finally, superconductivity is discussed within the framework of the Eliashberg theory in the cases of one and two bands(or gaps) models [10,31,62–64].

The thesis is organized in the following way: Chapter 1 reviews briefly the main ideas of the density functional theory, and also the LAPW and MBPP methods, for the solution of the Kohn-Sham equations. Additionally, an explanation of the virtual-crystal approximation is presented. Chapter 2 is devoted to the description of the perturbative density functional theory, which relies on the linear response theory approach for the calculation of vibrational properties. It also includes a section devoted to the Eliashberg theory, the electron-phonon coupling, and superconductivity, and how they are applied in the present calculations. The results of our study are split by alloy system: the Nb-Mo alloy is discussed in Chapter 3, while the MgB_2-based alloys are presented in Chapter 4. The structural parameters, electronic properties, phonon frequencies and e-ph coupling spectra,

and superconducting properties such as T_c and gaps are analyzed and discussed as a function of the concentration for each alloy. The numerical details for each system are also included in the corresponding chapters. Finally, the conclusions of this thesis are presented.

Chapter 1

The Density Functional Theory and methods

1.1 Introduction

There are different numerical calculation methods right now that are used to determine the ground state of solid state systems and materials in general, treating the many-body problem from the theoretical point of view. These methods, or approximations, are classified in three main groups: the first one is the Hartree-Fock approximation, The second one is based in the density funcional theory (DFT), and the last one are the statistical quantum methods, like the Monte Carlo, for example. In this thesis we use the second type method, that is to say, the density functional theory in order to describe and analyze the systems under study.

A theoretical description of the electronic properties of a specific system is not easy at all, since we are dealing as we said before with a many-body problem. Then, we start the description of the system with the time-independent Schrödinger equation

$$\left[-\frac{h^2}{2m} \sum_i \nabla_i^2 + \sum_i V_{\text{ext}}(\mathbf{r}_i) + \frac{1}{2} \sum_{i,j}{}' \frac{e^2}{|\mathbf{r}_i - \mathbf{r}_j|} \right] \Psi(\mathbf{r}_1, \mathbf{r}_2, \ldots, \mathbf{r}_N) = E\Psi(\mathbf{r}_1, \mathbf{r}_2, \ldots, \mathbf{r}_N)$$

$$(1.1)$$

assuming the Born-Oppenheimer approximation, which is based on the nuclei being much heavier than electrons. In this case we can neglect the nuclei movement, considering them as static and then we only take into account the electrons movement. in the last equation $\mathbf{r}_i$ is the position vector of the i-th electron, N is the total number of electrons in the system, V_{ext} is the external potential where the electrons move (potential generated by the nuclei), and E is the total electronic energy. The Hamiltonian's first terms on Eq. (1.1) correspond to the kinetic energy and the external potential, respectively. Now, if we solve the last equation

just with the Hamiltonian terms mentioned before, we will get the energy that corresponds just to the interaction between the electrons and the nuclei, but it will be missing the term that corresponds to the interaction between electrons (Coulomb interaction). That term is the third one on Eq. (1.1). As we can see from that equation, although spin variables have not been taken into account explicitly in order to simplify the equation, it is still quite complicated to solve Eq. (1.1) for general cases. The reason is the dependence of the wavefunction on the $3N$ position coordinates, and also due to the electron-electron interaction term, so it is impossible to simplify the equation to an easier form in order to solve in a straight forward way. However, we have one advantage, since we know that many of the important properties, or experimental observables that we are interested in, depend only on the electronic charge density, which could be expressed as

$$\rho(\mathbf{r}) = N \int \Psi(\mathbf{r}, \mathbf{r}_2, \dots, \mathbf{r}_N)\Psi^*(\mathbf{r}, \mathbf{r}_2, \dots, \mathbf{r}_N)d\mathbf{r}_2 d\mathbf{r}_3 \dots d\mathbf{r}_N. \qquad (1.2)$$

When we calculate Ψ we are obtaining more information than actually needed for many practical applications, additionally the computing-time used is increased, so it is convenient to avoid the calculation of this extra information included in Ψ that is useless for our purposes. A first approach to obtain a system where we do not need to put our hands directly on the wavefunctions was the theory proposed by Thomas-Fermi [65–67]. That theory, which is an approximation by construction, was focused on calculating all the interesting properties using only as a starting point the electronic charge density $\rho(\mathbf{r})$. At that time there were efforts to develop approximate ways to calculate the electronic charge density $\rho(\mathbf{r})$ or the wavefunction Ψ [68,69]. Later, Hohenberg and Kohn [7] took up the basic idea of Thomas-Fermi model and formulated the density functional theory as an exact theory of the many-body system. This formulation applies to any system of interacting particles in an external potential, $V_{\text{ext}}(\mathbf{r})$. The DFT, as we know it nowadays, is based upon two theorems proved by Hohenberg and Kohn [7], which are:

Theorem I: *For any system of interacting particles in any external potential $V_{\text{ext}}(\mathbf{r})$, the potential $V_{\text{ext}}(\mathbf{r})$ is determined uniquely, apart from a constant, by the ground state charge density $\rho_0(\mathbf{r})$.*

Theorem II: *A universal functional $E[\rho]$ in terms of the charge density $\rho(\mathbf{r})$ can be defined, valid for any external potential $V_{\text{ext}}(\mathbf{r})$. For any particular $V_{\text{ext}}(\mathbf{r})$, the exact ground state energy of the system is the global minimum value of this functional, and the density $\rho(\mathbf{r})$ that minimizes the functional is the exact ground state charge density $\rho_0(\mathbf{r})$.*

The consequences of these two theorems are quite important, because, from Theorem I, we have that since the Hamiltonian is fully determined (by the knowledge of $\rho_0(\mathbf{r})$), it follows that the many-body wavefunctions for all states (ground and excited) are determined by $\rho_0(\mathbf{r})$. Therefore all the properties of the system are completely determined given only the ground state charge density $\rho_0(\mathbf{r})$. According to Theorem II, the functional $E = E[\rho(\mathbf{r})]$ alone is sufficient to determine the exact ground state energy and density, but it does not provide any direct guidance concerning excited states. The great importance of the Hohenberg-Kohn theorems lies in the fact that it is not necessary to explicitly calculate of the wave function Ψ for the N particle system, but only the total electronic charge density $\rho(\mathbf{r})$ is needed in order to obtain all the properties of the ground state. However, this theorem does not tell us the explicit form of the functionals, and until now there do not exist exact functionals for the total energy $E = E[\rho(\mathbf{r})]$.

1.2 Kohn-Sham equations

The Kohn-Sham approach is used to replace the difficult interacting many-body system obeying the Hamiltonian of the Eq. (1.1) with a different auxiliary system that can be solved more easily. Kohn and Sham reformulated the problem of calculating the ground state total energy of a charge density functional ($E[\rho(\mathbf{r})]$), in such a way that the problem of N interacting particles (electrons) is solved using a group of N independent Schrödinger equations for individual independent particles but with an interacting density and a complicated effective potential.

The *ansatz* of Kohn and Sham [8] assumes that the ground state density of the original interacting system is equal to that of some chosen non-interacting system. This leads to independent-particle equations for the non-interacting system that can be considered exactly soluble (in practice by numerical means) with all the difficult many-body terms incorporated into an *exchange-correlation (xc)* functional of the density. The exchange term comes from the hole in the probability density of electrons due to the Pauli principle, i.e., the antisymmetry of the wavefunction and applies only to electrons with the *same spin*. The correlation term has contributions for electrons of either spin and is the hole resulting from the Coulomb electrostatic interaction which avoids electrons get close together. It is important to mention that only the total contribution (exchange-correlation) has a real physical meaning. The energy under this scheme is expressed in the following way,

$$E[\rho] = T[\rho] + \int \rho(\mathbf{r}) \left[V_{\text{ext}}(\mathbf{r}) + \frac{1}{2} V_{\text{C}}(\mathbf{r}) \right] d\mathbf{r} + \xi_{\text{xc}}[\rho], \tag{1.3}$$

where $T[\rho]$ is the kinetic energy of the system, considered as a ground state property and then expressed as a density functional. The next term is the energy

related to the external potential due to the nuclei and any other external fields. The following one is the classical Coulomb interaction energy of the electron density $\rho(\mathbf{r})$,

$$\frac{e^2}{2} \int \int \frac{\rho(\mathbf{r}_1)\rho(\mathbf{r}_2)}{|\mathbf{r}_1 - \mathbf{r}_2|} d\mathbf{r}_1 d\mathbf{r}_2 = \frac{1}{2} \int V_C(\mathbf{r})\rho(\mathbf{r})d\mathbf{r}. \tag{1.4}$$

The last term $\xi_{xc}[\rho]$ on Eq. (1.3) is where are grouped all the many-body effects of exchange and correlation, and it is named exchange-correlation energy. The Eq. (1.3) could be solved by applying the variational principle that comes from the Theorem II of DFT:

$$E[\tilde{\rho}(\mathbf{r})] \geq E[\rho(\mathbf{r})], \tag{1.5}$$

including the constrain of having a fixed number of particles in the system (N), that is also a particular functional of $\rho(\mathbf{r})$,

$$N = \int \rho(\mathbf{r})d\mathbf{r}, \tag{1.6}$$

which is related by a Lagrange multiplier [8],

$$\frac{\delta}{\delta\rho}\left[E - \mu\left(\int \rho(\mathbf{r}) - N\right)\right] = 0. \tag{1.7}$$

This gives the next Euler-Lagrange equation [8]

$$\frac{\delta T}{\delta\rho} + V_{ext}(\mathbf{r}) + V_C(\mathbf{r}) + \frac{\delta\xi_{xc}}{\delta\rho} = \mu, \tag{1.8}$$

where the Lagrange multiplier μ corresponds to the chemical potential of the electron gas.

In the next step, Kohn and Sham compared the last result with the one obtained from a non-interacting N particles system (fermions) moving under the effects of an effective potential V_{eff}, constructed in such a way that the charge density of this new system is equivalent to the one of the real system. Then, according to this, we can write Eq. (1.8) in a different way,

$$\frac{\delta\tilde{T}}{\delta\rho} + V_{eff}(\mathbf{r}) = \mu. \tag{1.9}$$

In the equation above it has been introduced the kinetic energy of a non-interacting particle system $\tilde{T}$. the components of these non interacting system are called the particles of the auxiliary system to differentiate them from the real system particles. Thus, relating the two last equations we find an expression for V_{eff},

$$
\begin{aligned}
V_{\text{eff}}(\mathbf{r}) &= V_{\text{ext}}(\mathbf{r}) + V_{\text{C}}(\mathbf{r}) + \frac{\delta \xi_{\text{xc}}}{\delta \rho} + \left(\frac{\delta T}{\delta \rho} - \frac{\delta \tilde{T}}{\delta \rho} \right) \\
&\equiv V_{\text{ext}}(\mathbf{r}) + V_{\text{C}}(\mathbf{r}) + V_{\text{xc}}(\mathbf{r}),
\end{aligned}
\tag{1.10}
$$

where we have introduced the exchange-correlation potential $V_{\text{xc}}(\mathbf{r})$, which is given by

$$
V_{\text{xc}}(\mathbf{r}) = \frac{\delta \xi_{\text{xc}}}{\delta \rho} + \left(\frac{\delta T}{\delta \rho} - \frac{\delta \tilde{T}}{\delta \rho} \right).
\tag{1.11}
$$

The main advantage of introducing the auxiliary system is that for this system we can solve the many-body Schrödinger equation, just splitting it into N equations of independent particles with a potential that must be found self-consistently with the resulting density, and these equations represent the Kohn-Sham equations in their canonical form

$$
\left[-\frac{\hbar^2}{2m} \nabla^2 + V_{\text{eff}}(\mathbf{r}) \right] \psi_i(\mathbf{r}) = \varepsilon_i \psi_i(\mathbf{r}),
\tag{1.12}
$$

where $\psi_i(\mathbf{r})$ and ε_i correspond to the wavefunction (also called orbital) and the eigenvalue of the energy for the i-th particle of the auxiliary system, respectively. Additionally we have the expression for the charge density as a function of the orbitals,

$$
\rho(\mathbf{r}) = \sum_{i=1}^{N} |\psi_i(\mathbf{r})|^2.
\tag{1.13}
$$

As we mentioned before, the charge density expressed by Eq. (1.13) is equivalent to the one of the real system, by construction, but the orbitals ψ_i and eigenvalues ε_i do not correspond to the real particles.

In practice, the charge density of the ground state is found in a self-consistent way by applying iterative methods, which start with a test charge density, that usually corresponds to the superposition of isolated atoms. From this density we can construct the potential V_{eff}, plug it into Eq. (1.12) and by solving the equations to get the orbitals ψ_i. Once we get the eigenvalues and orbitals, using Eq. (1.13) we are able to find a new density, which is compared with the previous one. This process is repeated and until a certain convergence criteria between the input and output densities is reached. On this way we get a good approximation of the real system by the use of the auxiliary system.

The charge density of the auxiliary and real systems are equivalent but, the orbitals and eigenvalues are not. In this way, the total energy of the auxiliary system of independent particles is just the sum of the eigenvalues of the occupied

orbitals ε_i, but in the case of the real system the energy is given by a more complex expression,

$$E[\rho] = \sum_{i=1}^{N} \left\langle \psi_i \left| -\frac{\hbar^2}{2m}\nabla^2 \right| \psi_i \right\rangle + \int \rho(\mathbf{r}) \left[V_{\text{ext}}(\mathbf{r}) + \frac{1}{2}V_{\text{C}}(\mathbf{r}) \right] d\mathbf{r} + E_{\text{xc}}[\rho]. \quad (1.14)$$

However, using Eqs. (1.10) and (1.12) we can simplify the total energy expression of Eq. (1.14) in the following way

$$E[\rho] = \sum_{i=1}^{N} \varepsilon_i - \int \rho(\mathbf{r}) \left[V_{\text{ext}}(\mathbf{r}) + \frac{1}{2}V_{\text{C}}(\mathbf{r}) \right] d\mathbf{r} + E_{\text{xc}}[\rho], \quad (1.15)$$

where we have defined $E_{\text{xc}} = \xi_{\text{xc}} + (T - \tilde{T})$. The last equation tells us that the sum of individual particle energies is modified by the exchange-correlation energy term. Thus, the Kohn-Sham equations are independent of any approximation to the functional $E_{\text{xc}}[\rho]$, and would lead to the exact ground state density and energy for the interacting (or real) system, if the exact functional $E_{\text{xc}}[\rho]$ was known. Furthermore, it follows from the Hohenberg-Kohn theorems that the ground state density uniquely determines the potential at the minimum, so there is an unique Kohn-Sham potential $[V(\mathbf{r})]_{\text{min}} \equiv V_{\text{eff}}(\mathbf{r})$ associated with any given interacting electron system. The problem is that until now there is not available an exact functional for $E_{\text{xc}}[\rho]$, and the theory does not give a functional form for this energy, in contrast to the other terms on Eq. (1.15), therefore, $E_{\text{xc}}[\rho]$ has to be approximated. The simplest way is to use a local or nearly local functional of the density. This means that the exchange-correlation energy can be expressed in the form

$$E_{\text{xc}}[\rho(\mathbf{r})] = \int \rho(\mathbf{r}) \epsilon_{\text{xc}}[\rho(\mathbf{r})] d\mathbf{r}, \quad (1.16)$$

where $\epsilon_{\text{xc}}[\rho(\mathbf{r})]$ is an energy per electron at point $\mathbf{r}$ that depends only on the local density $\rho(\mathbf{r})$. In the next section some of the different approximations proposed to find an appropriate expression for the exchange-correlation energy are discussed.

1.3 xc-functionals: LDA and GGA

In the previous section we introduced the Kohn-Sham formalism which allows an exact treatment of most of the contributions to the electronic energy of an atomic or molecular system, including the major fraction of the kinetic energy. All remaining, unknown parts are collected into the exchange-correlation functional $E_{\text{xc}}[\rho(\mathbf{r})]$. As we mentioned before, this includes the non-classical portion of the electron-electron interaction along with the correction for the self-interaction and the component of the kinetic energy not covered by the non-interacting reference

system. In this section we introduce two of the approximations widely used for the description of $E_{xc}[\rho(\mathbf{r})]$, namely the local density approximation and beyond it, the generalized gradient approximation. The simplest, and at the same time remarkably useful, approximation for the exchange-correlation potential is the so-called local density approximation, LDA. The central point of this model is the idea of a hypothetical *uniform electron gas*. This is a system in which electrons move in a positive background charge distribution such that the total ensemble is electrically neutral. The number of electrons as well as the volume V of the gas are considered to approach infinity, while the electron density ($N/V = \rho$) remains finite and has a constant value everywhere. The model system over which LDA rests, also known as the homogeneous electron gas, is widely used nowadays, despite being a very simple and crude approximation, because it is the only system for which we know the form of the exchange and correlation energy functionals exactly or at least to a very high accuracy. The LDA uses the expression of $E_{xc}[\rho(\mathbf{r})]$ as exposed on the seminal work of Kohn-Sham, Eq. (1.16) [8]. The quantity $\epsilon_{xc}[\rho(\mathbf{r})]$ can be further split into exchange and correlations contributions,

$$\epsilon_{xc}[\rho(\mathbf{r})] = \epsilon_x[\rho(\mathbf{r})] + \epsilon_c[\rho(\mathbf{r})]. \tag{1.17}$$

The expressions for these two quantities vary depending on the version or specific approximation of LDA. In this thesis we apply two different versions for the LDA *xc*-functional, the Hedin-Lundqvist (HL) [70] as well as the Perdew and Wang version (PW92) [71]. These two parametrizations have the following expression for ϵ_x, in the non-polarized case (per spin ρ and per electron $\rho \to 2\rho$),

$$\epsilon_x = -\frac{3}{4}\left(\frac{2}{\pi}\rho\right)^{1/3} = -\frac{3}{4\pi r_s}\left(\frac{9\pi}{4}\right)^{1/3}, \tag{1.18}$$

where the parameter r_s is defined as the radius of a sphere containing one electron on average, $r_s = (3/4\pi\rho)^{1/3}$. Thus, r_s is a measure of the average distance between electrons. For partially polarized systems, the exchange energy is just the sum of terms for the two spins, which can also be expressed in terms of the total density $\rho = \rho^\uparrow + \rho^\downarrow$ and the fractional polarization

$$\zeta = \frac{\rho^\uparrow - \rho^\downarrow}{\rho}. \tag{1.19}$$

Then we can re-write $\epsilon_x(r_s, \zeta)$ using Eqs. (1.18) and (1.19) as

$$\epsilon_x(r_s, \zeta) = -\frac{3}{4\pi r_s}\left(\frac{9\pi}{4}\right)^{1/3}\left[(1+\zeta)^{4/3} + (1-\zeta)^{4/3}\right]/2. \tag{1.20}$$

For the ϵ_c term, each parametrization (HL and PW92) has its own form. They are very similar however small differences exist. For HL we have,

$$\epsilon_c(r_s) = -C\left[(1+x^3)\ln\left(1+\frac{1}{x}\right) + \frac{x}{2} - x^2 - \frac{1}{3}\right],\tag{1.21}$$

and the correlation potential is obtained from,

$$V_c(r_s) = \epsilon_c(r_s) - \frac{r_s}{3}\frac{d\epsilon_c(r_s)}{dr_s}\tag{1.22}$$

giving the following expression,

$$V_c(r_s) = -C\ln\left(1+\frac{1}{x}\right),\tag{1.23}$$

where $C = 0.045$ Ryd, $x = r_s/A$, and $A = 21$.

On the other hand, the expression for the PW92 version is,

$$\epsilon_c(r_s, \zeta) = \epsilon_c(r_s, 0) + \alpha_c(r_s)\frac{f(\zeta)}{f''(0)} + \left[\epsilon_c(r_s, 1) - \epsilon_c(r_s, 0)\right]f(\zeta)\zeta^4,\tag{1.24}$$

where,

$$f(\zeta) = \frac{(1+\zeta)^{4/3} + (1-\zeta)^{4/3} - 2}{(2^{4/3} - 2)}.\tag{1.25}$$

The functions $\epsilon_c(r_s, 0)$, $\epsilon_c(r_s, 1)$ and $-\alpha_c(r_s)$ are obtained from the following general equation, just performing the substitution of G by each one of the previous functions,

$$G(r_s, A, \alpha_1, \beta_1, \beta_2, \beta_3, \beta_4, p) =$$
$$-2A(1+\alpha_1 r_s)\ln\left[1 + \frac{1}{2A(\beta_1 r_s^{1/2} + \beta_2 r_s + \beta_3 r_s^{3/2} + \beta_4 r_s^{P+1})}\right],\tag{1.26}$$

where the parameters A, α_1, β_i, and P are fitted in such a way to get the correlation energy in the high density limit.

The poor performance of LDA in certain systems has led to the development of various generalized gradient approximations (GGAs) with marked improvement over LDA for many cases [72–77]. The first step beyond the local approximation is a functional that depends on the magnitude of the density gradient $|\nabla\rho|$ as well as the value of ρ at each point. Such a "gradient expansion approximation" (GEA) was suggested in the original paper of Kohn and Sham [8], and obtained by Herman *et al.* [78]. The low-order expansion of the exchange and correlation energies is known [79]. However, the GEA does not lead to consistent improvement over the LDA. It violates the sum rules and other relevant conditions, like that the exchange hole is not restricted to be negative for any pair $(\mathbf{r}_1; \mathbf{r}_2)$ [78] and,

indeed, often leads to worse results. The basic problem is that gradients in real materials are so large that the expansion breaks down.

The term _generalized_-gradient approximation (GGA) denotes a variety of proposed ways for functions that modify the behavior at large gradients in such a way to preserve desired properties. Then, it is convenient to define the functional as a generalized form of the Eq. (1.6) [80],

$$
\begin{aligned}
E_{\mathrm{xc}}^{GGA}[\rho(\mathbf{r})] &= \int \rho(\mathbf{r})\epsilon_{\mathrm{xc}}[\rho(\mathbf{r}), |\nabla\rho(\mathbf{r})|]d\mathbf{r}, \\
&\equiv \int \rho(\mathbf{r})\epsilon_{\mathrm{x}}^{hom}[\rho(\mathbf{r})]F_{\mathrm{xc}}[\rho(\mathbf{r}), |\nabla\rho(\mathbf{r})|]d\mathbf{r}, \qquad (1.27)
\end{aligned}
$$

where F_{xc} is dimensionless and $\epsilon_{\mathrm{x}}^{hom}$ is the exchange energy of the non-polarized (or unpolarized) gas given by Eq. (1.18). For the exchange energy we only need to consider the spin-unpolarized $F_{\mathrm{x}}[\rho(\mathbf{r}), |\nabla\rho(\mathbf{r})|]$.

In this thesis we use the GGA parametrization of Perdew, Burke and Ernzerhof proposed in 1996, known as GGA-PBE96 [81]. In PBE96, the exchange is given by a simple form for the enhancement factor F_{x}. The form is chosen with $F_{\mathrm{x}}(0) = 1$ (so that the local approximation is recovered) and $F_{\mathrm{x}} \to constant$ at large s,

$$
F_{\mathrm{x}}(s) = 1 + \kappa - \frac{\kappa}{1 + \mu s^2/\kappa}, \qquad (1.28)
$$

where s is the dimensionless reduced density gradient, and is given by,

$$
s = \frac{|\nabla\rho|}{2k_F\rho} \qquad (1.29)
$$

having $k_F = 3(2\pi/3)^{1/3}r_s^{-1}$ as the Fermi's wavevector. The numerical values for the parameters are $\kappa = 0.804$ and $\mu = 0.21951$. These values are chosen in order to satisfy boundary conditions and to recover the linear response form of the local approximation.

The form for the correlation is expressed as the local correlation plus an additive term, both depending upon the gradients and spin polarization. The form chosen to satisfy several conditions is [80]

$$
E_{\mathrm{c}}^{GGA-PBE96}[\rho^\uparrow, \rho^\downarrow] = \int \rho[\epsilon_c^{hom}(r_s, \zeta) + H(r_s, \zeta, t)], \qquad (1.30)
$$

where $\zeta = (\rho^\uparrow - \rho^\downarrow)/\rho$ is the spin polarization, r_s is the local value of the density parameter and t is a dimensionless gradient $t = |\nabla\rho|/2\phi k_{TF}\rho$. Here $\phi = [(1 + \zeta)^{2/3} + (1 - \zeta)^{2/3}]/2$ and t is scaled by the screening wavevector k_{TF} rather than k_F ($k_{TF} = \sqrt{4k_F/\pi a_0}$, with a_0 the Bohr radius). The final form is

$$
H = \frac{e^2}{a_0}\gamma\phi^3\ln\left(1 + \frac{\beta}{\gamma}t^2\frac{1 + At^2}{1 + At^2 + A^2t^4}\right), \qquad (1.31)
$$

where the factor e^2/a_0 is unity in atomic units. The function A is given by

$$A = \frac{\beta}{\gamma} \left[\exp\left(\frac{-\epsilon_c^{hom}}{\gamma\phi^3 e^2/a_0} \right) - 1 \right]^{-1}, \qquad (1.32)$$

where the PBE96 parametrization uses $\beta = 0.066725$ and $\gamma = 0.031091$.

1.4   The full-potential method

In order to solve the Kohn-Sham equations the use of approximations is needed from the practical point of view where they are used trying to reduce the computing time, for example. The majority of the methods that we have until now for solving the equations of DFT consider the expansion of the eigenfunctions ψ_i in some kind of basis functions and also some kind of treatment of the potential in order to make the problem more tractable. One of the methods used in this thesis belongs to the group of so called *full potential methods* (since they include explicitly the core electrons in the calculation), applying a linearized augmented planewave (LAPW) scheme as an expansion basis. The LAPW method is basically a modification to the augmented planewave method (APW) of Slater [82,83]. The essence of the APW method is the following [82]: near an atomic nucleus the potential and wavefunctions of the system are similar to those in an isolated atom, i.e., they are strongly varying but nearly spherical. Conversely, in the regions between atoms both the potential and wavefunctions behave in a smoother way. According to this, the space is then divided into two regions and different basis expansions are used in these regions: radial solutions of the Schrödinger equation inside the non-overlapping atom centered spheres (region II) and planewaves in the remaining interstitial region (region I). In Fig. 1.1 we show a schematic representation of these two regions.

The fundamental improvement of the LAPW method over the APW was the proposing that the basis functions and their derivatives be continuous at the boundary of the regions, by matching them to a radial function at fixed E_l and its derivative with respect to E_l [54]. This choice solved some problems with the APW method [56] that prevented it to be used as a full potential method.

In the LAPW method, the basis functions inside the spheres are linear combinations of radial functions $u_l(r)Y_{lm}(\mathbf{r})$ and their energy derivatives. The energy derivative, $\dot{u}_l(r)Y_{lm}(\mathbf{r})$, satisfies

$$\left\{ -\frac{d^2}{dr^2} + \frac{l(l+1)}{r^2} + V(r) - E_l \right\} r\dot{u}_l(r) = ru_l(r) \qquad (1.33)$$

in the non-relativistic case. These functions are matched to the values and derivatives of the planewaves on the sphere boundaries. Planewaves, augmented in this way, are the LAPW basis functions. In terms of this basis the wavefunctions are
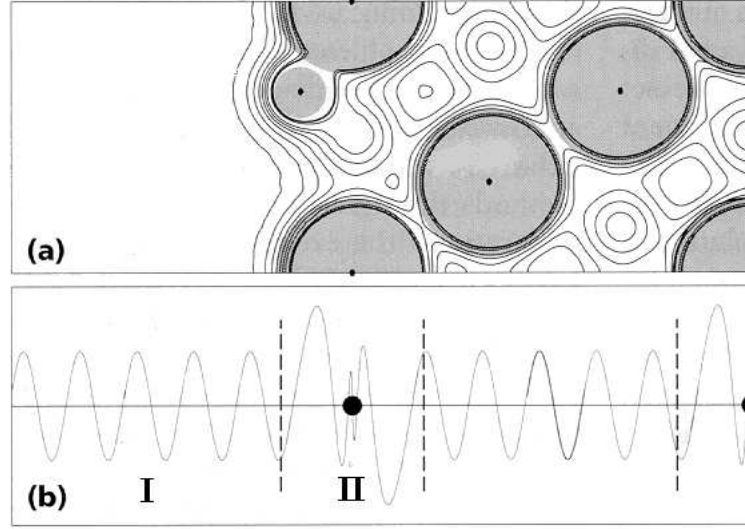
Figure 1.1: In the APW and LAPW methods, the space is divided in two regions. In (a) we have a scheme where is showed the division of the space in two regions on a charge density map and in (b) the division is showed in terms of the different functions: I-planewaves and II-spherical harmonics.

$$\phi_{k_n} = \begin{cases} \frac{1}{\Omega^{1/2}} e^{i\mathbf{k}_n \cdot \mathbf{r}} & \mathbf{r} \in I \\ \\ \sum_{lm} \left[A_{lm} u_l(r, E_l) + B_{lm} \dot{u}_l(r, E_l) \right] Y_{lm}(\mathbf{r}) & \mathbf{r} \in II \end{cases} \tag{1.34}$$

where $u_l(r, E_l)$ is the radial solution of the Kohn-Sham equation for a fixed energy E_l and $\dot{u}_l(r, E_l)$ is the energy derivative of the same function evaluated at the same energy. The coefficients A_{lm} and B_{lm} are functions of $\mathbf{k}_n$, which are determined in order to obtain the continuity on the boundary. For the interstitial zone, the expansion is based on planewaves with $\mathbf{k}_n = \mathbf{k} + \mathbf{K}_n$, where $\mathbf{K}_n$ are the reciprocal lattice vectors and $\mathbf{k}$ is the wavevector inside the first Brillouin zone. An important point to mention is that inside the spheres the LAPWs have more variational freedom than APWs. For example, if E_l differs slightly from the band energy (ϵ) a linear combination then, will reproduce the APW radial function constructed at that band energy

$$u_l(r, \epsilon) = u_l(r, E_l) + (E_l - \epsilon) \dot{u}_l(r, E_l) + O(E_l - \epsilon)^2, \tag{1.35}$$

where $O(E_l - \epsilon)^2$ denotes errors that are quadratic on this energy difference.

The solutions to the Kohn-Sham equations are expanded in this combined basis set of LAPWs according to the linear variation method,

$$\psi_k = \sum_n c_n \phi_{k_n} \tag{1.36}$$

and the coefficients c_n are determined by the Rayleigh-Ritz variational principle. In order to improve upon the linearization (i.e. to increase the flexibility of the basis) and to make possible a consistent treatment of semicore and valence states in one energy window (to ensure orthogonality) additional k_n independent basis functions can be added. They are called "local orbitals (LO)" [84] and consist of a linear combination of two radial functions at two different energies and one energy derivative (at one of these energies):

$$\phi_{lm}^{LO} = [A_{lm}u_l(r, E_{1,l}) + B_{lm}\dot{u}_l(r, E_{1,l}) + C_{lm}u_l(r, E_{2,l})] Y_{lm}(\mathbf{r}) \qquad (1.37)$$

The coefficients A_{lm}, B_{lm}, and C_{lm} are determined by constrains on ϕ^{LO}. It should be normalized and goes to zero in value and slope at the sphere boundary.

In this general form the LAPW method expands the potential as following

$$V(\mathbf{r}) = \begin{cases} \sum_K V_K(r)e^{i\mathbf{K}\cdot\mathbf{r}} & \mathbf{r} \in I \\ \\ \sum_{lm} V_{lm}(r)Y_{lm}(\mathbf{r}) & \mathbf{r} \in II \end{cases} \qquad (1.38)$$

and the charge density in an analogous way. Thus no shape approximations are made, a procedure frequently called as a "full-potential" method. The code that is used on this thesis for the full-potential calculations is the WIEN2K code, developed by Blaha and coworkers [57].

1.5   The pseudopotential method

The other method used in this thesis is a pseudopotential one, applying a mixed-basis for the eigenfunctions [59,85,86]. The fundamental idea of a *pseudopotential* is the replacement of one problem with a simpler one. The primary application in electronic structure is the replacement of the strong Coulomb potential of the nucleus and the effects of the tightly bound core electrons by an effective ionic potential acting on the valence electrons. This is the essence of the pseudopotential approximation: the strong core potential (including the ionic potential, core charge and a component of the exchange-correlation potential related to the valence-core interaction) is replaced by a pseudopotential, whose ground state wavefunction φ^{ps} mimics the all electron valence wavefunction outside a selected core radius r_c [56,87–90] (see Fig. 1.2).

For the calculations in this thesis we have used the so called *ab-initio norm-conserving pseudopotentials* [91, 92] in order to ensure the accuracy and trans-ferability of them. The term *ab-initio* is used because they are not fitted to experiment, in fact they are constructed to fit the valence properties calculated for the atom (or atomic-like states). The creation of this kind of pseudopoten-tials was motivated by the following goals: (1) the pseudopotential should be
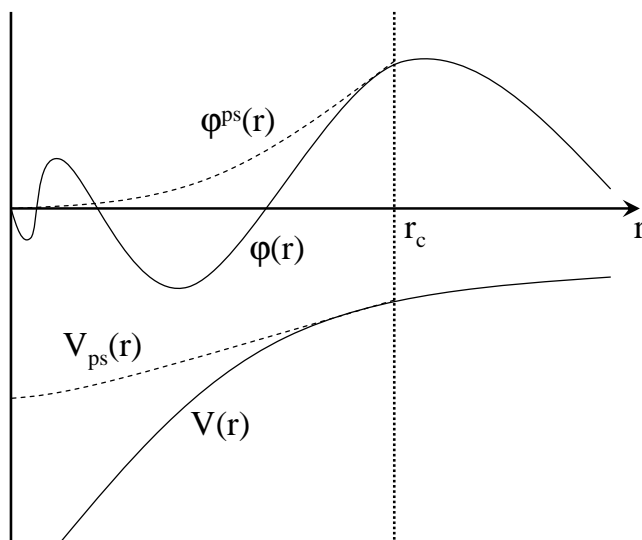
Figure 1.2: Schematic illustration of the replacement for the all-electron wavefunction and core potential by a pseudo-wavefunction and pseudopotential

as soft as possible meaning that it should allow expansion of the valence pseudo-wavefunctions using as few planewaves as possible; (2) it should be as transferable as possible, meaning that the pseudopotential generated for a given atomic configuration should reproduce also others accurately, helping to assure that the results will be reliable in solid state calculations where the crystal potential is necessarily different from an atomic potential; and (3) the pseudo-charge density (the density constructed using the pseudo-wavefunctions) should reproduce the valence charge density as accurately as possible. With norm-conserving pseudopotentials, the pseudo-wavefunctions and pseudopotential are constructed to be equal to the actual valence wavefunctions and potential outside some core radius, r_c. Inside $\mathbf{r}_c$, the pseudo-wavefunctions differ from the true wavefunctions, but the norm is constrained to be the same. That is,

$$\int_0^{r_c} \mathrm{d}r r^2 \varphi^{ps*}(r)\varphi^{ps}(r) = \int_0^{r_c} \mathrm{d}r r^2 \varphi^*(r)\varphi(r) \tag{1.39}$$

where the wavefunctions refer to the atomic reference state and spherical symmetry is enforced. It is important to note that the wavefunctions and eigenvalues are different for different angular momenta (l) and this implies that the pseudopotential should also be l dependent.

One measure of transferability is provided by the logarithmic derivatives at r_c of the all-electron and pseudo-wavefunctions, φ and φ^{ps}, respectively. The imposed equality of these for $r \geq r_c$, ensures that the logarithmic derivatives at r_c are also equal for the atomic reference configuration.

$$\frac{1}{\varphi^{ps}(\mathrm{r}_c, E)} \frac{\mathrm{d}\varphi^{ps}(\mathrm{r}_c, E)}{\mathrm{d}r} = \frac{1}{\varphi(\mathrm{r}_c, E)} \frac{\mathrm{d}\varphi(\mathrm{r}_c, E)}{\mathrm{d}r} \tag{1.40}$$

where E is the energy. The transferability is then defined by the range of E over which Eq. (1.40) holds adequately. However, using Green's theorem, we have

$$-\frac{\partial}{\partial E} \frac{\partial}{\partial r} \ln\varphi(r_c, E) = \frac{1}{r_c^2 \varphi^*(r_c, E)\varphi(r_c, E)} \int_0^{r_c} \mathrm{d}r r^2 \varphi^*(r_c, E)\varphi(r_c, E). \tag{1.41}$$

Imposition of norm-conservation ensures not only that the logarithmic derivative of the pseudo- and all-electron wavefunction match at the reference energy, but also that the first derivative with respect to E matches as well. Thus, the difference between the pseudo- and all-electron logarithmic derivative is second order in the deviation from the reference, and this helps ensure transferability for norm-conserving pseudopotentials. The method used here for construction of the pseudopotentials and pseudo-wavefunctions is the Vanderbilt scheme [93].

For many semiconductors or simple metals with only s and p valence states, the pseudopotentials are sufficiently smooth so that a small basis set of simple plane waves can be used. Nevertheless, in the case of transition metals, for example, the somewhat deeper pseudopotentials render planewave expansions uneconomical. A mixed basis consisting of planewaves and additional, well localized, energy-independent functions, which describe the more tightly bound nature of the d states, has proved to be very efficient [59,94]. The approximations made on the basis, the neglect of the core charge density and the shape difference between real and pseudo-valence charge densities within a small sphere around the atomic positions, hold as long as the real core and valence charge densities do not significantly overlap outside this sphere. For the calculations applying the pseudopotential formalism, we have used an energy-independent mixed-basis set [59,85,86]. It contains a moderate number of plane waves augmented by well localized functions centered at the atomic sites to describe the localized states, such as d states.

In the mixed-basis method the wavefunctions for a crystal with several atoms per unit cell are given by

$$\psi_{n\mathbf{k}}(\mathbf{r}) = \sum_{\mathbf{G}} \alpha_G^{n\mathbf{k}} \frac{1}{\sqrt{\Omega}} e^{i(\mathbf{k}+\mathbf{G})\cdot\mathbf{r}} + \sum_{j,l,m} \beta_{jlm}^{n\mathbf{k}} \phi_{jlm}^{\mathbf{k}}(\mathbf{r}). \tag{1.42}$$

where $\alpha_{\mathbf{G}}^{n\mathbf{k}}$ and $\beta_{jlm}^{n\mathbf{k}}$ are obtained as eigenvectors $\psi^{n\mathbf{k}}$ of the generalized eigenvalue problem:

$$\mathbf{H}^{\mathbf{k}}\psi^{n\mathbf{k}} = \epsilon_{n\mathbf{k}}\mathbf{S}^{\mathbf{k}}\psi^{n\mathbf{k}}, \tag{1.43}$$

where $\mathbf{H}^{\mathbf{k}}$ and $\mathbf{S}^{\mathbf{k}}$ are the Hamiltonian and overlap matrix, respectively. In Eq. (1.42) the terms

$$(1/\sqrt{\Omega})e^{i(\mathbf{k}+\mathbf{G})\cdot\mathbf{r}} \tag{1.44}$$

are the planewaves and $\phi^{\mathbf{k}}_{jlm}(\mathbf{r})$ are Bloch sums

$$\phi^{\mathbf{k}}_{jlm}(\mathbf{r}) = \frac{1}{\sqrt{N}}\sum_{\mathbf{R}}e^{i\mathbf{k}\cdot(\mathbf{R}+\mathbf{r}_j)}\varphi_{lm}(\mathbf{r}-\mathbf{R}-\mathbf{r}_j) \tag{1.45}$$

of localized basis functions φ_{lm} centered at the positions of atomic nuclei in the crystal ($\mathbf{r}' = \mathbf{r} - \mathbf{R} - \mathbf{r}_j$):

$$\varphi_{lm}(\mathbf{r}') = i^l f_l(r')K_{lm}(\hat{\mathbf{r}}') \quad r' = |\mathbf{r}'| \quad \hat{\mathbf{r}}' = \mathbf{r}'/|\mathbf{r}'| \tag{1.46}$$

The $f_l(r')$ are Gaussians or numerical functions, depending on the kind of orbital you want to describe (s, p, d, etc.). The localized numerical functions are derived from atomic valence pseudo-wavefunctions $\psi_l(r)$ by cutting off the tails beyond certain radius r_c. The cubic harmonics $K_{lm}(\hat{\mathbf{r}}')$ are given by

$$\left.\begin{array}{l} K_{l,+m}(\vartheta,\varphi) \\ K_{l,-m}(\vartheta,\varphi) \end{array}\right\} = \sqrt{\frac{2l+1}{2\pi(1+\delta_{0,m})}\frac{(l-m)!}{(l+m)!}}(-1)^m P_l^m(\cos\vartheta)\left\{\begin{array}{l} \cos m\varphi \\ \sin m\varphi \end{array}\right. \tag{1.47}$$

Finally for the calculation of the overlap matrix $\mathbf{S}^k$ and Hamiltonian matrix $\mathbf{H}^k$ entering in Eq. (1.43), matrix elements containing both planewaves and Bloch sums of the localized functions (Eqs. (1.48) and (1.49) respectively) have to be evaluated. The program used for the pseudopotential calculations in this study was the FORTRAN90 Program for Mixed-Basis Pseudopotential Calculations for Crystals, MBPP, developed by Meyer, Elsässer and Fähnle in Max-Planck-Institut für Metallforschung, Stuttgart, Germany [58].

1.6   The virtual crystal approximation

In this section we are presenting the approximation used to model the alloys. We are considering that a disordered alloy $A_{1-x}B_x$ is formed that results from a substitution of one former element (A) by the alloying one (B) at a certain content or concentration, x. The standard methods for studying alloys (supercells for example) require the construction of huge unit cells in order to ensure periodicity in the system, that is translated as an increasing in the computing time, and also in the lost of symmetry that makes difficult the interpretation of the results. Then for the simulation of the alloying in the cases under study in this thesis (Nb-Mo, $Mg_{1-x}Al_xB_2$, and $MgB_{2(1-x)}C_{2x}$ alloys), we use the virtual crystal approximation (VCA) [25–29]. This approximation simulates the alloying by the use of virtual atoms with fractional number of charge carriers that corresponds to the concentration of the alloy on the unit cell. To clarify the concept we use as an example,

the hypothetical $A_{1-x}B_x$ case. We perform a systematic substitution of all the A and B atoms (with n_A and n_B charge carriers, respectively) in the unit cell by a virtual atom with a fractional number of charge carriers that corresponds to the concentration of the alloy in the unit cell, $n_{A-B} = (1-x)n_A + (x)n_B$ (Fig. 1.3).
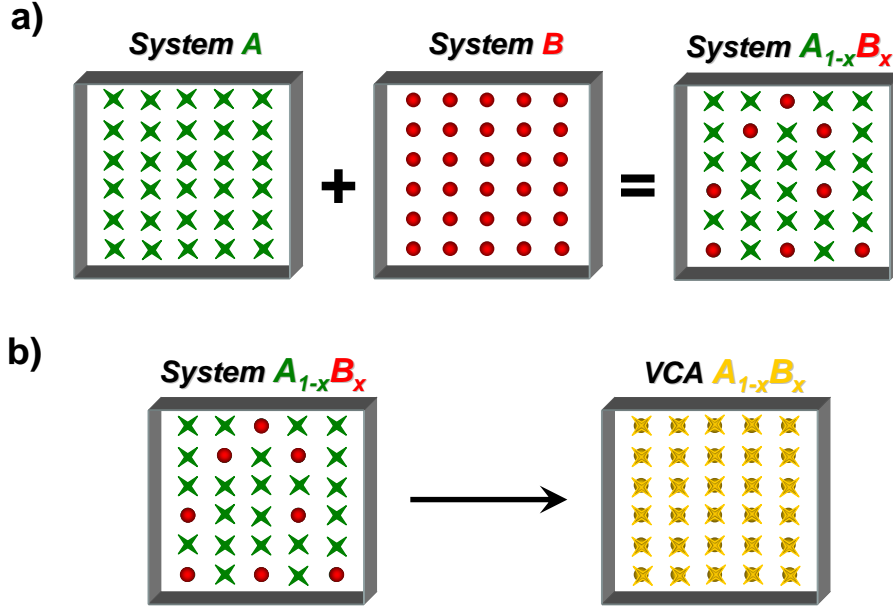
Figure 1.3: Schematic illustration of the replacement of the real alloy system a) by the VCA system b): the substitution of the atoms A and B by a virtual atom with fractional number of charge carriers $n_{A-B} = (1-x)n_A + (x)n_B$.

One important point to mention is that this approximation is only valid when the alloying elements are nearest neighbors on the periodic table, that is to say, $|n_A - n_B| = 1$. More important, once we have fixed the total number of charge carriers by atom on the unit cell (n_{A-B}), we let the system to evolve by means of a redistribution of the ground state charge density on a self-consistent way. This means that the only step where we are modifying the system is in n_{A-B}. In other words, we do not just perform an average of the charge density or the potential between atoms A and B, but rather these properties are generated and redistributed on every self-consistent cycle of the calculation, giving then a self-consistent virtual crystal approximation (SC-VCA) [27].

Chapter 2

Calculation methods for lattice dynamics and electron-phonon coupling

2.1 Introduction

A wide variety of physical properties of solids depend on their lattice-dynamical behavior: infrared, Raman, and neutron diffraction spectra; specific heat, thermal expansion, and heat conduction. Other phenomena are related to the electron-phonon interaction such as the resistivity of metals, and superconductivity to mention a few of them. The understanding of these properties in terms of phonons is considered an important part of the solid state theory and in general of the quantum theory. The basic theory of lattice vibrations dates back to the 1930s, and the work of Born and Huang [95] is considered today as a basic reference textbook of this field. These early formulations were mainly concerned with establishing the general properties of the dynamical matrices without considering their connections with the electronic properties that actually determine them. A systematic study of these connections was not performed until the 1970s [96, 97].

In the specific case of lattice-dynamical properties, a large number of *ab initio* calculations based on the linear response theory of lattice vibrations [96, 97] have been made possible over the past fifthteen years by the developments of density functional theory (DFT) [7, 8] and by the development of density functional perturbation theory (DFPT) [9, 98, 99]. The aim of this chapter is to review in some detail the theoretical framework of density functional perturbation theory, including the technical approaches used for the calculation of vibrational properties, namely, frozen phonon approximation and linear response theory. Additionally, we revise the electron-phonon coupling concepts and the Eliashberg formalism, which are used in the calculations of the superconducting properties of the systems under study in this thesis.

2.2   Perturbative DFT and the dynamic matrix

With the use of the *adiabatic approximation* of Born-Oppenheimer [100] (which is based on the nuclei being much heavier than electrons) we can separate the vibrational from the electronic degrees of freedom. Thus, the lattice-dynamical properties of a system are determined by the eigenvalues ϵ_N and eigenfunctions Φ_N of the Schrödinger equation:

$$\left(-\sum_I \frac{\hbar^2}{2M_I}\frac{\partial^2}{\partial \mathbf{R}_I^2} + E(\mathbf{R})\right)\Phi_N(\mathbf{R}) = \epsilon_N\Phi_N(\mathbf{R}),\qquad(2.1)$$

where M_I is mass of the Ith-nucleus, $\mathbf{R}_I$ its coordinate, $\mathbf{R} \equiv \{\mathbf{R}_I\}$ the set of all the nuclear coordinates, and $E(\mathbf{R})$ the clamped-ion energy of the system, which is often referred to as the *Born-Oppenheimer energy surface*. $E(\mathbf{R})$ is considered as the ground-state energy of a system of interacting electrons moving in the field of the nuclei (treated as fixed), whose Hamiltonian (that depends on $\mathbf{R}$) acting on the electronic variables reads

$$H_{BO}(\mathbf{R}) = -\frac{\hbar^2}{2m}\sum_i \frac{\partial^2}{\partial \mathbf{r}_i^2} + \frac{e^2}{2}\sum_{i\neq j}\frac{1}{|\mathbf{r}_i - \mathbf{r}_j|} - \sum_{iI}\frac{Z_I e^2}{|\mathbf{r}_i - \mathbf{R}_I|} + E_N(\mathbf{R}),\qquad(2.2)$$

where Z_I is the charge of the Ith nucleus, $-e$ is the electron charge, and $E_N(\mathbf{R})$ is the electrostatic interaction between nuclei given by

$$E_N(\mathbf{R}) = \frac{e^2}{2}\sum_{I\neq J}\frac{Z_I Z_J}{|\mathbf{R}_I - \mathbf{R}_J|}.\qquad(2.3)$$

The equilibrium of system is reached when the forces acting on the individual nuclei vanish:

$$\mathbf{F}_I \equiv -\frac{\partial E(\mathbf{R})}{\partial \mathbf{R}_I} = 0,\qquad(2.4)$$

whereas the vibrational frequencies of the atoms ω are obtained from the Hessian of the Born-Oppenheimer energy, scaled by the nuclear mass:

$$\det\left|\frac{1}{\sqrt{M_I M_J}}\frac{\partial^2 E(\mathbf{R})}{\partial \mathbf{R}_I \partial \mathbf{R}_J} - \omega^2\right| = 0.\qquad(2.5)$$

From the last two equations it can be seen that for obtain the equilibrium geometry and the vibrational properties of a system it is required the calculation of the first and second derivatives of its Born-Oppenheimer energy surface. In order to obtain this quantities it is used the Hellmann-Feynman theorem [101,102] which basically states that the first derivative of the eigenvalues of a Hamiltonian,

H_λ, that depends on a parameter λ, is given by the expectation value of the Hamiltonian's derivative:

$$\frac{\partial E_\lambda}{\partial \lambda} = \left\langle \Psi_\lambda \left| \frac{\partial H_\lambda}{\partial \lambda} \right| \Psi_\lambda \right\rangle, \tag{2.6}$$

where Ψ_λ is the eigenfunction of H_λ that corresponds to the E_λ eigenvalue. In the Born-Oppenheimer approximation, the nuclear coordinates act as parameters in the electronic Hamiltonian, see Eq. (2.2). Thus, the force acting on the I-th nucleus in the electronic ground state is

$$\mathbf{F}_I = -\frac{\partial E(\mathbf{R})}{\partial \mathbf{R}_I} = -\left\langle \Psi(\mathbf{R}) \left| \frac{\partial H_{BO}(\mathbf{R})}{\partial \mathbf{R}_I} \right| \Psi(\mathbf{R}) \right\rangle, \tag{2.7}$$

where $\Psi(\mathbf{r}, R)$ represents the electronic ground state wave function of the Born-Oppenheimer Hamiltonian. We observe that this Hamiltonian depends on $\mathbf{R}$ via the electron-ion interaction that couples to the electronic degrees of freedom only through the electron charge density. In this case, applying the Hellmann-Feynman theorem as expressed above, we have the following expression,

$$\mathbf{F}_I = -\int \rho_\mathbf{R}(\mathbf{r}) \frac{\partial V_\mathbf{R}(\mathbf{r})}{\partial \mathbf{R}_I} d\mathbf{r} - \frac{\partial E_N(\mathbf{R})}{\partial \mathbf{R}_I}, \tag{2.8}$$

where $V_\mathbf{R}(\mathbf{r})$ is the electron-nucleus interaction,

$$V_\mathbf{R}(\mathbf{r}) = -\sum_{iI} \frac{Z_I e^2}{|\mathbf{r}_i - \mathbf{R}_I|}, \tag{2.9}$$

and $\rho_\mathbf{R}(\mathbf{r})$ is the ground-state electron charge density corresponding to the nuclear configuration $\mathbf{R}$. With the help of the already obtained Hellmann-Feynman forces we are able to calculate the Hessian of the Born-Oppenheimer energy surface appearing in Eq. (2.5), by differentiating them with respect to the nuclear coordinates,

$$\frac{\partial^2 E(\mathbf{R})}{\partial \mathbf{R}_I \partial \mathbf{R}_J} = -\frac{\partial \mathbf{F}_I}{\partial \mathbf{R}_J} = \int \frac{\partial \rho_\mathbf{R}(\mathbf{r})}{\partial \mathbf{R}_J} \frac{V_\mathbf{R}(\mathbf{r})}{\partial \mathbf{R}_I} d\mathbf{r} + \int \rho_\mathbf{R}(\mathbf{r}) \frac{\partial^2 V_\mathbf{R}(\mathbf{r})}{\partial \mathbf{R}_I \partial \mathbf{R}_J} d\mathbf{r} + \frac{\partial^2 E_N(\mathbf{R})}{\partial \mathbf{R}_I \partial \mathbf{R}_J}. \tag{2.10}$$

The last equation basically states that for the calculation of $\partial^2 E(\mathbf{R})/\partial \mathbf{R}_I \partial \mathbf{R}_J$ it is required the calculation of the ground-state electron charge density $\rho_\mathbf{R}(\mathbf{r})$ as well as of its *linear response* to a distortion of the nuclear geometry, $\partial \rho_\mathbf{R}(\mathbf{r})/\partial \mathbf{R}_I$ [96,97]. The Hessian matrix is known as the matrix of the *interatomic force constants* and applying to it a Fourier transform, this gives the so called *dynamical matrix* of the system [9,99].

2.3 Linear response theory: RuO_2 as a case of study

In the previous section we observed that the matrix of the interatomic force constants of a system is determined by the its electron-density linear response. The aim of this section is to obtain this response from DFT by assuming that the external potential on the electrons is a differentiable function of a set of parameters, $\lambda \equiv \{\lambda_i\}$, (where λ could be $\mathbf{R}_I$ in the case of considering the dynamics of the lattice). As in the case of Eq. (2.8) and Eq. (2.9), we apply the Hellmann-Feynman theorem but now with the set of parameters λ_i instead of $\mathbf{R}_I$, obtaining the first and second derivatives of the ground-state energy

$$\frac{\partial E}{\partial \lambda_i} = \int \rho_\lambda(\mathbf{r}) \frac{\partial V_\lambda(\mathbf{r})}{\partial \lambda_i} d\mathbf{r}, \tag{2.11}$$

$$\frac{\partial^2 E}{\partial \lambda_i \partial \lambda_j} = \int \frac{\partial \rho_\lambda(\mathbf{r})}{\partial \lambda_i} \frac{\partial V_\lambda(\mathbf{r})}{\partial \lambda_j} d\mathbf{r} + \int \rho_\lambda(\mathbf{r}) \frac{\partial^2 V_\lambda(\mathbf{r})}{\partial \lambda_i \partial \lambda_j} d\mathbf{r}. \tag{2.12}$$

The electron-density response, $\partial \rho_\lambda(\mathbf{r})/\partial \lambda_i$, in Eq. (2.12) can be evaluated linearising the charge density as a function of the orbitals (Eq. (1.13)), the Kohn-sham equation in their canonical form (Eq. (1.12)), and the effective potential (Eq. (1.10)) taking into account the explicit form of V_{xc} (Eq. (1.11)) and V_C (Eq. (1.04)). The linearization is respect to the wave function, density and potential. In particular, the linearization of Eq. (1.13) leads to

$$\Delta \rho(\mathbf{r}) = 2\mathrm{Re} \sum_{n=1}^{N} \psi_n^*(\mathbf{r}) \Delta \psi_n(\mathbf{r}), \tag{2.13}$$

where the finite-difference operator Δ^λ is defined as

$$\Delta^\lambda F = \sum_i \frac{\partial F_\lambda}{\partial \lambda_i} \Delta \lambda_i \tag{2.14}$$

and the superscript λ has been omitted just for clarity. Each Kohn-Sham eigenfunction and its complex conjugate used in Eq. (2.13) are degenerate, since the external potential (both, unperturbed and perturbed) is real. Therefore, the imaginary part of the sum appearing in Eq. (2.13) vanishes.

In oder to obtain the variation of the Kohn-Sham orbitals, $\Delta \psi_n(\mathbf{r})$, we apply standard first-order perturbation theory:

$$(H_{SCF} - \epsilon_n)|\Delta \psi_n\rangle = -(\Delta V_{SCF} - \Delta \epsilon_n)|\psi_n\rangle, \tag{2.15}$$

where

$$H_{SCF} = -\frac{\hbar^2}{2m} \frac{\partial^2}{\partial \mathbf{r}^2} + V_{SCF}(\mathbf{r}) \tag{2.16}$$

is the unperturbed Kohn-Sham Hamiltonian,

$$\Delta V_{SCF}(\mathbf{r}) = \Delta V(\mathbf{r}) + e^2 \int \frac{\Delta\rho(\mathbf{r}')}{|\mathbf{r} - \mathbf{r}'|}d\mathbf{r}' + \frac{dv_{xc}(\rho)}{d\rho}\bigg|_{\rho=\rho(\mathbf{r})} \Delta\rho(\mathbf{r}), \qquad (2.17)$$

is the first-order correction to the self-consistent potential, and $\Delta\epsilon_n = \langle\psi_n|\Delta V_{SCF}|\psi_n\rangle$ represents the first-order variation of the Kohn-Sham eigenvalue ϵ_n.

The Eqs. (2.13) to (2.17) form a set of self-consistent equations for the perturbed system completely analogous to the Kohn-Sham equations in the unperturbed case (Eqs. (1.10), (1.12), and (1.13)) being Eq. (2.15) the corresponding Kohn-Sham eigenvalue equation. Focus in the perturbed case, the self-consistency requirement is manifested in the dependence of the right-hand-side on the solution of the linear system. For the left-hand-side, we have that $\Delta V_{SCF}(\mathbf{r})$ is a linear functional of $\rho(\mathbf{r})$, which also depends linearly in the $\Delta\psi$'s. Thus, the whole self-consistent calculation can be considered in terms of a generalized linear problem.

Now, the aim is to find a procedure to obtain the first-order correction to a given eigenfunction of the Schrödinger equation, given by Eq. (2.15). One way to express this function is in terms of a sum over the spectrum of the unperturbed Hamiltonian,

$$\Delta\psi_n(\mathbf{r}) = \sum_{m\neq n} \psi_m(\mathbf{r})\frac{\langle\psi_m|\Delta V_{SCF}|\psi_n\rangle}{\epsilon_n - \epsilon_m}, \qquad (2.18)$$

where we are running over all the states of the system, occupied and empty, but without taking into account the state that is being considered, in this case n. Using this form for $\Delta\psi_n$ we can express the charge-density response as following,

$$\Delta\rho(\mathbf{r}) = 2\sum_{n=1}^{N}\sum_{m\neq n} \psi_n^*(\mathbf{r})\psi_m(\mathbf{r})\frac{\langle\psi_m|\Delta V_{SCF}|\psi_n\rangle}{\epsilon_n - \epsilon_m}. \qquad (2.19)$$

In the last equation the m index is considered as counting conduction states only. This is equivalent to say that the charge-density distribution does not respond to a perturbation acting only on the occupied-state subspace, or in other words, to the component of any perturbation which couples occupied states among each other. Finally, one of the greatest advantages of LRT and DFPT, as compared to other non-perturbative methods for calculating vibrational properties of crystalline solids (like the frozen-phonon or molecular dynamics analysis methods), is that within LRT-DFPT the responses to perturbations of different wavelengths are decoupled. This important feature allows one to calculate phonon frequencies at arbitrary wave vectors $\mathbf{q}$ avoiding the use of supercells and using an approach that is essentially independent of the phonon wavelength.

As a test case of using the LRT, we performed the calculation of the lattice dynamics of bulk RuO$_2$ in the rutile structure. The results are compared with

Table 2.1: Comparison of measured and calculated frequencies of Raman-active modes (in meV)

Mode	Experiment	Theory	
	Ref. [103]	LDA	GGA
B_{1g}	20.5	22.4	23.2
E_g	65.5	66.3	60.3
A_{1g}	80.0	82.7	74.1
B_{2g}	88.7	92.7	85.3

measurements of the Raman spectra [103] as well as with the generalized phonon density of states (GDOS) obtained by inelastic neutron scattering [104]. RuO_2 has been studied previously in great detail, in order to understand the mechanism of the catalytic carbon monoxide oxidation on the $RuO_2(110)$ surface [105]. Using the optimized structural parameters, the phonon dispersion curves and the generalized phonon density of states (GDOS) have been calculated using two different xc-functionals, the LDA as given by Hedin and Lundqvist [70] and the GGA as given by Perdew, Burke, and Ernzerhof (PBE) [81]. Phonon dispersion bands are presented in the Fig. 2.1 (LDA and GGA). The analysis of the eigenvectors shows that the Ru-dominated modes are responsible for the low-lying part of the spectrum, while above 50 meV the spectrum is clearly dominated by oxygen vibrational modes.
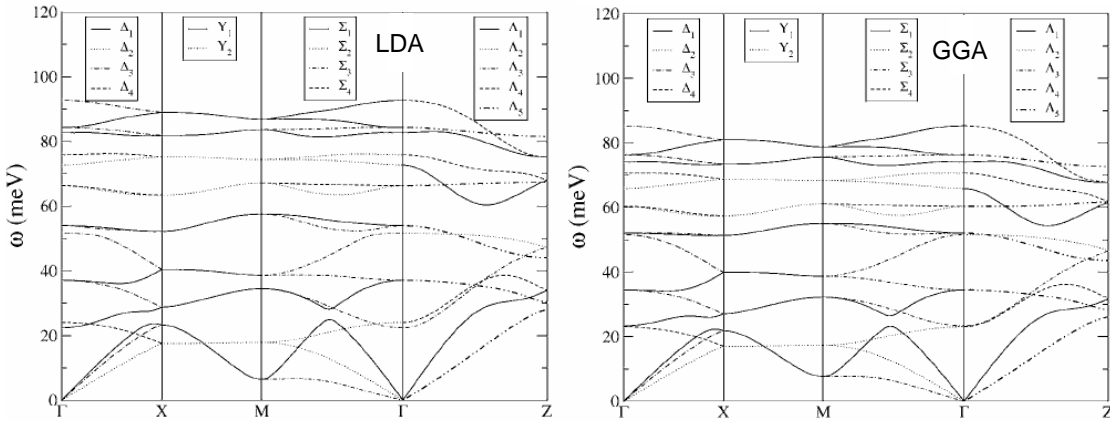
Figure 2.1: Calculated phonon dispersion curves for RuO_2 (rutile) with the LDA (left) and GGA (right) along high-symmetry lines in the first Brillouin zone.

Comparing LDA and GGA dispersions, the most striking difference is seen at the upper end of the spectrum. For the GGA the high-lying oxygen modes are located around 70 meV while in LDA calculations they show up around 80 meV. This is a very significant difference. For comparison with experimental data so far only $q = 0$ modes obtained from Raman measurements [103] are available.

These modes are listed in the Table 2.1 and compared with our calculations. As it can be seen the most prominent E_g mode is represented very well in LDA calculations, while in GGA calculations the frequency of this mode is substantially underestimated. For other modes the effect is not as drastic but, again, the LDA results are in better agreement with the experimental data than GGA. However, these measurements probe only the Γ point of the Brillouin zone; thus we do not have enough information to say anything about the quality of the LDA versus GGA. To overcome this situation we compared our calculated GDOS and the measured GDOS with neutron scattering [104].
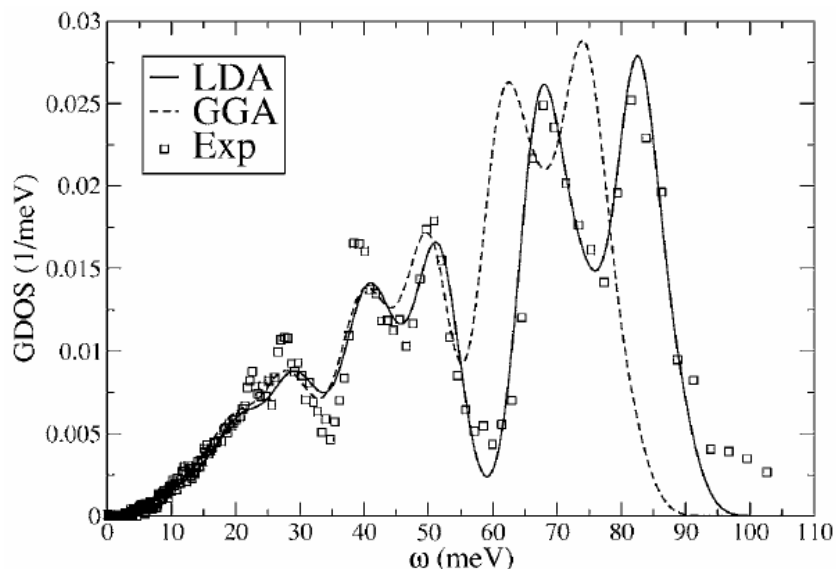

Figure 2.2: Comparison of theoretical GDOS results for the LDA and GGA with experimental data.

The Fig. 2.2 shows the comparison of the calculated and measured GDOS. We can see that in the regime up to 20 meV which is dominated by Ru vibrations modes LDA and GGA results do not differ appreciably and both agree very well with the experiment. Above roughly 20 meV the LDA and GGA start to differ more and more, with the phonon modes calculated by the GGA being much softer (lower in frequency). Above 60 meV it becomes quite obvious that the GGA results do not agree with the experiments while the LDA gives very good agreement with the measured generalized phonon density of states. In the upper part of the spectrum the GGA results are off by roughly 10 meV which is a huge discrepancy. The measurements of the GDOS support the trends already seen in the Raman measurements and indicate that these are not restricted to the Γ point in the Brillouin zone only. We can conclude that although for structural studies it seems that GGA calculations give slightly better description compared to experiment than LDA, for investigations of phonon properties LDA is clearly

preferred, at least in this particular system.

2.4   The frozen phonon approximation

The frequencies of selected phonon modes can be calculated from energy differences (or from the forces acting on atoms) produced by finite and periodic displacements (u) of a few atoms in an otherwise perfect crystal at equilibrium. A frozen-phonon calculation for lattice vibrations at a generic $\mathbf{q}$ vector requires a supercell having $\mathbf{q}$ as a reciprocal-lattice vector and whose linear dimensions must be therefore at least of the order of $2\pi/|\mathbf{q}|$. In practice, the size of the supercell that one can afford to deal with has limited the application of this technique to zone-center or selected zone-boundary phonon modes in relatively simple materials. However, zone-center phonons are also the best characterized because they may be Raman or infrared active, so that they do not require neutron or x-ray spectroscopy to be detected. By calculating the total energy for a set of displacements configurations (varying the values of u), one maps out the energy surface along this particular phonon mode. This potential curve is typically parabolic around the equilibrium configuration (small u), but for large displacements, anharmonic components in the potential become important. One can extract the frequency for this phonon mode from the potential energy curve, solving the Schrödinger equation and taking from there the two lowest energy eigenvalues that are related with the frequency [99, 106–108].

The advantages of the frozen-phonon approach are that it provides the potential for the atomic displacements and it is not limited to the harmonic approximation and it does not require any specialized computer code, as DFPT does. This technique can in fact be straightforwardly implemented using any standard total energy and force code, and only moderate care is needed in the evaluation of numerical derivatives. Nevertheless, the principal limitation is the unfavorable scaling of the computational cost with the range of the long-wavelength modes, since one needs to setup a supercell that can be quite large in order to include the corresponding distortion.

2.5   Eliashberg theory: e-ph coupling and super-conductivity

In this section we review the theoretical background of the phonon mediated superconductivity. Indeed, the description of the electron-phonon coupling mechanism is considered one of most successful models explaining *conventional* superconductivity (no high T_c's superconductors). We also discuss the most developed microscopical theory until now that tries to explain the phenomenological behavior of

the superconducting materials, that is the Eliashberg theory [1, 3, 4].

While the discovery of superconductivity occurred in 1911 [109], from a theoretical point of view, a first breakthrough occurred with the discovery of the Meissner-Ochsenfeld effect [110] (the expulsion of magnetic fields from inside a superconductor), and the understanding of that phenomenon implied that the superconducting state was a thermodynamic phase [111]. In 1950 several important developments took place; first, two independent isotope effect measurements were performed on Hg [112, 113], which indicated that the superconducting transition was intimately related to the lattice, probably through the electron-phonon interaction. Basically the way that it works is the following: changing only the isotopic mass of one species (and therefore the phonon frequencies) changes the critical temperature accordingly (decreasing the mass increases the phonon frequencies and T_c). Secondly, Fröhlich [114] studied the electron-phonon interaction in metals, using a mean-field theoretical approach for the first time. His theory correctly produced an isotope effect and moreover, predicted the discovery of the perovskite superconductors, by suggesting that the number of free electrons per atom should be reduced. He also demonstrated through second order perturbation theory, that electrons exhibit an effective attractive interaction through the phonons.

What occurs physically in the electron-phonon interaction, is that one electron makes a transition which excites a phonon, accompanied by an ionic charge density fluctuation. A second electron undergoes a transition caused by this induced charge density fluctuation. If the differences in the electron energies are small compared to the phonon excitation energy, the second electron is *actually* attracted to the first. This interaction scheme is shown in Fig. 2.3. This idea represented the starting point for the two-electron interaction in metals and used in a simplified way by the Bardeen-Cooper-Schrieffer (BCS) theory in 1957 [115, 116]. BCS considered an electron-gas as the model for a metal where the electrons, in addition to being subject to the usual screened Coulomb interaction, interact via exchange of virtual phonons. The two effects compete to respectively bind or separate a pair of electrons. Pairing electrons (also known as *Cooper pairs*) leads to a lower total energy, and the excitation spectrum of the resulting system possesses a gap, which one has to overcome to excite a single electron of a pair. By treating the e-ph interaction via the simplified model of a Cooper pair (assuming that the effective phonon-mediated interaction energy between the two electrons is negative and a constant about the Fermi surface and zero otherwise), the BCS theory was able to explain all the observed properties of a superconductor and put the pairing formalism on a firm ground.

BCS was very successful in explaining a large number of experiments, like the isotope effect, penetration depth, specific heat, the energy gap in the electronic spectrum, among others for conventional superconductors like Al, Pb, V, Nb, Ta,
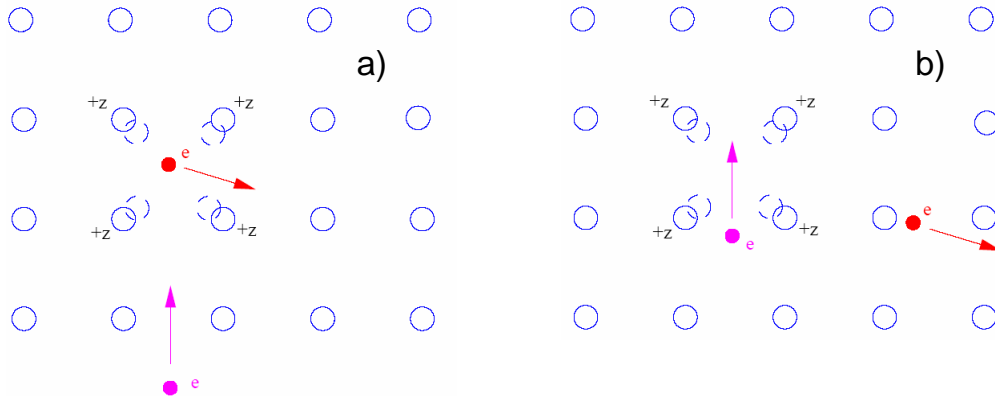
Figure 2.3: In a) one electron polarizes the lattice; in b) that electron has moved away. In the meantime a second electron (see below in a)) is attracted to the polarized region, which has remained polarized long after the first electron has left the region.

Cu, and including superconducting alloys such as Nb_3Sn. Indeed, one of the elegant outcomes of the BCS theory is the universality of various properties; at the same time this universality means that this theory really does not distinguish one superconductor from another, and more seriously, one mechanism from another. After the BCS work appeared, several works rederived their results using alternative formalisms. A remarkable one was from Gor'kov [117], who developed a Green's function method, from which the BCS results could be derived, near the superconducting transition temperature, T_c. Around the same time, tunneling became a very useful spectroscopic probe of the superconducting state [118]; besides providing an excellent measure of the gap in a superconductor, it also revealed the fine detail of the e-ph interaction [119], to such an extent that tunneling data could be inverted to tell us about the underlying e-ph interactions. The Gor'kov formalism proved to be the most useful, for the purposes of generalizing BCS theory (with its model effective interaction) to the case where the electron-phonon interaction is properly taken into account in the superconducting state. That work was developed by Eliashberg in 1960 [1].

The central quantity of the Eliashberg theory is the so-called Eliashberg spectral function, $\alpha^2 F(\omega)$, which expresses the e-ph interaction in the form of a spectral density. For phonon-mediated superconductivity it forms the essential bridge between theory and experiment. $\alpha^2 F(\omega)$ can be calculated from *ab-initio* calculations and used as input in the Eliashberg gap equations to determine T_c and the temperature-dependence of the energy gap. It can also be derived, as we said before, from experiments by inversion of tunneling spectra.

The discussion of the e-ph coupling is first focused on the isotropic limit, while

in the next part we present a brief description that contains the principal results for the anisotropic limit of the multiband case. For simplicity of the analysis, we consider the case of a single atom of mass M per unit cell. The e-ph matrix element for scattering of an electron from a Bloch state $\mathbf{k}_i$ to another Bloch state $\mathbf{k}_j = \mathbf{k}_i + \mathbf{q}$ (i and j are band indexes) by a phonon of frequency $\omega_{\mathbf{q}\nu}$ is

$$g^{\mathbf{q}\nu}(\mathbf{k}_i, \mathbf{k}_j) = \left(\frac{\hbar}{2M\omega_{\mathbf{q}\nu}}\right)^{1/2} \langle \mathbf{k}_i | \hat{\mathbf{u}}_{\mathbf{q}\nu} \cdot \nabla_{\mathbf{R}} V_{sc} | \mathbf{k}_j \rangle, \tag{2.20}$$

where $\hat{\mathbf{u}}_{\mathbf{q}\nu}$ is the phonon polarization vector, and $\nabla_{\mathbf{R}} V_{sc}$ is the gradient of the self-consistent potential with respect to atomic displacements [120]. The scattering of phonon $\mathbf{q}\nu$ by electrons give rise to a finite phonon linewidth that can be determined from the following,

$$\gamma_{\mathbf{q}\nu} = 2\pi\omega_{\mathbf{q}\nu} \sum_{\mathbf{k}_i, \mathbf{k}_j} |g^{\mathbf{q}\nu}(\mathbf{k}_i, \mathbf{k}_j)|^2 \, \delta(\epsilon_{\mathbf{k}_i} - \epsilon_F)\delta(\epsilon_{\mathbf{k}_j} - \epsilon_F). \tag{2.21}$$

The Eliashberg spectral function is given then by a sum over contributions to the coupling from each phonon mode (for each band combination i,j),

$$\alpha^2 F(\omega) = \frac{1}{2\pi N(0)} \sum_{\mathbf{q}\nu} \frac{\gamma_{\mathbf{q}\nu}}{\omega_{\mathbf{q}\nu}} \delta(\omega - \omega_{\mathbf{q}\nu}), \tag{2.22}$$

where $N(0)$ is the electronic density of states (per atom and spin) at the Fermi energy.

Once we have defined the electron-phonon matrix elements and the Eliashberg function, we can introduce the Eliashberg gap equations, which can be formulated in terms of both real and imaginary frequency axes. In the real axis formulation the superconducting gap Δ is complex and defined for all frequencies ω, while on the imaginary axis the gap is real and only defined on the discrete set of imaginary Matsubara frequencies $\omega_n = \pi T(2n - 1)$, with $n = 0, \pm1, \pm2, \dots$ and T being the temperature in energy units. The two formulations become formally equivalent by an analytic continuation of the gap itself and the gap equations [3]. In this thesis we have used the imaginary gap equations which involve two nonlinear coupled equations for the Matsubara gaps $\Delta(i\omega_n)$ and the renormalization factors $Z(i\omega_n)$. On the imaginary-frequency axis, they take the form (for an isotropic system):

$$\Delta(i\omega_n)Z(i\omega_n) = \pi T \sum_m \left[\Lambda(i\omega_m - i\omega_n) - \mu^*(\omega_c)\theta(\omega_c - |\omega_m|)\right] N_{\Delta 1}(i\omega_m), \tag{2.23}$$

$$Z(i\omega_n) = 1 + \frac{\pi T}{\omega_n} \sum_m \Lambda(i\omega_m - i\omega_n)N_{\Delta 0}(i\omega_m), \tag{2.24}$$

where θ is the Heaviside function, and $\mu^*(\omega_c)$ is the Coulomb pseudopotential opposing superconductivity. It comes with a cutoff at ω_c; to ensure convergence,

it is usually chosen ten times the maximum phonon frequency: $\omega_c \approx 10\omega_{ph}^{max}$. The functions $\Lambda(i\omega_m - i\omega_n)$, $N_{\Delta 1}(i\omega_m)$, and $N_{\Delta 0}(i\omega_m)$ which are related to the electron-phonon attraction between two electrons interacting around the Fermi energy are defined as,

$$\Lambda(i\omega_m - i\omega_n) = 2 \int_0^\infty \frac{\omega \alpha^2 F(\omega) d\omega}{\omega^2 + (\omega_n - \omega_m)^2} \equiv \Lambda(\omega_m - \omega_n) \qquad (2.25)$$

$$N_{\Delta 1}(i\omega_m) = \frac{\Delta(i\omega_m)}{\sqrt{\omega_m^2 + \Delta^2(i\omega_m)}} \qquad (2.26)$$

$$N_{\Delta 0}(i\omega_m) = \frac{\omega_m}{\sqrt{\omega_m^2 + \Delta^2(i\omega_m)}} \qquad (2.27)$$

The solution of the gap equations (2.23) and (2.24) requires as input the e-ph spectral function $\alpha^2 F(\omega)$ and the Coulomb pseudopotential $\mu^*(\omega_c)$. The first one is obtained from *ab-initio* calculations and the second one is a parameter that must be fitted in order to reproduce the experimental data.

Analytic expressions for the critical temperature (T_c) can be obtained from the Eliashberg gap equations (2.23) and (2.24) under some approximations. For example, McMillan [121] considered the integral equations in the real frequency formulation of the Eliashberg theory, involving the complex gap function $\Delta(\omega)$. By considering several approximations about the shape of the gap function McMillan was able to show that an approximate solution for the critical temperature can be written in the form

$$T_c = \omega_0 \exp\left\{ -\frac{1+\lambda}{\lambda - \mu^*(1 + (\langle\omega\rangle/\omega_0)\lambda)} \right\}, \qquad (2.28)$$

with ω_0 being the maximum phonon frequency and $\langle\omega\rangle$ being the average phonon frequency, defined as

$$\langle\omega\rangle = \frac{\int_0^{\omega_0} \alpha^2(\omega')F(\omega')d\omega'}{\int_0^{\omega_0} \alpha^2(\omega')F(\omega')d\omega'/\omega'}, \qquad (2.29)$$

and with λ as the effective mass enhancement parameter given by

$$\Lambda(m = n) = \Lambda(0) \equiv \lambda = 2 \int_0^\infty d\omega \frac{\alpha^2 F(\omega)}{\omega}. \qquad (2.30)$$

From extensive numerical studies of the integral equations, McMillan [121] was further able to show that in most cases T_c could be reproduced reasonably well by the following expression,

$$T_c = \frac{\Theta_D}{1.45} \exp\left\{ -\frac{1.04(1+\lambda)}{\lambda - \mu^*(1 + 0.62\lambda)} \right\}, \qquad (2.31)$$

where Θ_D is the Debye temperature. It is important to mention here that the Coulomb pseudopotential μ^* used in the McMillan equation is different from the one that appears in the Eliashberg equations (2.23) and (2.24). Nevertheless, there exists a relation between both pseudopotentials, scaled in the following way [2],

$$\frac{1}{\mu^*(\langle\omega^2\rangle)} = \frac{1}{\mu^*(\omega_c)} + \ln\left(\frac{\omega_c}{\langle\omega^2\rangle^{1/2}}\right) \tag{2.32}$$

where $\langle\omega^2\rangle$ is given by

$$\langle\omega^2\rangle = \frac{2}{\lambda}\int d\omega\,\alpha^2 F(\omega)\omega. \tag{2.33}$$

In practice, the value of μ^* could be considered as lying between the widely used range of 0.10 to 0.20 [121], or by fixing T_c to the experimental value in Eq. (2.31), or solve numerically the Eliashberg equation for T_c (explained later) using a standard Matsubara technique, and then obtaining μ^* [11, 32, 122].

Allen and Dynes [2] improve the McMillan equation considering results of more than 200 such numerical solutions for a number of different shapes of the Eliashberg function and values of λ from small to as large as 10^6. They basically proposed the same equation as McMillan, but with the prefactor $\Theta_D/1.45$ replaced by $\omega_{log}/1.2$. The logarithmically averaged characteristic phonon frequency ω_{log} in the Allen-Dynes formula is obtained from

$$\omega_{log} = \exp\left\{\frac{2}{\lambda}\int_0^\infty \frac{d\omega}{\omega}\alpha^2 F(\omega)\ln(\omega)\right\}. \tag{2.34}$$

This equation can be taken to represent an important measure of the average phonon frequency associated with the spectral density $\alpha^2 F(\omega)$.

As a final point, we write down the Eliashberg gap equations also in the multiband model. The reason for considering this case is that it has been demonstrated by experimental and theoretical works that the MgB_2 possesses two superconducting gaps [31, 44, 63, 64, 123–127]. The equations for a multiband system are the following (i and j being the band index),

$$\Delta_i(i\omega_n)Z_i(i\omega_n) = \pi T\sum_{m,j}\left[\Lambda_{ij}(i\omega_m - i\omega_n) - \mu_{ij}^*(\omega_c)\theta(\omega_c - |\omega_m|)\right]N_{\Delta 1}^j(i\omega_m), \tag{2.35}$$

$$Z_i(i\omega_n) = 1 + \frac{\pi T}{\omega_n}\sum_{m,j}\Lambda_{ij}(i\omega_m - i\omega_n)N_{\Delta 0}^j(i\omega_m), \tag{2.36}$$

where,

$$\Lambda_{ij}(i\omega_m - i\omega_n) = 2\int_0^\infty \frac{\omega\alpha_{ij}^2 F(\omega)d\omega}{\omega^2 + (\omega_n - \omega_m)^2} \equiv \Lambda_{ij}(\omega_m - \omega_n), \tag{2.37}$$

$$N^j_{\Delta 1}(i\omega_m) = \frac{\Delta_j(i\omega_m)}{\sqrt{\omega_m^2 + \Delta_j^2(i\omega_m)}}, \tag{2.38}$$

$$N^j_{\Delta 0}(i\omega_m) = \frac{\omega_m}{\sqrt{\omega_m^2 + \Delta_j^2(i\omega_m)}}. \tag{2.39}$$

The solution of these equations for a two gap system like MgB_2 requires as input (a) the four (but only three independent) electron-phonon spectral functions $\alpha^2_{ij}F(\omega)$ since $i, j = 1, 2$; and (b) the four (but only three independent) elements of the Coulomb pseudopotential matrix $\mu^*_{ij}(\omega_c)$.

Chapter 3

Results for the Nb-Mo alloy

3.1 Introduction

The $Nb_{1-x}Mo_x$ alloy forms a solid solution with a body-centered cubic (bcc) structure for the whole range of Mo concentrations ($0.0 \leq x \leq 1.0$) [13, 14]. The constituent elements, Nb(Z=41) and Mo(Z=42), belong to the $4d$-transition metals on the Periodic Table with 5 and 6 valence electrons, respectively. Therefore, by changing the Mo-content in the system, we obtain a continuous evolution of the number of electrons per atom (n_e). An interesting characteristic of this system is the non-monotonic behavior of the superconducting critical temperature (T_c) as a function of x. While Nb possesses the highest T_c among elemental metals (9.25 K), T_c decreases with increasing Mo-content, falling below 0.5 K for $0.4 \leq x \leq 0.9$, and slightly recovering again to $T_c = 0.92$ K for pure Mo ($x = 1$) [13–15].

The non-monotonic behavior of T_c for the Nb-Mo alloy as a function of the Mo content has motivated many experimental and theoretical studies. Indeed, there are a lot of studies on the structural [14, 19, 128–130], elastic [129, 131–134], electronic [20–24, 130, 135–137], vibrational [11, 16–18, 106–108, 138, 139], and superconducting properties [11, 13, 15, 140–142] of this alloy. It is interesting to note that the evolution of some of these properties as a function of Mo-content also shows non-monotonic behavior. The origin of these features is not yet completely understood despite all the above mentioned efforts. For example, experimental studies of the elastic properties at low temperatures show anomalies in the C' and C_{44} elastic constants around a Mo-content of $x \approx 0.4$ [129, 131–134]. This behavior was associated with an electronic topological transition of the Fermi surface as a consequence of increasing n_e. However, early tight-binding calculations of the electronic structure and elastic properties using the rigid band approximation did not reproduce the anomalies observed experimentally [129, 131–134].

Another interesting behavior comes from the vibrational properties, where the evolution of the dispersion curves with increasing Mo-content shows that the phonon anomalies are strongly dependent on the value of n_e [16–18]. For example,

a Kohn anomaly is present in the longitudinal branch $[00\zeta]$ in Nb, but not in Mo. In contrast, in Mo, a depression is found near the symmetry point H for the longitudinal and transversal branches [16–18]. The evolution of this anomaly in the $Nb_{1-x}Mo_x$ alloy was studied using coherent one-phonon scattering of thermal neutrons and it was found that at $x \approx 0.4$, the anomaly starts to disappear [18], but for higher Mo concentrations, (≥ 0.9), a depression at the H-point appears suddenly. Another example of this kind of change due to the variation of n_e occurs in the transversal-mode frequencies at the N point, where the frequencies of the transversal modes (T_1 and T_2) in Nb are 16.13 and 20.88 meV, respectively, while for Mo this ordering is reversed with the T_2 frequency at 18.78 meV and the T_1 at 23.57 meV [18].

From the theoretical point of view, the evolution of the electronic and elastic properties of the $Nb_{1-x}Mo_x$ alloy as a function of x has been studied using quasi-random structures [19], the coherent potential approximation (CPA) [20–22], and the Korringa-Kohn-Rostoker coherent potential approximation (KKR-CPA) [23, 24] approaches. However, these studies have been limited to only a few Mo concentrations, because these calculations are computationally very demanding, especially if one is interested in very low (close to Nb) or high concentrations (close to Mo). These studies [20–22,24] found an electronic topological transition (ETT) from a holelike band to an electronlike band at the Γ point of the electronic band structure between $x = 0.25$ and $x = 0.50$, but because a large disorder-induced smearing of the bands was already obtained for the $x = 0.25$ case, it was difficult to accurately identify the critical Mo-concentration (x_c) of the ETT in this alloy. A smaller range $x_c = 0.3 - 0.4$ was given by Bruno *et al.* [23], who analyzed the ETT within the rigid-band approximation using their calculated band structure for $x =0.50$ as a starting point. Now, about the superconducting properties, the T_c was calculated only in a fairly global way by expressing the electron-phonon coupling λ as a function of x in terms of the Hopfield parameter (η) [24]. Combined with the Debye temperature and assumptions about the Coulomb pseudopotential μ^*, the general trend of $T_c(x)$ was reproduced with the McMillan formula [121]. Reliable quantitative values can only be obtained, however, from a more detailed treatment of the phonon dispersion and the electron-phonon coupling.

In this chapter we present the results of the calculations of the structural, electronic, vibrational, and superconducting properties and their evolution for the $Nb_{1-x}Mo_x$ alloy, as a function of x in the whole range of the Mo concentrations ($0 \leq x \leq 1$). The results were obtained using two methodologies: the full-potential LAPW method and the MBPP pseudopotential method, both of them for two different xc-functionals, LDA and GGA. The main reason for the use of two different methodologies is the validation of the pseudopotential calculations by comparing a wide variety of properties such as the mentioned above with the

highly accurate full-potential LAPW method. The closer the MBPP calculations are to LAPW ones, the better the description of the pseudopotential is for each case under study. Additionally, and as explained early in Chapter 1, we use both functionals, LDA and GGA in order to find which one is better describing the different calculated properties. In the section 3.2 they are presented the numerical details of the calculations of the structural, electronic, vibrational and superconducting properties the Nb-Mo system. In the section 3.3, we present the results of the structural optimization of the $Nb_{1-x}Mo_x$ alloy at the BCC structure for the whole range of Mo concentrations. The results are compared with experimental data, specifically the lattice constant (a_0) and the bulk modulus (B_0). The evolution of the density of states (DOS) and the electronic band structure as a function of Mo-content are analyzed in order to determine the critical concentration of possible electronic topological transitions. That analysis is presented in section 3.4. In the section 3.5 they are presented the results of the vibrational calculations, namely, the frequencies for two high-symmetry points, H, and N (with its three different polarizations N_1, N_3, and N_4), which are compared with experimental data available in the literature. The full phonon dispersion curves and the phonon density of states (PDOS) for different values of x are also presented. The evolution of the vibrational anomalies as a function of Mo-content is analyzed. With the information obtained for the electronic and vibrational properties at the optimized lattice parameters, we have obtained the electron-phonon properties such as the Eliashberg function, $\alpha^2 F(\omega)$, the logarithmic average of the frequency, ω_{log}, the electron-phonon coupling constant, λ, and T_c as a function of x, for the $Nb_{1-x}Mo_x$ alloy. Those results are presented and analyzed in section 3.6.

3.2   Numerical details of the calculations

This section is split in two parts in order to explain in detail each step of the calculations, namely, properties obtained with *(i)* the all-electron LAPW and *(ii)* the MBPP method. For the calculation of the vibrational properties we have used the implementation of linear response theory (LRT) on the MBPP method and the frozen phonon approximation (FPA) with the LAPW method. It is important to emphasize that all the calculations performed in this thesis used two *xc*-functionals, LDA [70, 71] and GGA [81].

(i) LAPW calculations. For the all-electron calculations, the Kohn-Sham total energies were calculated using the full-potential linearized augmented plane-wave method (LAPW) [54–56] as implemented in the Wien2k code [57]. The core states were treated fully relativistically, and the semicore and valence states were computed in a scalar relativistic approximation [143]. The exchange-correlation

potential was evaluated within LDA using the Perdew-Wang form [71] and the GGA using the functional proposed by Perdew, Burke, and Ernzerhof (PBE) [81, 144, 145]. We chose muffin-tin radii (R_{MT}) of 2.25 a.u. for Nb and Mo, and a plane-wave cutoff $R_{MT} \times K_{MAX} = 9.0$. Inside the atomic spheres, the potential and charge densities were expanded in crystal harmonics up to $l = 10$. Convergence was assumed when the energy difference between the input and output steps was less than 1×10^{-6} Ry. Special attention was paid to convergence of results with respect to the number of k points. We used a grid of $23 \times 23 \times 23$ for the structural optimization and $32 \times 32 \times 32$ for the frozen phonon calculations. For the integration inside the Brillouin zone in reciprocal space we used the Gaussian smearing method with a smearing factor of 0.2 eV.
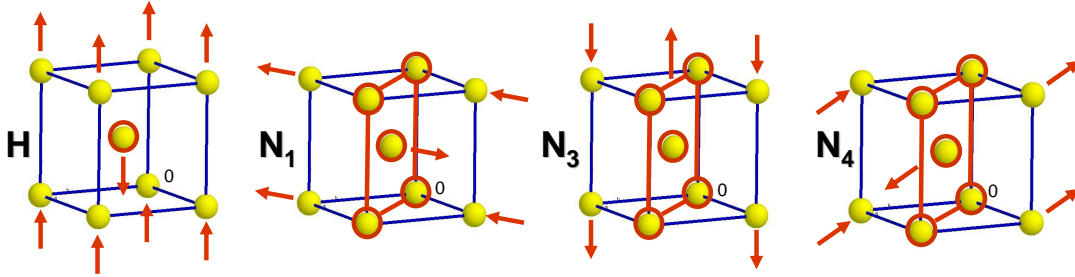

Figure 3.1: Displacement patterns on the BCC structure for the calculations of the H, N_1, N_3, and N_4 phonon modes of the Nb-Mo alloy using the frozen phonon approximation.

The vibrational properties obtained with the LAPW code were calculated using the frozen phonon approximation (FPA) [106–108], which involves the calculation of the total energy of the crystal as a function of atom displacements for a particular eigenmode. The studied phonon modes correspond to the wave vector at the H (threefold degenerated) and N high-symmetry points. In the Fig. 3.1 they are shown the different displacement patterns implemented for the BCC structure, which corresponds to the structure of the Nb-Mo alloy in the VCA approximation. In the Tables 3.1 and 3.2 we present the structural details for each distortion pattern H and N (with its three different polarizations), respectively, such as the origin of the new Cartesian system ($\vec{O}$), the lattice vectors with respect to this new origin ($\vec{a_i}$), the basis vectors ($\vec{b_i}$) including the displacement unit (u), and the corresponding space group. The energy-versus-displacement *ab initio* calculation was fitted by a sixth-order polynomial with only even terms, as required by the symmetry of the displacement patterns. The harmonic phonon frequency was then extracted from the second-order coefficient of the fitted polynomial.

(ii) MBPP calculations. As we said before, the pseudopotential calculations were performed with the mixed-basis pseudopotential method (MBPP) [58]. In this calculation we have used norm conserving pseudopotentials under the Vanderbilt scheme [93], and considered $4s$ and $4p$ semicore states as valence electrons

Table 3.1: Structural details of the H distortion pattern.

	H
$\vec{O}$	$\left(\frac{1}{4}, \frac{1}{4}, \frac{1}{4}\right) a$
$\vec{a_1}$	$(1, 0, 0) a$
$\vec{a_2}$	$(0, 1, 0) a$
$\vec{a_3}$	$(0, 0, 1) a$
$\vec{b_1}$	$\frac{1}{4}\vec{a_1} + \frac{1}{4}\vec{a_2} + \left(\frac{1}{4} + u\right) \vec{a_3}$
$\vec{b_2}$	$\frac{3}{4}\vec{a_1} + \frac{3}{4}\vec{a_2} + \left(\frac{1}{4} - u\right) \vec{a_3}$
Space group	P4/nmm-D$_{4h}^{7}$ (#129)

Table 3.2: Structural details of the N distortion patterns.

	N_1	N_3	N_4
$\vec{O}$	$\left(-\frac{1}{2}, 0, \frac{1}{2}\right) a$	$\left(\frac{1}{4}, \frac{1}{4}, \frac{1}{4}\right) a$	$\left(-\frac{1}{2}, 0, \frac{1}{2}\right) a$
$\vec{a_1}$	$(0, 0, 1) a$	$(-1, 1, 0) a$	$(0, 0, 1) a$
$\vec{a_2}$	$(1, -1, 0) a$	$(0, 0, 1) a$	$(1, -1, 0) a$
$\vec{a_3}$	$(1, 1, 0) a$	$(1, 1, 0) a$	$(1, 1, 0) a$
$\vec{b_1}$	$\frac{3}{4}\vec{a_2} + \left(\frac{1}{4} - u\right) \vec{a_3}$	$\left(\frac{1}{4} - u\right) \vec{a_2} + \frac{1}{4}\vec{a_3}$	$\left(\frac{3}{4} - u\right) \vec{a_2} + \frac{1}{4}\vec{a_3}$
$\vec{b_2}$	$\frac{1}{4}\vec{a_2} + \left(\frac{3}{4} + u\right) \vec{a_3}$	$\left(\frac{3}{4} + u\right) \vec{a_2} + \frac{3}{4}\vec{a_3}$	$\left(\frac{3}{4} + u\right) \vec{a_2} + \frac{3}{4}\vec{a_3}$
Space group	Cmma-D$_{2h}^{21}$ (#67)	Cmcm-D$_{2h}^{17}$ (#63)	Cmcm-D$_{2h}^{17}$ (#63)

which substantially improved the description of the different calculated properties in this alloy. The fairly deep potentials for Nb/Mo are efficiently treated by the mixed-basis scheme, which uses a combination of local functions and plane waves for the representation of the valence states. We used s-, p- and d-type functions at the Nb/Mo sites, supplemented by plane waves up to a kinetic energy of 36 Ry. Phonon properties are calculated via density functional perturbation theory [8, 59] as implemented in the MBPP code [9, 62]. The studies were carried out with two different approximations for the exchange-correlation functional, the LDA using the Hedin-Lundqvist form [70] and the GGA using the PBE functional [81, 144, 145]. The Brillouin-zone integration has been performed using Monkhorst-Pack special k-point sets with a Gaussian smearing of 0.2 eV. For the calculation of the ground state properties (structural optimization and electronic properties) a 20×20×20 k-point mesh was used. For the phonon calculations we have used a much denser 32×32×32 k-point mesh. Complete spectra are obtained from a Fourier interpolation of dynamical matrices calculated on an 8×8×8 q-point mesh. The same method provides access to the screened electron-phonon matrix elements, which are the ingredients of the isotropic Eliashberg theory [10, 146]. All phonon calculations are based on full structural optimization for each x with respect to the total energy. Finally, estimates for T_c are obtained

via the Allen-Dynes formula [2].

The $Nb_{1-x}Mo_x$ alloy was modeled in the self-consistent virtual crystal approximation (VCA) [25–29]. In the case of the all-electron method, the Nb ($Z=41$) sites were substituted by virtual-atoms which have a fractional electronic charge ($Z=41+x$) depending on the Mo concentration (x). The valence charge was modified by the same amount in order to maintain the neutrality of the virtual-atom. This approximation is justified since Mo has only one electron more than Nb. The potential for the VCA system is determined self-consistently for each value of x without shape approximation [57]. The self-consistent VCA within the LAPW framework has already been applied successfully to model C, Be and Al substitutions in MgB_2 [26, 27] and electron and hole doping in high-temperature superconducting compounds [28, 29]. In the same spirit, the VCA was implemented within the pseudopotential method by generating new pseudopotentials with a fractional nuclear charge ($Z=41+x$) for each x and by adjusting the valence charge accordingly. The equilibrium lattice parameter was determined by total-energy calculations for eleven Mo concentrations ($x=0.0$, 0.1, 0.2, 0.3, 0.4, 0.5, 0.6, 0.7, 0.8, 0.9 and 1.0). The structural optimization was performed with both methods, all-electron (LAPW) and pseudopotential (MBPP), and each one for both xc-functionals, LDA and GGA.
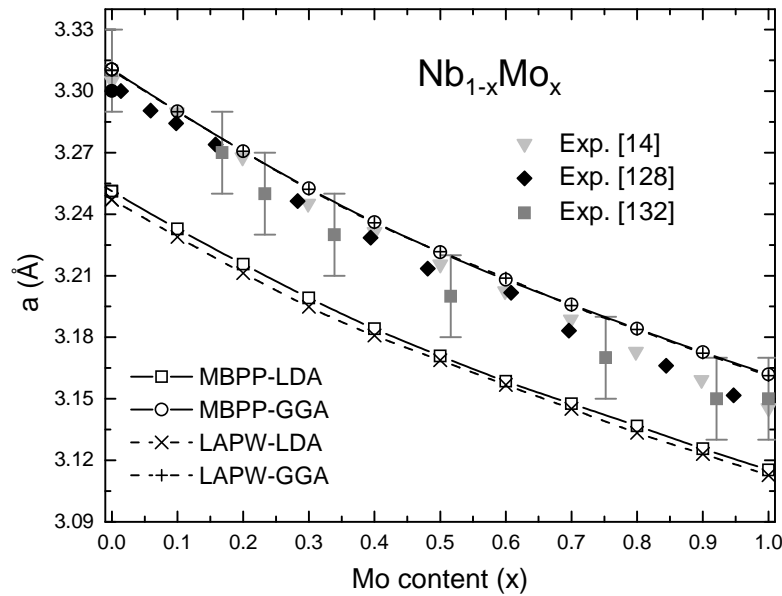
3.3 Structural properties

Figure 3.2: Evolution of lattice parameter a_0 as a function of x for the Nb-Mo system. For comparison experimental data are also included [14, 128, 132].

We present the calculated lattice parameters for the eleven x values start-

ing from $Nb(x = 0.0)$ until $Mo(x = 1.0)$. The optimal values were obtained by the minimization of the total energy as a function of volume using the Birch-Murnaghan equation of state [147]. In Figs. 3.2 and 3.3 we show the evolution of the lattice parameter, a_0, and the bulk modulus, B_0, as a function of x. The very good agreement between the two methods of calculation for the same xc-functional (LDA or GGA) indicates that the implementation of the VCA in the pseudopotential code describes very well the structural parameters of the Nb-Mo alloy. In fact, both methods with both functionals follow the trend of the experimental data [14, 128, 129, 132, 148]. The GGA results are closer to the experimental data than LDA, which is consistent with the tendency reported in the literature that GGA improves the calculation of the lattice parameters in comparison with LDA [72–77]. The largest difference between GGA calculations and the experimental data for a_0 is only 0.5%, which happens in pure Mo, comparing the MBPP-GGA value of 3.1619 Å and the experimental value of 3.1454 Å [14].
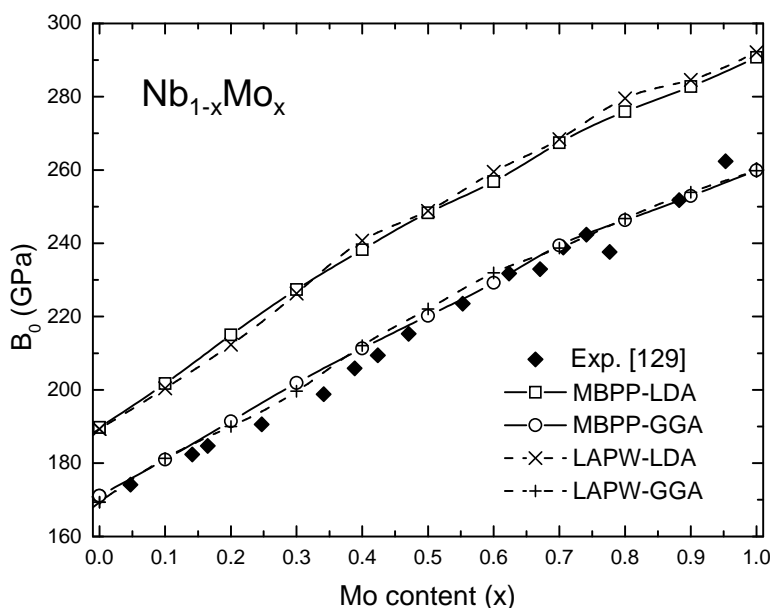

Figure 3.3: Calculated bulk modulus (B_0) for $Nb_{1-x}Mo_x$ compared with experimental results [129].

3.4 Electronic properties

In order to evaluate the effects of increasing the Mo-content on the electronic properties of the $Nb_{1-x}Mo_x$ alloy, we analyzed the evolution of the density of states (DOS) and the band structure. In Fig. 3.4 we present the DOS for the case of Nb ($x = 0$) and the DOS integral, which corresponds to the number of valence electrons of the system up to the given energy. One of the important effects of

adding Mo to Nb - and then obtaining the Nb-Mo alloy - is the shift of the Fermi level to the right on the DOS plot (see Fig. 3.4) as a result of increasing the number of valence electrons in the system (the raising of the dashed line). This is an important effect of alloying, which is captured by the simple rigid band approximation but neglects the changes in the DOS. In our case we are using the VCA, which gives us information about the changes in the shape of DOS, obtaining a broadening of the plot as a function of x (not showed here since the changes are quite small but observable) in addition to the change in the position of the Fermi level. These small effects are quite important since the position of the Fermi level is very close to a high peak, near to a shoulder, and any small change in the DOS could have a very important effect on the value of the density of states at the Fermi level, $N(E_F)$.
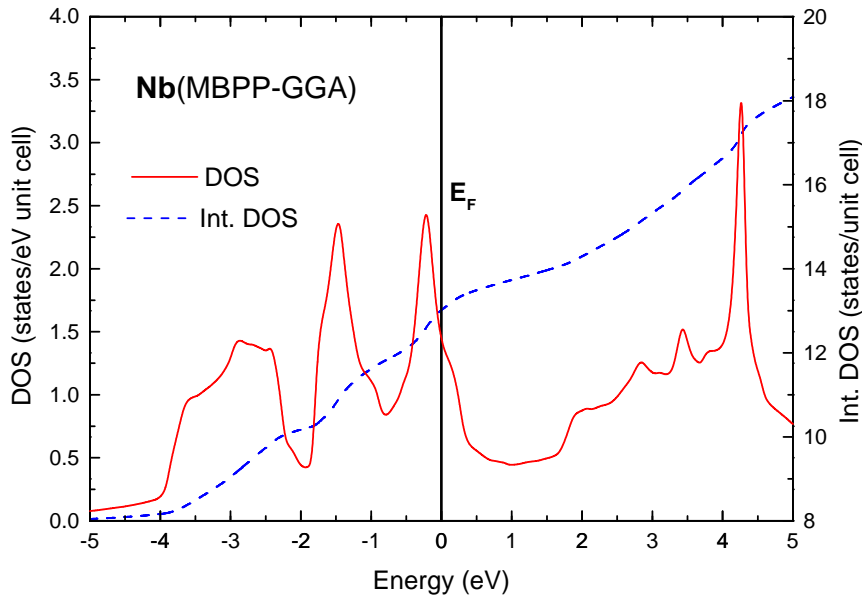

Figure 3.4: Electronic density of states, DOS, and the DOS integral for Nb corresponding to the MBPP-GGA data.

In order to see the effects of alloying on the DOS closely, in Fig. 3.5 we plotted the $N(E_F)$ as a function of x obtained with both methods (LAPW and MBPP) for each functional (LDA and GGA). We can see that $N(E_F)$ decreases as a function of x reaching the lowest value around $x \approx 0.7$, however, near to Mo it increases a little bit. We can see clearly that in the interval that corresponds to the range of $0.0 \leq x \leq 0.4$, there are some differences between methods (solid and dash lines); the differences disappear at $x = 0.4$. This result indicates that at the regime of high Mo content, the $N(E_F)$ has practically the same behavior as a function of x for both methods with both xc-functionals. From a methodological point of view, we also find a very good agreement between functionals and methods, especially

at $x \geq 0.2$. For lower x, a region that corresponds to the shoulder of the central peak, the agreement is not so good, indicating that this is a very sensitive zone.
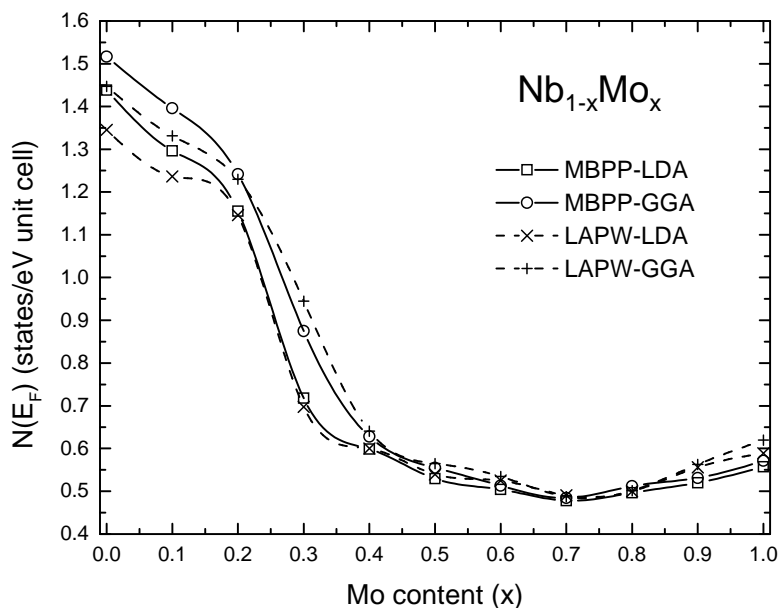

Figure 3.5: Evolution of the density of states at the Fermi level for the $Nb_{1-x}Mo_x$ system.

Another way to explore the effects of alloying on the electronic properties is the analysis of the electronic band structure. In Fig. 3.6, we show the band structures for the boundary cases under study for this alloy, $Nb(x=0)$ and $Mo(x=1)$, which correspond to the calculated MBPP-GGA data, using the calculated lattice parameters. From the band structure, it can be seen that a threefold degenerate state exists at the Γ point (E_Γ), close to the Fermi level, which lies at 0.3 eV in Nb and at -1.5 eV in Mo. Thus, in $Nb(x=0)$ the band centered at Γ is partially filled and crosses the Fermi level with hole character, but as the Mo-content is increased, it starts to fill up until a critical concentration (x_c) where this band is completely filled. For $x > x_c$, other bands are rising in that region but with electron character. This indicates that an electronic topological transition (ETT) occurs around the Γ point at x_c, since the Fermi surface corresponding to the hole-like band disappears and a Fermi surface with electron character emerges. In order to find the critical concentration x_c, we trace the evolution of the energy bands at the Γ point. In Fig. 3.7, the values of E_Γ are shown as a function of x calculated with both methods and both functionals. We find a very good agreement between both methods, MBPP and LAPW. Nevertheless, GGA gives slightly larger values for x_c than LDA (x_c is 0.28 and 0.32 for LDA and GGA, respectively). Note that this result represents an accurate determination (under the restrictions and limits of VCA) for $x_c \approx 0.3$ of the ETT, which has been conjectured from the observed anomalies in the elastic properties of this system [129].
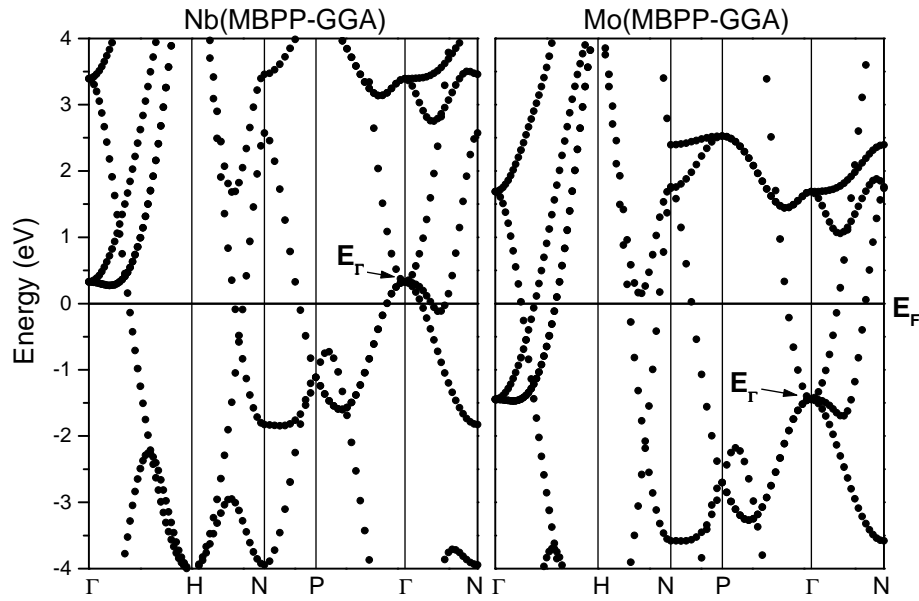
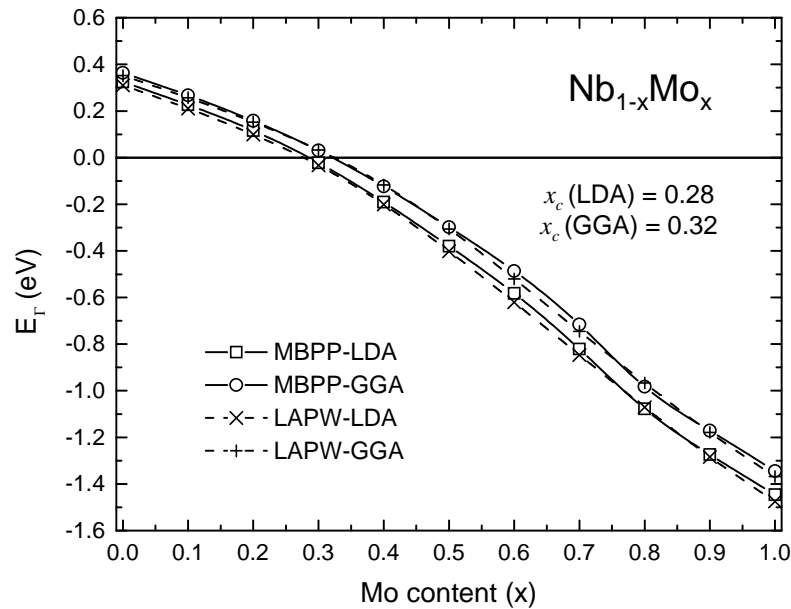Figure 3.6: Electronic band structure of Nb and Mo obtained with the MBPP-GGA method.

Figure 3.7: Evolution of E_Γ as a function of x for the $\mathrm{Nb}_{1-x}\mathrm{Mo}_x$ alloy.

3.5   Vibrational properties

In this section we present the results of the vibrational properties of $Nb_{1-x}Mo_x$ and their evolution as a function of x. In the first part we show the phonon frequencies of the Nb-Mo alloy at the H and N (with its three polarizations) high symmetry points obtained by means of the FPA using the all-electron code (LAPW) and with the LRT implemented on the pseudopotential code (MBPP). The second part corresponds to the analysis of the full-phonon dispersion curves as the Mo-content changes in the alloy. For all modes (H, N_1, N_3, and N_4), we compare the results obtained with the two methods using both LDA and GGA xc-functionals to experimental data [18].
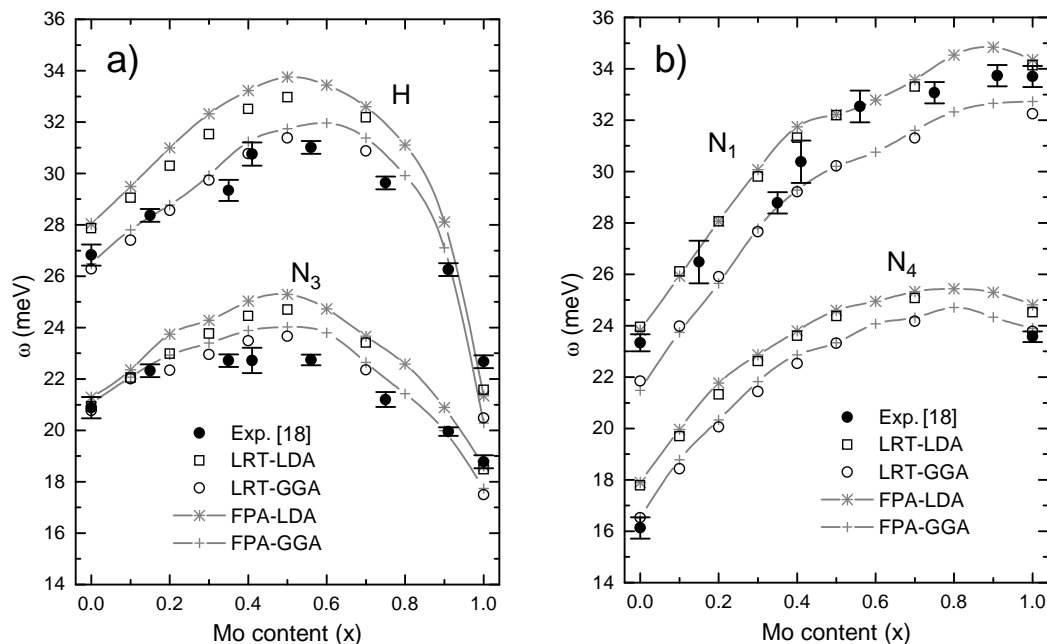

Figure 3.8: Frequency of the a) H and N_3, and b) N_1 and N_4 phonon modes for the $Nb_{1-x}Mo_x$ alloy as a function of x. Solid circles correspond to the experimental values taken from Ref. [18].

The results for the phonon frequencies at the H and N points are presented in Fig. 3.8, where the label FPA indicates frequencies obtained with the LAPW code and LRT indicates the ones obtained with the MBPP. For comparison, experimental frequencies from Powell *et al.* [18] are included. These experimental data were taken at room temperature, but it has been found that the frequencies of the H- and N-point phonons practically remain unchanged down to low temperatures [149, 150]. We see that the frequencies agree very well between the two methodologies (FPA and LRT). Furthermore, the trends of the experimental data are reproduced with both functionals, LDA and GGA. In particular, we find that VCA predicts correctly the non-monotonic dependence of the frequencies on

x. This a very remarkable result considering the fact that the VCA works as a linear interpolation of the electronic charge at the beginning of the calculation. It is important however to note that the present version of VCA a self-consistent treatment is performed, thus the charge density is redistributed for each concentration, leading then to a better description of the alloy than, for example, the rigid band approximation, which only considers the shifting of the Fermi level as the principal effect of alloying as well as previous versions of VCA where the charge density or potential for the alloy is obtained taken a weighted average of the alloying elements.

From Fig. 3.8a we can see that for both modes, H and N_3, the frequency shows a monotonic increase until $x \approx 0.4$-0.5 where it reaches a maximum, and then starts to decrease for larger x. We note that for the H mode in Mo, a slight deviation for the calculated frequency from the experimental value is observed ($\omega_{FPA-LDA}$=21.34 meV, $\omega_{FPA-GGA}$=20.28 meV, ω_{expt}=22.68$\pm$0.25 meV) despite the fact that anharmonic terms have been taken into account. Extensive tests showed that the frequency of the H-point phonon of Mo is quite sensitive to various numerical parameters, such as k-point sampling, because of the presence of an anomaly at the H point. Interestingly, both methods with both functionals give very similar frequencies (a difference less than 0.4 meV) for the N_3 mode in Nb which is also anomalous. For the N_1 mode (see Fig. 3.8b), we found a quasilinear behavior of the frequency for $x \leq 0.4$, with a large slope. In contrast to the other modes studied, the N_1 mode does not show a maximum for intermediate concentrations. Finally, for the N_4 mode, we found good agreement of our GGA results with the experimental values of the frequency for Nb and Mo. Further experimental data for intermediate concentrations for this specific mode are not available in the literature.

From the methodological point of view, we found that the range of differences between the calculated frequencies with GGA and LDA is quite broad, but it depends on the mode. For instance, for the H and N_1 modes ($\Delta\omega_{LDA-GGA} \approx$ 1.24-2.48 meV) the differences are larger than those for the N_3 and N_4 modes ($\Delta\omega_{LDA-GGA} \approx$ 0.41-1.65 meV). This indicates that the H and N_1 modes are more sensitive to the xc-functional and, in general, to the details of the description of the electronic density of the system. We find that in both methods, GGA gives lower frequencies than LDA and that GGA is in better agreement with the experimental results, with the exception of the N_1 mode where both LDA and GGA show the same level of agreement. However, more calculations for the full-phonon dispersion curves are needed in order to establish which xc-functional describes better the phonon properties of the Nb-Mo alloy system. We want to note that the differences of the frequencies between calculations and experiments could be larger if the numerical parameters (such as k-point sampling, or the

cut energy, among others) are not properly taken into account. In particular, for the FPA, the fitting procedure of the effective potential to the total-energy calculations is rather critical in order to get reliable results.
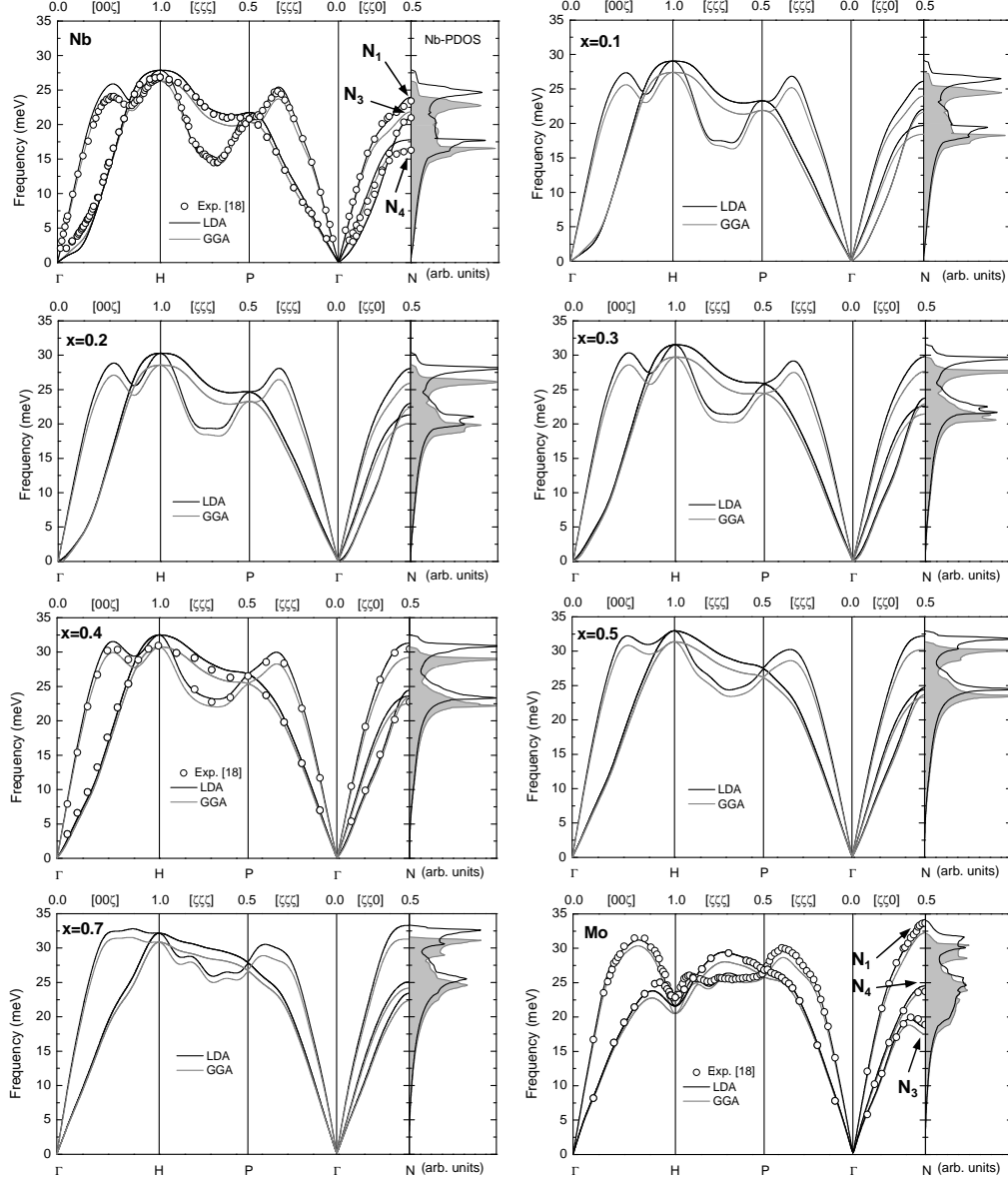

Figure 3.9: Phonon dispersion curves and phonon density of states (PDOS) for $Nb_{1-x}Mo_x$ calculated using the LDA and GGA xc-functionals. Experimental data [18] are shown by empty circles.

As we mentioned before, a detailed analysis of the full-phonon dispersion curves is needed in order to observe the evolution of the phonon anomalies at different places in the Brillouin zone as a function of x. From the experimental point of view, measurements of phonon dispersions revealed a wealth of phonon anomalies which strongly depend on the value of x [16–18] as we already mention in the intro-

duction. Thus, an interesting test of the VCA in modeling alloys is to evaluate the usefulness of this approach in describing the evolution of the phonon anomalies. In Fig. 3.9 we display the phonon dispersions together with the corresponding phonon densities of states (PDOS) for eight Mo concentrations ($x = 0.0, 0.1, 0.2,$ $0.3, 0.4, 0.5, 0.7,$ and 1.0). Results obtained with both xc-functionals, LDA and GGA, are compared with the experimental data [18]. As a general trend, the phonon spectra hardens with increasing x, which indicates a strengthening of the interatomic bonds from Nb to Mo. Comparing between the two xc-functionals, we find that GGA produces softer frequencies than LDA for all concentrations. However, both perform equally well with respect to experimental data for $x = 0.0$ and $x = 0.4$, with only a slight preference for LDA in the case of $x = 1$. From the complete dispersion curves, we can follow in more detail the evolution of the different anomalies present in $Nb_{1-x}Mo_x$ as a function of x. In particular the Kohn anomaly at the Γ-H direction and the crossing of the transversal branches at the Γ-N direction. The latter is directly connected with the reordering of the transversal frequencies at the N point mentioned above. We note that the Kohn anomaly becomes less deep as x increases and disappears for $x \approx 0.5$. In contrast, on the Mo side a strong softening occurs at the H point. For the Γ-N direction the crossing of the transverse branches moves toward the zone boundary of ζ with increasing x until for $x \approx 0.5$ it reaches the N point. For larger x the crossing disappears, while close to Mo, the lower transverse branch develops a depression in the vicinity of N. As it was mentioned before in the numerical details section, the method that we used to obtain the full-phonon dispersion curves provides access to the screened electron-phonon matrix elements, which are the ingredients of the Eliashberg theory [10, 146]. The study of such properties is discussed on the following section.

3.6   Superconducting properties

We now discuss our results for the electron-phonon coupling properties of the $Nb_{1-x}Mo_x$ alloy. In Fig. 3.10 we show the calculated electron-phonon spectral functions $\alpha^2 F(\omega)$. We can see that increasing x, the weight of the spectra is decreasing gradually until $x \approx 0.7$, before recovering again for Mo. The shape of the spectra reflects the underlying PDOS, which explains the shift to higher frequencies when x increases, as well as the fact that the LDA spectra are always harder than the corresponding GGA ones. Experimental information about $\alpha^2 F(\omega)$ is only available for Nb [5, 151–153]. Results from different tunneling experiments for Nb [5, 151–153] are depicted in Fig. 3.10 with symbols. While there is reasonable agreement for the low-frequency region, theory and experiments clearly differ with respect to the intensity of the high-frequency (longitudinal) peak. Theory predicts

a significantly larger coupling of the longitudinal phonons than seen in all experiments. This discrepancy has also been found in previous calculations of Savrasov *et al.* [10,11] and Bauer *et al.* [141]. Early attempts to link it to difficulties related to the tunneling technique (e.g. preparation of high-quality junctions) have been discarded by extensive studies [5, 153]. This points to a currently unidentified shortcoming in the theoretical approach.
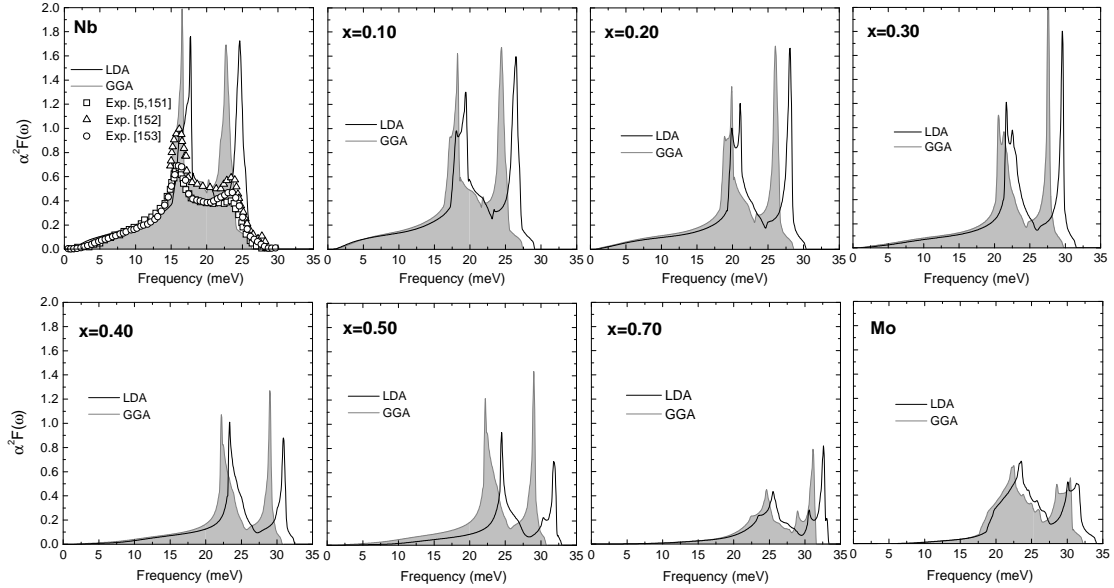

Figure 3.10: Eliashberg function $\alpha^2 F(\omega)$ for $Nb_{1-x}Mo_x$ calculated using the LDA and GGA xc-functionals. Symbols refer to spectra extracted from tunneling experiments [5, 151–153].

The spectral functions determine the electron-phonon mass enhancement parameter $\lambda(x)$ and the average effective frequency $\omega_{log}(x)$. The evolution of these two quantities together with the density of states at the Fermi level $N(E_F)$ are shown in Fig. 3.11. Both xc-functionals result in very similar $\lambda(x)$. For small x, λ decreases almost linearly until $x \approx 0.4$, passes a shallow minimum in the range $0.4 \leq x \leq 0.7$ before increasing slightly toward $x = 1$ (Mo). A very similar behavior is exhibited by $N(E_F)$, which indicates that the variation of λ with x is predominantly determined by the variation of $N(E_F)$, and to a much lesser degree by the variation of the electron-phonon coupling. The effective phonon frequency used in the Allen-Dynes formula is always higher for LDA than for GGA, a feature that comes from the harder phonon spectrum for LDA. The increase of $\omega_{log}(x)$ from Nb to Mo essentially occurs in the region $0.2 \leq x \leq 0.7$, while $\omega_{log}(x)$ stays almost constant otherwise.

In comparison with previous theoretical work, our value of λ=0.41 for Mo (LDA and GGA) agrees very well with that obtained by Savrasov *et al.* (λ=0.42) [11]. Similarly, for Nb we obtain $\lambda_{LDA} = 1.34$ and $\lambda_{GGA} = 1.31$, very close results

to the value found by Bauer *et al.* (λ=1.33) [141]. While a slightly smaller value
was reported by Savrasov *et al.* (λ=1.26) [11]. This difference can be traced back
to the use of the experimental lattice constant in the calculation of the electron-
phonon coupling in the latter work [11], while in the present calculation as well as
by Bauer *et al.* [141] the calculated lattice constant was chosen. The theoretical
values of λ for Nb are approximately 20% larger than those deduced from tunneling
experiments (1.04 [5], 1.22 [154], 0.95-1.09 [153]), which is a direct consequence of
the overestimation of the high-frequency part of the Eliashberg function discussed
above. It is important to mention that in contrast to the tunneling experiments,
from a de Haas-van Alphen experiment [155] a value of $\lambda = 1.33$ was extracted,
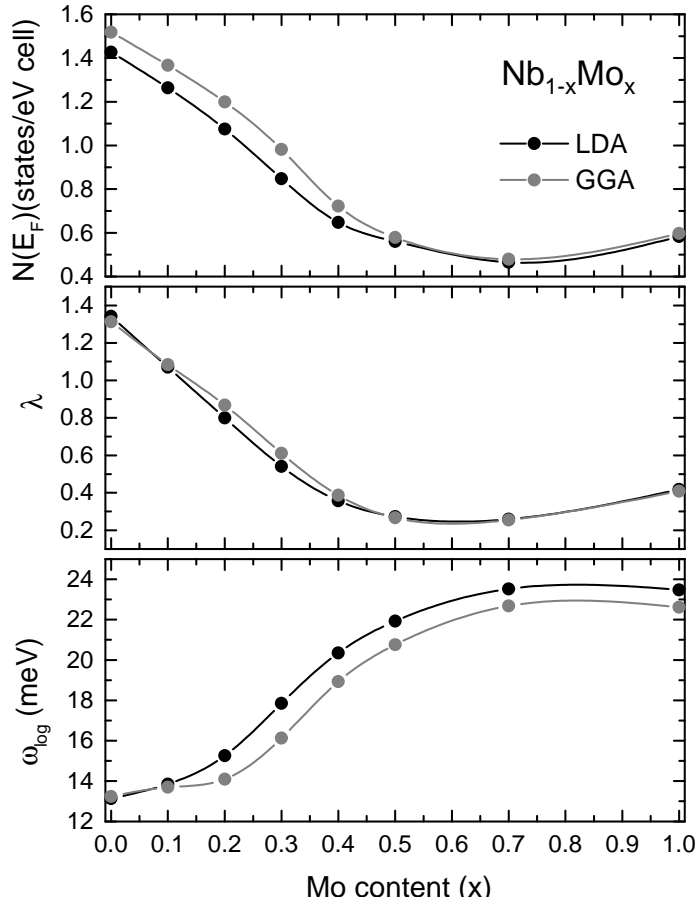which is in close agreement with the theory.

Figure 3.11: Evolution of $N(E_F)$, λ, and ω_{log} as a function of x for the $Nb_{1-x}Mo_x$
alloy.

The superconducting critical temperature $T_c(x)$, was obtained using the Allen-
Dynes formula [2] [1]. Beside the quantities $\lambda(x)$ and $\omega_{log}(x)$ discussed above, it re-

---

[1]To check the accuracy of the Allen-Dynes formula in the strong coupling regime, we also
solved the exact gap equation for the boundary cases of the alloy, Nb and Mo. The obtained

quires the knowledge of the Coulomb pseudopotential (μ^*), which is the only phenomenological parameter. We have considered two different interpolation schemes to estimate the dependence of μ^* with the alloy concentration (x). The first one consists of a simple linear interpolation, $\mu^*(x) = (1-x)\mu^*_{\text{Nb}} + (x)\mu^*_{\text{Mo}}$, between the values of μ^* for Nb and Mo. The boundary values were chosen to fit the experimental T_c of 9.25 K for Nb and 0.92 K for Mo, giving $\mu^*_{\text{N}b}$=0.224(0.219) and μ^*_{Mo}=0.119(0.112) for LDA(GGA). Note that our $\mu^*_{\text{N}b}$ is larger than the value obtained from inversion of the tunneling data ($\mu^* \approx 0.15 - 0.19$ [153]). This is a consequence of the larger theoretical value of λ, and has been noted before by Savrasov *et al.* [11]. The second scheme is based on the representation $\mu^*(x) = U_c(x)N(E_F, x)$ proposed by Gladstone *et al.* [156]. Here we combine our calculated values for $N(E_F, x)$ with a linear interpolation of $U_c(x)$. The boundary values $U_c(\text{N}b) = 0.158(0.144)$ and $U_c(\text{M}o) = 0.205(0.188)$ for LDA(GGA), are again chosen to reproduce the T_c's of Nb and Mo, respectively.
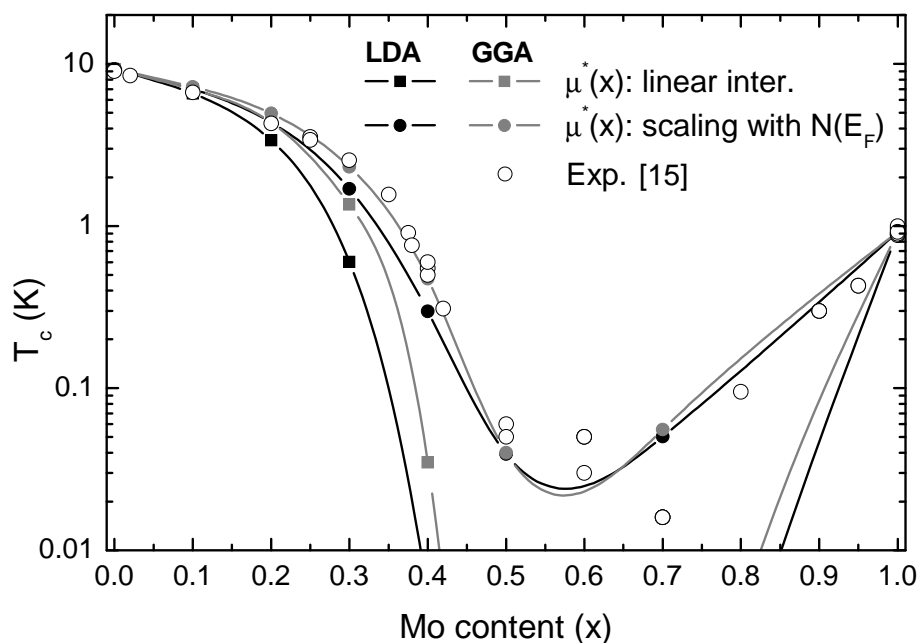

Figure 3.12: Calculated $T_c(x)$ on a logarithmic scale for $\text{Nb}_{1-x}\text{Mo}_x$ alloy using two different interpolation schemes for $\mu^*(x)$, see text. For comparison, experimental data from Refs. [15] are shown as open symbols.

In Fig. 3.12 we present the evolution of T_c as calculated with the two different interpolations of $\mu^*(x)$ for both LDA and GGA, and compare them with experimental data [15]. With both schemes, the experimental trend is well reproduced, that is, a reduction of T_c for small x, a minimum at $x \approx 0.5$-0.7, and then an

_____

differences in T_c of $\approx 3\%$ and 5% for Nb and Mo, respectively, are negligible for the purpose of the present study.

increase toward $Mo(x = 1)$. Nevertheless, the linear interpolation scheme performs poorly for intermediate values of x if we look carefully the comparison with experimental data. For example, this scheme gives a minimum value for T_c of the order of 10^{-6} at $x = 0.5$. However, a much improved description is obtained for the case of scaling of $\mu^*(x)$ with $N(E_F, x)$ for both xc-functionals, LDA and GGA, with a slightly better agreement for GGA in the region $x \leq 0.5$.

Chapter 4

Results for the $\mathrm{Mg}_{1-x}\mathrm{Al}_x\mathrm{B}_2$ and $\mathrm{MgB}_{2(1-x)}\mathrm{C}_{2x}$ alloys

4.1 Introduction

In 2001 it was reported the discovery of superconductivity in the intermetallic compound MgB_2 with a $T_c \approx 39$ K [30]. This discovery has motivated a lot of activity in the scientific community, on both, experimental and theoretical, stimulating a renewed interest in intermetallic superconducting materials. Although its T_c is not so spectacular compared with the high-T_c superconductors (as high as 160K under pressure in some cases), MgB_2 possesses the highest T_c for an intermetallic material. Additionally, it shows a simple structure (hexagonal AlB_2 type, space group P6/mmm D_{6h}^1 #191), which consists of intercalated graphite-like boron layers with hexagonal magnesium planes, a property that makes it very easy to study and prepare in the laboratory (see Fig. 4.1). From the technological point of view, MgB_2 has convenient mechanical properties (malleability as an example) that make it as strong candidate to be applied in superconducting devices [157].
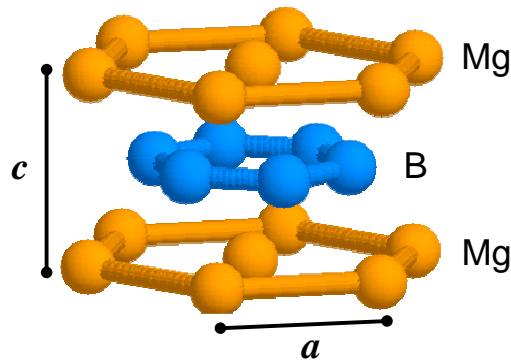

Figure 4.1: MgB_2 unit cell. The light color spheres represent Mg atoms and the dark color ones are B atoms.

As soon as MgB_2 was found to be superconducting, its electronic properties were studied [158, 159]. The electronic band structure consists of two bonding σ bands corresponding to in-plane $s - p_x - p_y$ (sp^2) hybridization in the boron layer and two π bands (bonding and anti-bonding) formed by hybridized boron p_z orbitals. Both σ and π bands have strong in-plane dispersion due to the large overlap between all p orbitals (both in-plane and out-of-plane) for neighboring boron atoms. The interlayer overlap is much smaller, especially for the $p_x - p_y$ orbitals.

The peculiar feature of MgB_2 is the incomplete filling of the two σ bands corresponding to strongly covalent, sp^2-hybrid bonding within the graphite-like boron layer. The holes at the top of these σ bands show a notably two-dimensional character and are localized within the boron planes. In contrast, the electrons and holes in the π bands are mostly three-dimensional and are delocalized over the entire crystal. The unfilled σ bands, together with weak k_z dispersion, give as a result the appearance of two nearly cylindrical sheets of the Fermi surface around the $\Gamma - A$ line. The π bands form two planar honeycomb tubular networks that consist of an anti-bonding electron-type sheet centered at $k_z = 0$ and a similar, but more compact, bonding hole-type sheet centered at $k_z = \pi/c$, c being the distance between boron planes. These 2D covalent and 3D metallic-type states contribute almost equally to the total density of states (DOS) at the Fermi level, while the unfilled covalent σ-bands experience strong interaction with the longitudinal vibrations in the boron layer [158–160].

It is now generally accepted that MgB_2 is a phonon-mediated BCS-Eliashberg superconductor with multiple gaps and strong electron-phonon (e-ph) coupling [161–163]. The e-ph coupling in MgB_2 is resulting mainly from the interaction of the σ-band orbitals and the B-B bond stretching modes with E_{2g} symmetry at Γ) [161, 163]. This general picture is supported by a wealth of experimental evidence, and its good agreement with first principles calculations [164, 165]. Since the E_{2g} phonon mode lies at Γ in the Brillouin zone, initial experimental verification of phonon behavior came from Raman spectroscopy, which is a useful and sensitive technique to study zone center phonons. Experiments [32, 166–168] showed a very broad band line-width for the phonon mode and a strong softening (≈ 50 mev) relative to AlB_2 (which is not a superconductor) [32]. This provided early experimental confirmation of the picture of strongly coupled (broad and soft) E_{2g} modes at Γ. Since the Raman scattering is restricted to the Brillouin zone center ($\mathbf{q} = 0$), then this technique is only able to access a limited number of the available phonon modes. However, given the strong dispersion and line-width changes expected in MgB_2, it is of great interest to observe the momentum dependence of the phonon properties (e.g. $\omega(\mathbf{q})$). The first investigations with of phonon dispersion in MgB_2 were calculations carried out by different groups

nearly simultaneously [31–34]. All these groups came to similar general conclu-
sions, namely that the dominant effect in the phonon spectrum was the strong
electron-phonon coupling of E_{2g} modes to the σ-band Fermi sheets about the $\Gamma - A$
line. This coupling leads to relatively soft and broad modes in the region where
$|\mathbf{q}| < 2k_F$, with k_F being the radii of the cylindrical σ-band Fermi surfaces. From
the MgB_2 full-phonon dispersion plot [32] it can be observed the strong softening
of the E_{2g} mode along $\Gamma - A$, in comparison with AlB_2, and the very similar struc-
ture of the low-energy phonon region of these two compounds. Measurements of
phonon spectra in pure MgB_2 have been carried out by two groups using inelastic
x-ray scattering (IXS) [164, 165]. Shukla *et al.* [164] showed that the broad band
line seen in the Raman data was present at several points along the $\Gamma - A$ line.
However, no measured values for the E_{2g} line-width away from the $\Gamma - A$ line were
reported. More recently, Baron *et al.* [165] showed that the softening of the E_{2g}
mode, on moving from large momentum transfers toward Γ, and the increase of
the line-width were well correlated and in good agreement with calculations. They
also showed that the temperature dependence of the phonon spectra containing
the E_{2g} mode was small.

Another interesting feature that has attracted attention of many authors is the
anharmonicity of the E_{2g} phonon modes [33,34,63,169]. In general, anharmonicity
can be expected to lead to shifts of phonon frequencies relative to the harmonic
calculation, generating additional contributions to the phonon line-width and,
possibly, strong temperature dependence. The strong T-dependence in the Raman
spectra might have helped to focus attention on this aspect [168]. However, due to
the good agreement between the experimental data and harmonic calculations of
the full-dispersion phonon plots [161,170], it is clear that predictions of rather large
(15-25%) hardening of the E_{2g} modes, due to anharmonicity are not supported.

As we mention previously, after the discovery of superconductivity in MgB_2,
the e-ph coupling was estimated and then it was suggested that MgB_2 is a stan-
dard BCS superconductor [159, 163], where the coupling with longitudinal vi-
brations on the B planes is the driving force for the superconductivity in this
compound. The related phonons were soon identified as two optical E_{2g} modes,
and that was confirmed by the e-ph coupling calculation by An and Pickett [158].
After this publication, some groups started to work on the calculation of the
e-ph coupling spectral function, $\alpha^2 F(\omega)$, including for this purpose the contribu-
tion of all electronic bands and all phonons on the same footing [31, 32, 63, 123].
However, experimental reports on MgB_2 were not consistent with a conventional
strong coupling scenario [171–178]. In particular, it was observed that the spe-
cific heat [172, 179] and tunneling [178] measurements were easy to explain if two
superconducting gaps are assumed instead of one. Liu *et al.* [63] concluded that
there are in fact, two distinctive gaps associated with the σ and π Fermi surfaces.

Then, with this evidence, the results for the Eliashberg function were broken in a 2×2 e-ph coupling matrix [31, 63, 64]. In the same direction, in a paper by Geerk *et al.* [127], the e-ph spectral function for MgB_2 was obtained experimentally by tunneling spectroscopy, and compared with *ab-initio* LDA calculations in the two-gap scheme. By comparing experiments and calculations, it was possible to identify the character of the contributions to the different peaks shown in the experimental spectra. The theoretical justification for the two-band superconductivity comes from the fact that the system is highly anisotropic and the E_{2g} phonons couple strongly to the holes at the top of the σ bands, while the three dimensional π electrons couple only weakly to the phonons [158]. The different coupling strengths of the σ- and π-bands lead to different superconducting gaps in character and size [31, 32, 63, 123].

The search for superconductivity in MgB_2 related systems is another very active research subject. One of the first studies in this direction was the substitution of Mg by Al. It was found to cause a decrease of the interplanar distance and a very small reduction of the distance between atoms in the same plane. More drastic is the reduction of the superconducting critical temperature, T_c, as a function of x in the $Mg_{1-x}Al_xB_2$ alloy, for $x \geq 0.5$ where the system loses the superconducting state [35–38]. This behavior was successfully explained by first principle calculations, using the virtual-crystal approximation, with the main reason of the T_c reduction being the filling effect of the σ-bands as a function of x [27]. Another interesting MgB_2-based system is the $MgB_{2(1-x)}C_{2x}$ alloy, which presents a nearly constant behavior in the c lattice parameter, and a larger decrease of the a parameter, in comparison with the Al-case. The C-doped system shows a stronger reduction of T_c as a function of x, since $T_c \approx 0$ for $x \geq 0.15$ [39, 40, 42, 43]. The difference in the evolution of the lattice parameters between Al- and C-systems indicates that although both are electron doped systems, the doping site is crucial in the understanding of the behavior of their properties as a function of doping.

The superconducting properties of MgB_2, such as e-ph coupling and T_c, are influenced by doping in several ways, for instance the changes in the electronic band structure that has direct impact on the electronic density of states, a key ingredient in the superconducting properties. Furthermore, the electronic change also influences the phonon properties, like the renormalization of the E_{2g} phonon frequency in $Mg_{1-x}Al_xB_2$, which has been demonstrated by Raman scattering measurements, where it was found that the frequency increases as a function of x, from ≈ 73 meV (MgB_2) until 123 meV (AlB_2) [32, 52, 53]. In the case of C-doped system, so far there are not reliable phonon characterizations as a function of x.

According to the reduction of T_c with doping in $Mg_{1-x}Al_xB_2$ and $MgB_{2(1-x)}C_{2x}$, it has also been observed the decrease of the superconducting gaps Δ_σ and Δ_π with x in these alloys. In Al-doped single crystals and polycrystals it is clear that

the σ and π gaps do not merge even for $T_c(x)$ as low as 10 K [44–48], indicating that the interband scattering $\Gamma_{\sigma\pi}$ (a quantity that induces the merging of gaps) turns out to be rather small, especially at high doping levels, and in any case insufficient to produce the merging. For the case of C-doped system, the situation is not so clear, since the $\Gamma_{\sigma\pi}$ effect is only observed in a set of C-doped single crystal samples [45, 48] but not in others [47, 49–51]. Then, in general it seems that substitutions of Mg by Al and B by C, the band filling effects are largely dominant and partially mask any other effects like $\Gamma_{\sigma\pi}$.

In this chapter we present results of the structural, electronic, vibrational, and superconducting properties for the $Mg_{1-x}Al_xB_2$ and $MgB_{2(1-x)}C_{2x}$ systems, as a function of the Al and C-content (x). The results were obtained using two methodologies, the full-potential LAPW method, and the MBPP pseudopotential method, and in both cases the LDA and GGA xc-functionals. In the section 4.2 of this chapter there is the description of the numerical details for the calculations performed on the Al and C-doped MgB_2 systems. We present in the section 4.3 the results of the structural optimization of the hexagonal unit cell for the systems under study, for fourteen Al concentrations from $x = 0$ to $x = 1$ and for thirteen C concentrations from $x = 0$ to $x = 0.3$. These results are compared with experimental data, specifically the lattice constants a_0 and c_0. The evolution of the density of states (DOS) and electronic band structure as a function of Al and C-content are analyzed in order to determine the critical concentration of possible topological transitions. This analysis is presented in the section 4.4. In the section 4.5 they are presented the vibrational calculations for the two systems, namely, the frequencies of the E_{2g} phonon mode at Γ, which are compared with experimental data available in the literature. The full-phonon dispersion curves for different values of x are also presented in section 4.5. Finally, from the results for the electronic and vibrational properties at the calculated lattice parameters, we have obtained the electron-phonon properties using the two gaps model, such as the Eliashberg function, $\alpha_{ij}^2 F(\omega)$ and the electron-phonon coupling constant, λ_{ij}. They are used as input (together with the proposed Coulomb pseudopotential matrix μ_{ij}^*) for the solution of the Eliashberg gap equations on the imaginary axis (Matsubara frequencies), obtaining then the superconducting gaps, Δ_σ, Δ_π and the value of T_c as a function of x, for the $Mg_{1-x}Al_xB_2$ and $MgB_{2(1-x)}C_{2x}$ alloys. The results for the e-ph coupling and superconducting properties are presented in section 4.6.

4.2 Numerical details of the calculations

As in the case of the previous chapter with the Nb-Mo alloy, we applied two different methodologies in order to test the implementation of VCA in the pseu-

dopotential method: *(i)* the all-electron LAPW and *(ii)* the MBPP method. As before, for the calculation of the vibrational properties we have applied the implementation of linear response theory (LRT) on the MBPP method and used the frozen phonon approximation (FPA) with the LAPW method. For the calculated properties of these alloy systems we also used two *xc*-functionals, LDA [70, 71] and GGA [81].

(i) LAPW calculations. For the all-electron calculations, we chose muffin-tin radii (R_{MT}) of 1.8 a.u. for Mg/Al and 1.4 a.u. for B/C and a plane-wave cutoff $R_{MT} \times K_{MAX} = 9.0$. Inside the atomic spheres the potential and charge density were expanded in crystal harmonics up to $l = 10$. Convergence was assumed when the energy difference between the input and output steps was less than 1×10^{-6} Ry. Special attention was paid to convergence of results by performing the calculations for a sufficiently large number of k-points, using a grid of $17 \times 17 \times 10$ for the structural optimization and $18 \times 18 \times 15$ for the frozen phonon calculations. We use the Gaussian smearing method for the Brillouin-zone integration with a smearing factor of 0.2 eV. The vibrational properties obtained with the LAPW code were calculated using the frozen phonon approximation (FPA) [106–108]. The studied phonon mode using this method is the E_{2g}-mode at Γ.
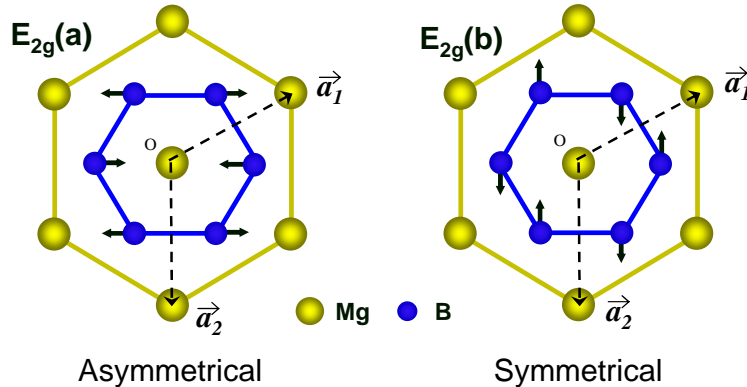

Figure 4.2: MgB_2 displacement patterns corresponding to the degenerate E_{2g} phonon mode, (*a*)-asymmetrical and (*b*)-symmetrical.

In Fig. 4.2 they are shown the different displacement patterns for both polarization states of this E_{2g}-mode. Because they are degenerate at Γ, we only performed the calculation of the symmetric one, $E_{2g}(b)$. In Table 4.1 we show the structural details for the E_{2g} distortion patterns, the lattice vectors ($\vec{a_1}$ and $\vec{a_2}$), and the basis vectors ($\vec{b_1}$ and $\vec{b_2}$) including the displacement unit (u). We performed seven different distortions u for each x. The energy-versus-displacement surface was fitted by a sixth-order polynomial with only even terms, as required by the symmetry of the displacement pattern [33, 34]. The harmonic phonon frequency was then extracted from the second-order coefficient of the fitted polynomial using $\hbar/a_0\sqrt{2a_2/m_B}$, where a_0 is the lattice parameter of the distorted

cell, a_2 is the second-order coefficient of the fitted polynomial and m is the mass of the boron atom (or virtual element, in the case of C-doped system).

Table 4.1: Structural details of the distortion patterns corresponding to the $E_{2g}(a)$ and $E_{2g}(b)$ phonon modes.

	$E_{2g}(a)$	$E_{2g}(b)$
$\vec{a_1}$	$(1,0,0)\,a$	$(1,0,0)\,a$
$\vec{a_2}$	$(0,1,0)\,a$	$(0,1,0)\,a$
$\vec{c}$	$(0,0,1)\,a$	$(0,0,1)\,a$
$\vec{b_1}$	$\left(\frac{1}{3}\pm\frac{2}{\sqrt{3}}u\right)\vec{a_1}+\left(\frac{2}{3}\pm\frac{1}{\sqrt{3}}u\right)\vec{a_2}+\frac{1}{2}\vec{c}$	$\frac{1}{3}\vec{a_1}+\left(\frac{2}{3}\pm u\right)\vec{a_2}+\frac{1}{2}\vec{c}$
$\vec{b_2}$	$\left(\frac{2}{3}\mp\frac{2}{\sqrt{3}}u\right)\vec{a_1}+\left(\frac{1}{3}\mp\frac{1}{\sqrt{3}}u\right)\vec{a_2}+\frac{1}{2}\vec{c}$	$\frac{2}{3}\vec{a_1}+\left(\frac{1}{3}\mp u\right)\vec{a_2}+\frac{1}{2}\vec{c}$
Space group	Cmmm-D$_{2h}^{19}$ (#65)	P2/m-C$_{2h}^{1}$ (#10)

(ii) MBPP calculations. The pseudopotential calculations were performed with the mixed-basis pseudopotential method (MBPP) [58]. For B/C and Mg/Al the pseudopotentials were constructed according to the description of Vanderbilt [93]. For the calculations we have included partial core corrections for the generation of all pseduopotentials. The fairly deep potentials for B/C and Mg/Al are efficiently treated by the mixed-basis scheme, which uses a combination of local functions and plane waves for the representation of the valence states. We use s and p-type functions at the B/C sites, supplemented by plane waves up to a kinetic energy of 16 Ry and a G_{MAX} parameter of 28. Phonon properties are accessed via density functional perturbation theory [8, 59] as implemented in the MBPP code [9,62]. The studies were carried out with two different approximations for the exchange-correlation functional, the LDA using the Hedin-Lundqvist form [70] and the GGA using the PBE functional [81, 144, 145]. The Brillouin-zone integration has been performed using Monkhorst-Pack special k-point sets with a Gaussian smearing of 0.2 eV. For the calculation of the ground state properties and phonons a 18×18×18 k-point mesh was used. Complete Eliashberg spectra in the two gaps model (σ and π) were obtained from a Fourier interpolation of dynamical matrices, calculated on a much denser grid of 36×36×36 k-point mesh, with a 6×6×6 q-point mesh. The same method provides access to the screened electron-phonon matrix elements, which are the ingredients of the Eliashberg theory [10, 146]. All phonon calculations are based on full structural optimization for each x with respect to the total energy. Once we have $\alpha_{ij}^2 F(\omega)$, the Eliashberg gap equations were solved in the two gaps model (see section 2.5 for details) in order to obtain Δ_σ, Δ_π, and T_c [1].

The $Mg_{1-x}Al_xB_2$ and $MgB_{2(1-x)}C_{2x}$ alloys were modeled in the self-consistent virtual-crystal approximation (VCA) [25–29], in the same way as described in the section 3.2 for the $Nb_{1-x}Mo_x$ alloy. Nevertheless, we want to note that in the present case, the virtual-atom with fractional atomic number is only at the Mg or

B site, for Al or C doping, respectively. Thus, the equilibrium lattice parameters were determined by total-energy calculations for fourteen Al-concentrations for $\mathrm{Mg}_{1-x}\mathrm{Al}_x\mathrm{B}_2$ (x=0.0, 0.1, 0.2, 0.25, 0.3, 0.35, 0.4, 0.5, 0.55, 0.6, 0.7, 0.8, 0.9, 1.0) and for thirteen C-concentrations for $\mathrm{MgB}_{2(1-x)}\mathrm{C}_{2x}$ (x=0.0, 0.025, 0.05, 0.075, 0.1, 0.125, 0.15, 0.175, 0.2, 0.225, 0.25, 0.275, 0.3). The structural optimization was performed with both methods, all-electron (LAPW) and pseudopotentials (MBPP), and in both cases with the LDA and GGA xc-functionals.

4.3   Structural properties

In Fig. 4.3 we show the evolution of the calculated structural parameters a_0 and c_0 as a function of the Al and C-content in the alloys. On one hand, for the Al-doped system, we observe a decrease of the c_0 lattice parameter, which is related to the interplanar distance, and a nearly constant behavior of the a_0 lattice parameter. which is related with the atom-atom distance in the same plane. On the another hand, for the C-doped system, the behavior for these quantities is reversed, with c_0 being nearly constant and a_0 showing a decreasing behavior. This is a very interesting result keeping in mind that both systems are electron-doped, indicating that the doping site is important for determining the characteristics of these systems.
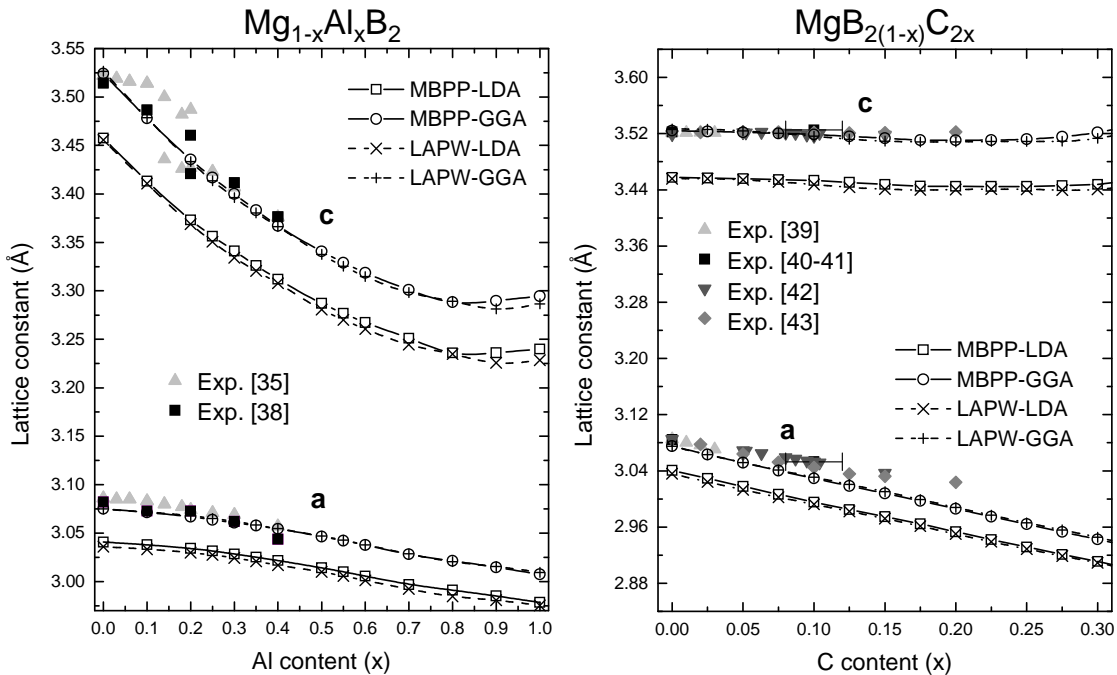

Figure 4.3: Evolution of the a_0 and c_0 lattice parameters for $\mathrm{Mg}_{1-x}\mathrm{Al}_x\mathrm{B}_2$ and $\mathrm{MgB}_{2(1-x)}\mathrm{C}_{2x}$ as a function of x and comparison with experimental results [35, 38–43].

The reason for this contrasting behavior of the lattice parameters is that for the

Al-doped system, the extra charge is located on the interplanar zone, and screens the repulsion between ions of different planes, giving as a result the reduction of c_0. Instead, the C-doped system shows the same effect but in the zone located between the B atoms of the same plane, since the extra charge coming from the C is located at the σ-bond and then a_0 decreases as the C-content increases. This behavior was understood due to a charge transfer analysis performed in a previous work [27, 180].

We also observe a good agreement between both methods, independently of the functional that we are using. This tells us so far that the VCA implementation on the MBPP-code works very well for the calculation of structural properties on these ternary alloys. Going further in the analysis, we see from the Fig. 4.3 that the GGA results are in better agreement with the experimental data than LDA, which is in accordance with several results in the literature where it is claimed that LDA underestimates the lattice parameters of metallic systems [72–77].
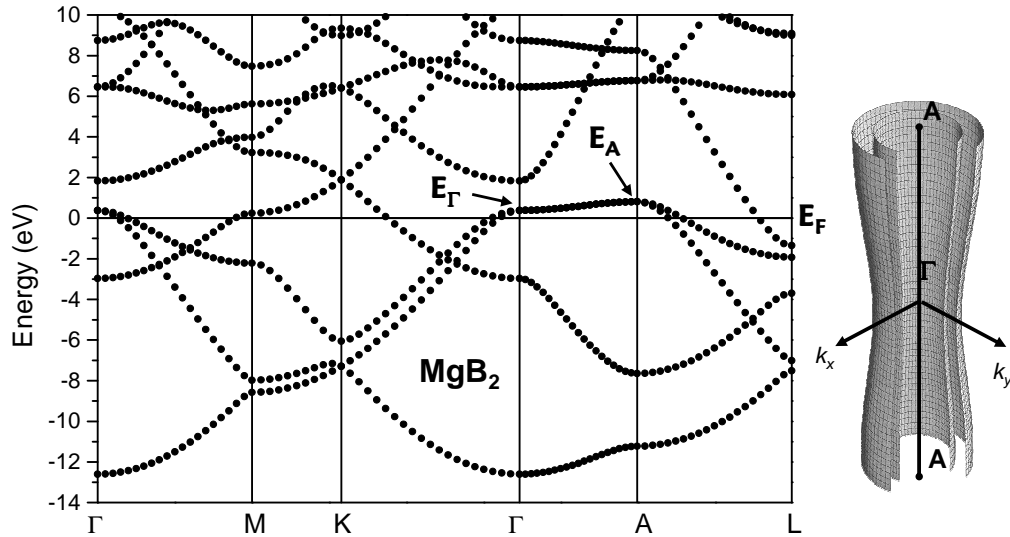
4.4 Electronic properties

Figure 4.4: Electronic band structure of MgB_2 and the σ-band Fermi surface at the $\Gamma - A$ path.

The electronic structure plays an important role in determining the superconducting properties of the materials. In the case of the MgB_2, the σ-band has special importance due to the strong e-ph coupling with the zone center E_{2g} phonon mode [123, 158, 159]. For that reason, we have studied the electronic properties of the $Mg_{1-x}Al_xB_2$ and $MgB_{2(1-x)}C_{2x}$ alloys, in particular the evolution of the electronic band structure. In Fig. 4.4 we show the MgB_2 electronic band structure and the Fermi surface associated to the σ-band at the $\Gamma - A$ path. In

general, we found that this band saturates as the content of Al or C in the alloy increases. This behavior is expected, since both systems are electron-doped, and one of the principal effects is the shift of the Fermi level to higher energies (band filling). Nevertheless, we find that the behavior of the σ-band is different between both cases, Al and C-doped.

In order to analyze the evolution of the σ-band, in Fig. 4.5 we show the behavior of the energy at the Γ point (E_Γ) and at the A point (E_A) (see Fig. 4.4) as a function of x for both systems. For $\mathrm{Mg}_{1-x}\mathrm{Al}_x\mathrm{B}_2$ we found that E_Γ goes to zero at $x = 0.26$, indicating an electronic topological transition (ETT) happening on the σ-band, since there is a transition from a continuous surface to a discontinuous one [27]. If we continue increasing the Al-content, we reach a second ETT, where $E_A = 0$ at $x = 0.57$, indicating total saturation of the σ-band and collapse of the corresponding Fermi surface. This critical concentration, $x_c = 0.57$, correlates with the loss of superconductivity on this alloy, experimentally determined at $x > 0.5$ (nominal content) [35–38]. The last result indicates that the loss of superconductivity in the $\mathrm{Mg}_{1-x}\mathrm{Al}_x\mathrm{B}_2$ alloy is related to the filling of the σ-band [27, 181].
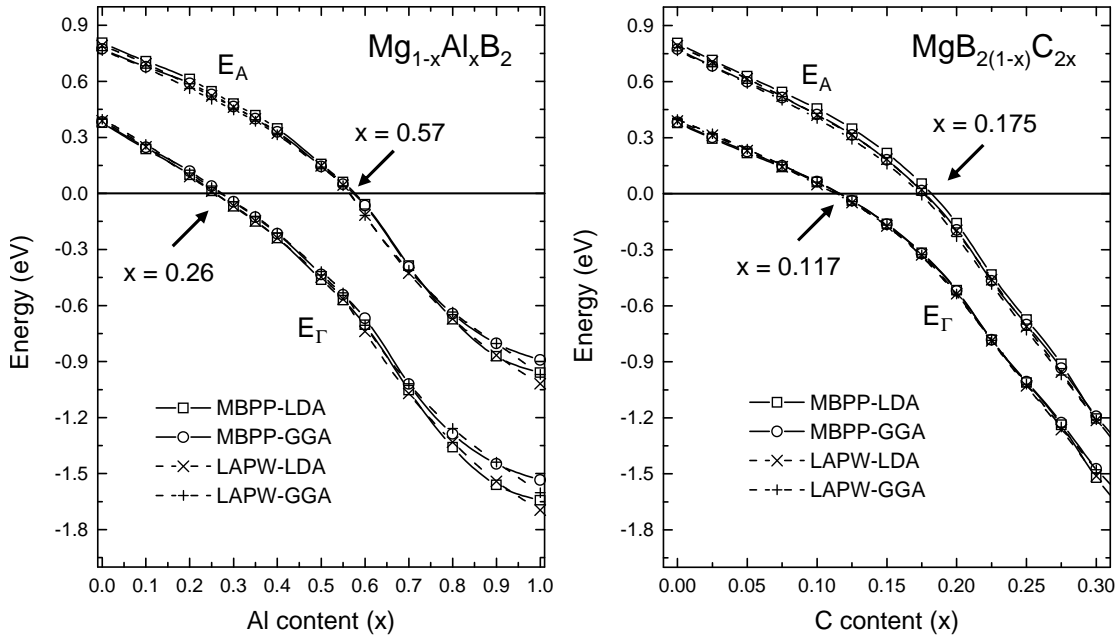

Figure 4.5: Evolution of E_Γ and E_A as a function of x for $\mathrm{Mg}_{1-x}\mathrm{Al}_x\mathrm{B}_2$ and $\mathrm{MgB}_{2(1-x)}\mathrm{C}_{2x}$ alloys obtained with both methods, LAPW and MBPP, and with both functionals, LDA and GGA.

We also studied the evolution of the σ-band in the $\mathrm{MgB}_{2(1-x)}\mathrm{C}_{2x}$ system, getting the following critical values for the ETT: $E_\Gamma = 0$ at $x = 0.117$ and $E_A = 0$ at $x = 0.175$. These values are clearly different from the Al-case, with the effect of C-doping being stronger than the Al-doping, although both of them are in prin-

ciple electron-doping systems. Note that the x values are not directly equivalent between both systems, since this x value is the number of extra electrons per atom in each alloy. If we want to make them equivalent (extra electrons per cell), then we just need to take the double of electrons for the C-doped system. With this in mind, the σ-band saturates at $x = 0.57$ in the Al-doped system and at $x = 0.35$ in the C-doped system, per unit cell, clearly a different result to the expected from the rigid band approximation, where the two systems must give the same critical concentration, since under this approximation they are indistinguishable. For $MgB_{2(1-x)}C_{2x}$ the experimental value of x_c, the critical concentration where $T_c \to 0K$ has not been reported, since there are segregation problems on this alloy at higher C-concentrations ($x > 0.13$). However, from the experimental data, it is observed a loss of superconductivity for $x \geq 0.15$ [39, 40, 42, 43], which is in agreement with our predicted value of $x_c = 0.175$.

Finally, the results have been calculated with both methodologies (LAPW and MBPP) and with both functionals (LDA and GGA), obtaining very good agreement between the two methods and only very small difference between functionals. Moreover, the results indicate the reliable description of electronic properties by the VCA implemented in the MBPP.

4.5 Vibrational properties
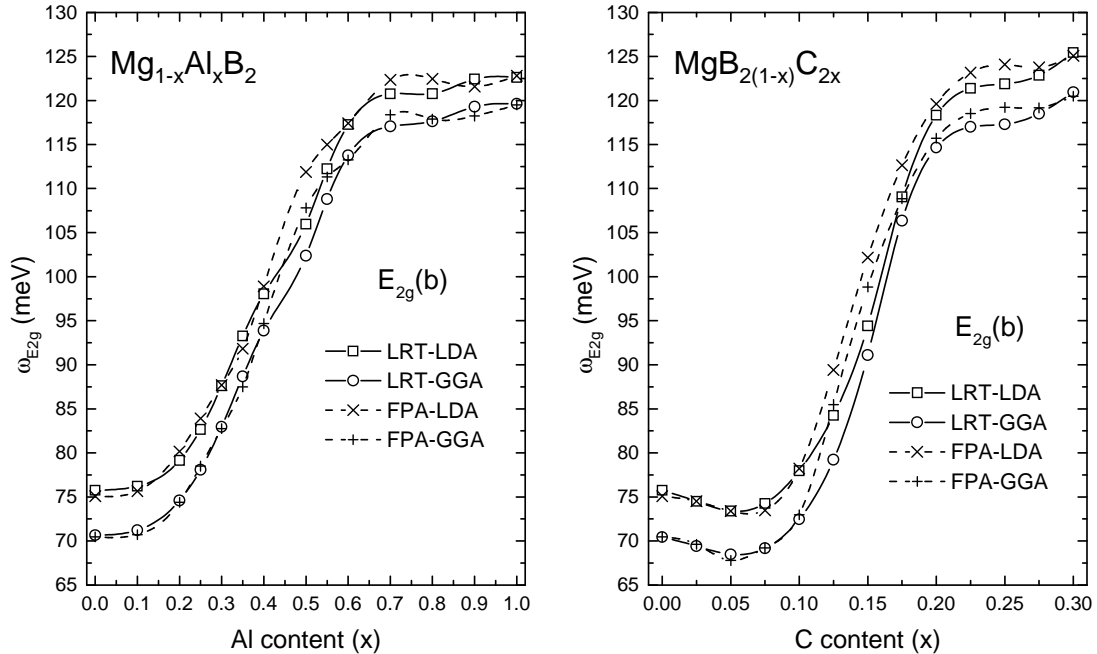

Figure 4.6: Evolution of $E_{2g}(b)$ phonon mode frequency as a function of x for $Mg_{1-x}Al_xB_2$ and $MgB_{2(1-x)}C_{2x}$ alloys. LRT calculations correspond to the MBPP code and FPA calculations correspond to the LAPW code.

In this section we present the results of the vibrational properties of the Al and C-doped $\mathrm{MgB_2}$ alloys, in particular, the evolution of the E_{2g}-phonon mode frequency and the full-phonon dispersion as a function of x. We start analyzing the evolution of the E_{2g}-phonon mode calculated with the frozen phonon approximation (FPA) implemented in the full potential code (LAPW) and the linear response theory (LRT) implemented in the pseudopotential code (MBPP). The two sets of calculations were performed using both xc-functionals, LDA and GGA.

In Fig. 4.6 we show the evolution of the E_{2g}-phonon mode frequency as a function of x for the $\mathrm{Mg_{1-x}Al_xB_2}$ and $\mathrm{MgB_{2(1-x)}C_{2x}}$ alloys. First we note that the results obtained with the two methods are in agreement, independently of the xc-functional (LDA or GGA). This gives us confidence that the VCA implementation is performing very well on zone center, high-symmetry modes, like the E_{2g}. In general, we observe that both alloys show a strong renormalization of the frequency as a function of x. This effect is stronger in the C-doped system, since the range of x where the transition takes place is narrower than in the Al-doped system. It is important to mention that this transition region (Fig. 4.6) correlates with the x region between the two ETT in the σ-band which were found before (Fig. 4.5) (Al: $0.26 \leq x \leq 0.57$; C: $0.117 \leq x \leq 0.175$), indicating the strong effect of the σ-band filling on the vibrational properties. We also note that in both systems, the LDA results are harder than GGA, a behavior that correlates with the smaller lattice parameters obtained with LDA (see section 4.1).
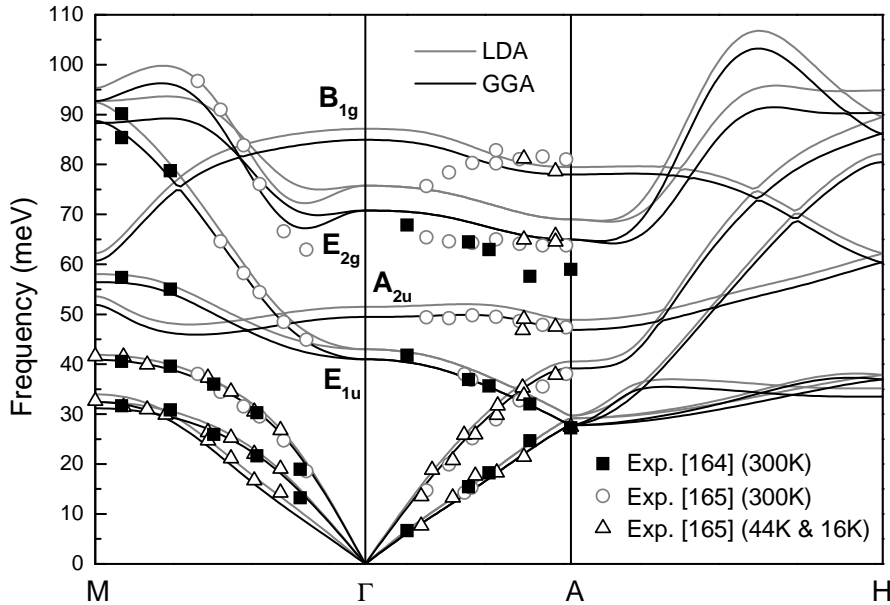

Figure 4.7: Full phonon dispersion of $\mathrm{MgB_2}$ in comparison with experimental results from Baron *et al.* [165] and Shukla *et al.* [164].

After we compared the VCA calculations of the phonon frequency for a specific mode on these alloys using the FPA-LAPW and LRT-MBPP methodologies.

We performed the calculation of the full-phonon dispersion for MgB_2 in order to compare with experimental results available in the literature [164, 165]. We observe that the calculations are in rather good agreement with the experimental data (see Fig. 4.7), with the GGA results (black line) being closer to experimental data than LDA (gray line). Thus, we can conclude that for MgB_2 the GGA describes better the full-phonon dispersion. Therefore, we continue the further analysis of the Al and C-doped systems with only the GGA xc-functional.
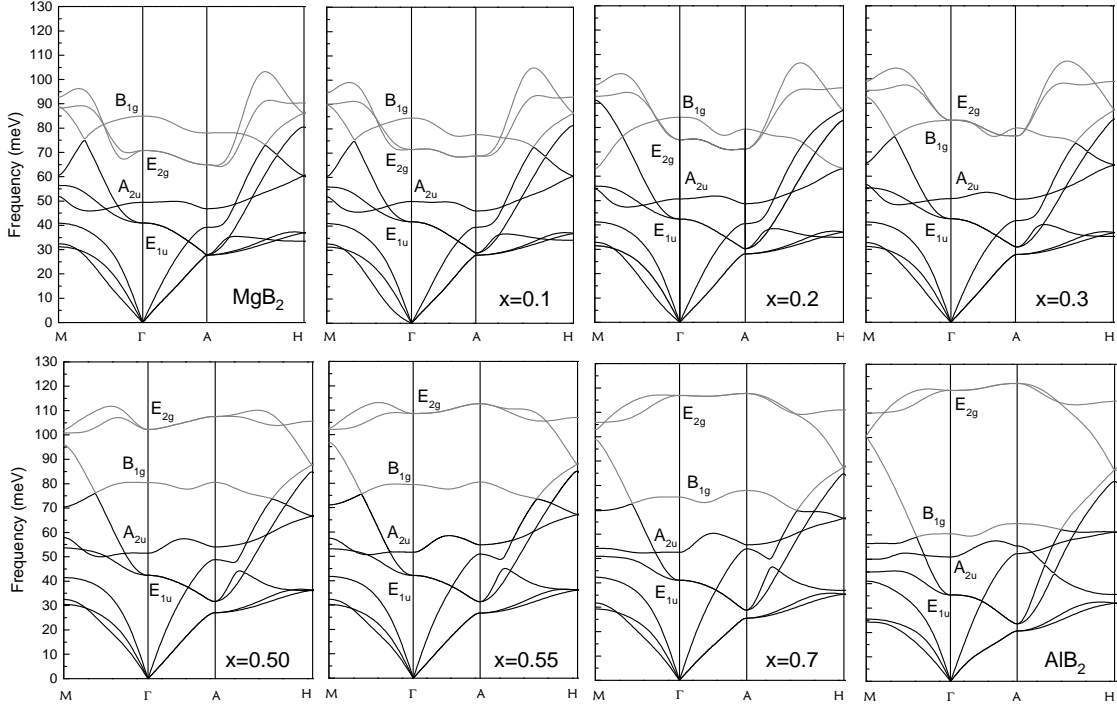

Figure 4.8: Full-phonon dispersion for $Mg_{1-x}Al_xB_2$ as a function of x. Gray color corresponds to the more affected branches by doping. Not showing $x = 0.25$ and $x = 0.90$ just for clarity.

For $Mg_{1-x}Al_xB_2$ we calculated the full-phonon dispersion curves for ten Al-concentrations (0.0, 0.1, 0.2, 0.25, 0.3, 0.5, 0.55, 0.7, 0.9, and 1.0) and also ten C-concentrations (0.0, 0.05, 0.075, 0.1, 0.125, 0.15, 0.175, 0.2, 0.25, and 0.3) for $MgB_{2(1-x)}C_{2x}$. The results for the Al-doped system are shown in Fig. 4.8 and for the C-doped system in Fig. 4.9. In both figures we marked with gray color the branches that are strongly affected by the Al and C-doping. Analyzing first the Al-doped system, we observe an interesting behavior of the spectra as a function of x, hardening of the E_{2g}-phonon mode and softening of the B_{1g}-phonon mode, which corresponds to an out-plane movement of the B-atoms [34]. The shift of these branches involves a strong reduction of dispersion of the branch corresponding E_{2g}-phonon mode, and the loss of dispersion is almost complete at $x = 0.55$, the same Al-concentration that corresponds to the saturation of the σ-band on the

electronic band structure (second ETT). At higher x, the branch keeps practically without any change, with just a small increase in frequency. On the another hand, the branch corresponding to the B_{1g}-mode continues shifting down until $x = 1.0$.

For the C-doped system the behavior of the full-phonon dispersion as x increases is similar to the Al-doped system, but taking place at smaller x. In this case there exists also a correlation between the loss of dispersion of the branch where the E_{2g}-mode corresponds, with the saturation of the σ-band ($x \approx 0.175$). However, the behavior of the B_{1g}-mode branch is slightly different, since in the C-doped system it is less affected than in the Al-doped system, being nearly constant with increasing C-content in the alloy. The loss of dispersion effect along the $M - \Gamma - A - H$ directions has a close relationship with the saturation of the σ-band from the electronic band structure. This is because the σ-states provide the background media in MgB_2 to slow down the E_{2g} frequency. When the σ-states (holes) decrease due to Al or C-doping (electrons), the background density starts to disappear and, then, the E_{2g}-mode rises in frequency.
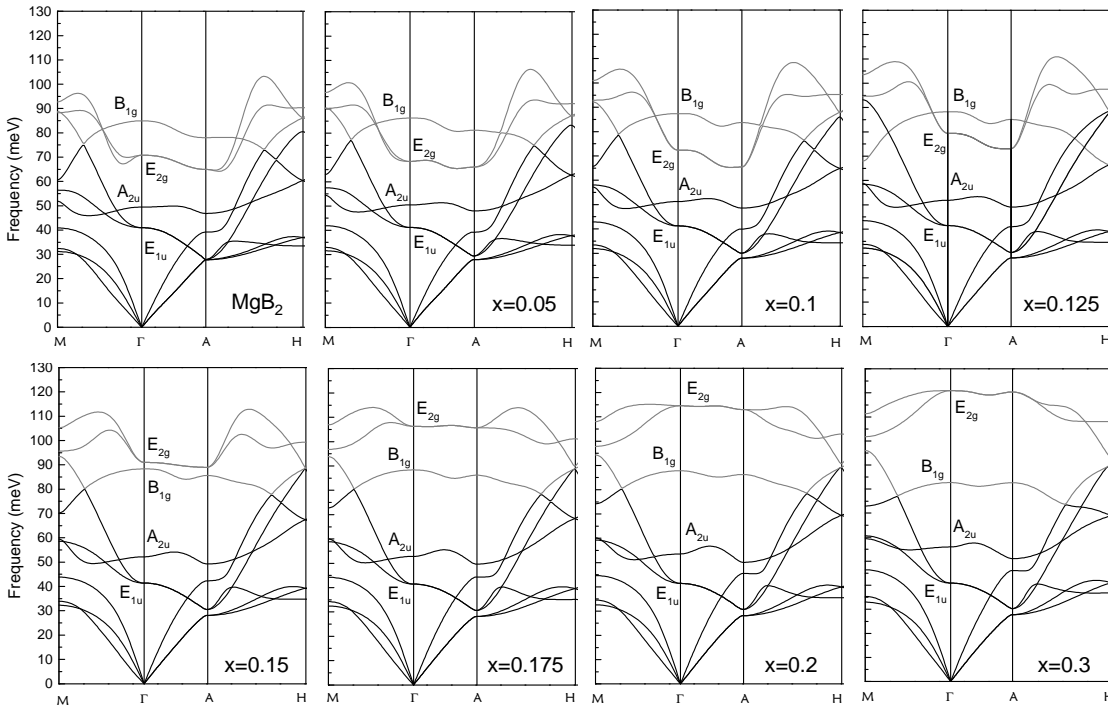
Figure 4.9: Full phonon dispersion for $MgB_{2(1-x)}C_{2x}$ as a function of x. Gray color corresponds to the more affected branches by doping. Not showing $x = 0.075$ and $x = 0.25$ just for clarity.

With the previously obtained information (electronic and vibrational properties), and using linear response theory it is possible to calculate the electron-phonon coupling and Eliashberg functions of the alloys from first-principles. This is exposed in the following section.

4.6   Superconducting properties

For the study of the superconducting properties, we have calculated the spectral or Eliashberg function, $\alpha^2 F(\omega)$, for each case, and from there, we are able to obtain the electron-phonon coupling constant, λ. Because the alloys based on MgB_2 are described by the two gaps model, we need to obtain these quantities for each band contribution, i.e. $\alpha_{ij}^2 F(\omega)$ and λ_{ij} with $i, j = \sigma, \pi$. Note that three of these four quantities are independent: $\sigma\sigma$, $\pi\pi$ (intraband contributions) and $\sigma\pi$ or $\pi\sigma$ (interband contribution).
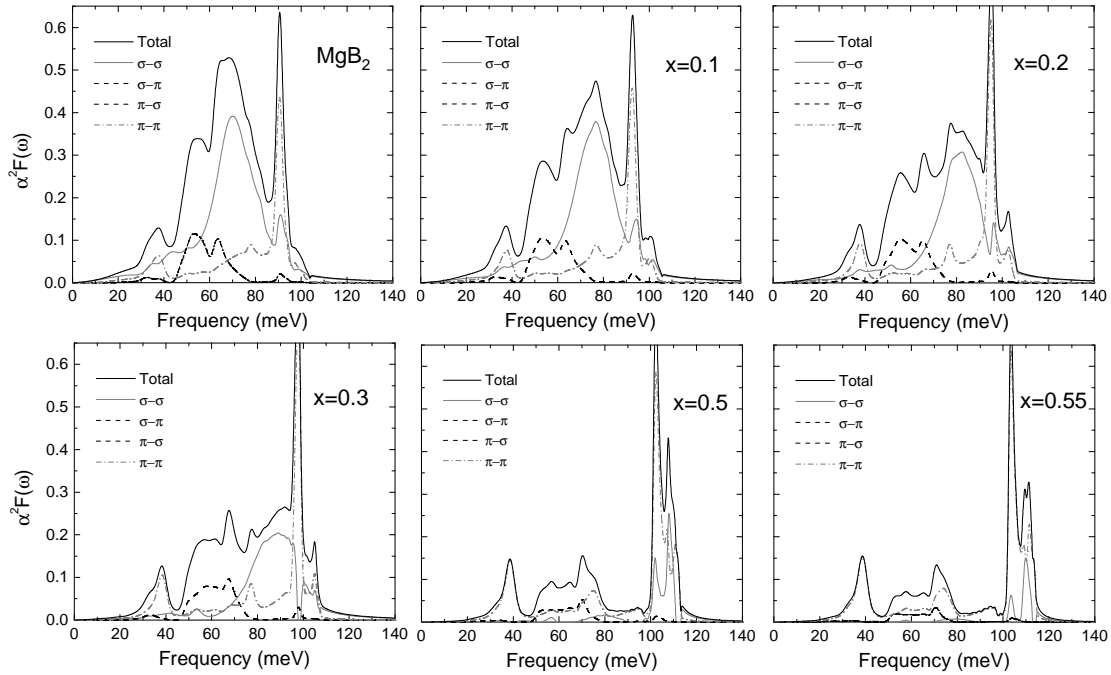

Figure 4.10: Evolution of the total and the components of the Eliashberg spectral function $\alpha_{ij}^2 F(\omega)$ with $ij = \sigma\sigma, \sigma\pi, \pi\sigma, \pi\pi$, for the $Mg_{1-x}Al_x B_2$ alloy.

In Fig. 4.10 we show the evolution of the total and the four components of the Eliashberg spectral function $\alpha_{ij}^2 F(\omega)$ ($ij = \sigma\sigma, \sigma\pi, \pi\sigma, \pi\pi$) of the $Mg_{1-x}Al_x B_2$ alloy for six Al-concentrations (0.0, 0.1, 0.2, 0.30, 0.5, and 0.55). This range of Al-concentrations represents the superconducting region for the alloy. For MgB_2 ($x = 0$), we can see that the main contribution to the total spectral function comes from the $\sigma\sigma$ spectra, with the main peak centered at approximately 70 meV, a value that corresponds to the E_{2g}-phonon mode frequency. Nevertheless, although the $\sigma\sigma$ spectra represents the main part of the total spectra, the other components also contribute to the total $\alpha^2 F(\omega)$. For example, the $\pi\pi$ spectrum is closely related to the high-frequency region of the phonons, mainly the B_{1g}-phonon mode, and the $\sigma\pi(\pi\sigma)$ spectra to the low-frequency region, between 40 and 70 meV. Thus, the present results indicate that in order to fully understand these systems,

we must consider the other contributions to $\alpha^2F(\omega)$, instead of considering it as a single band system (in that case, $\sigma\sigma$). From the evolution of the different contributions to $\alpha^2F(\omega)$ for $Mg_{1-x}Al_xB_2$ (see Fig. 4.10), we can observe how strongly $\alpha^2_{\sigma\sigma}F(\omega)$ is affected by the increase of Al-content. The main effects on this component of the spectra are the shift to higher frequencies and the reduction of its area at the same time, until $x = 0.55$, where the contribution is practically zero and the system is not superconducting [27,37,38]. That reduction indicates a loss of electron-phonon coupling between the $\sigma\sigma$ states and the bond-stretching phonon modes at the corresponding frequency. The interband contribution, $\sigma\pi$, follows closely the behavior of $\sigma\sigma$, showing a reduction as a function of x and almost disappears for $x = 0.55$. Nevertheless, the $\pi\pi$ contribution at higher frequencies is becoming stronger and the position of its main peak is practically unaffected by doping. This behavior is resulting from the hardening of the E_{2g}-phonon mode that we already discussed in the previous section.
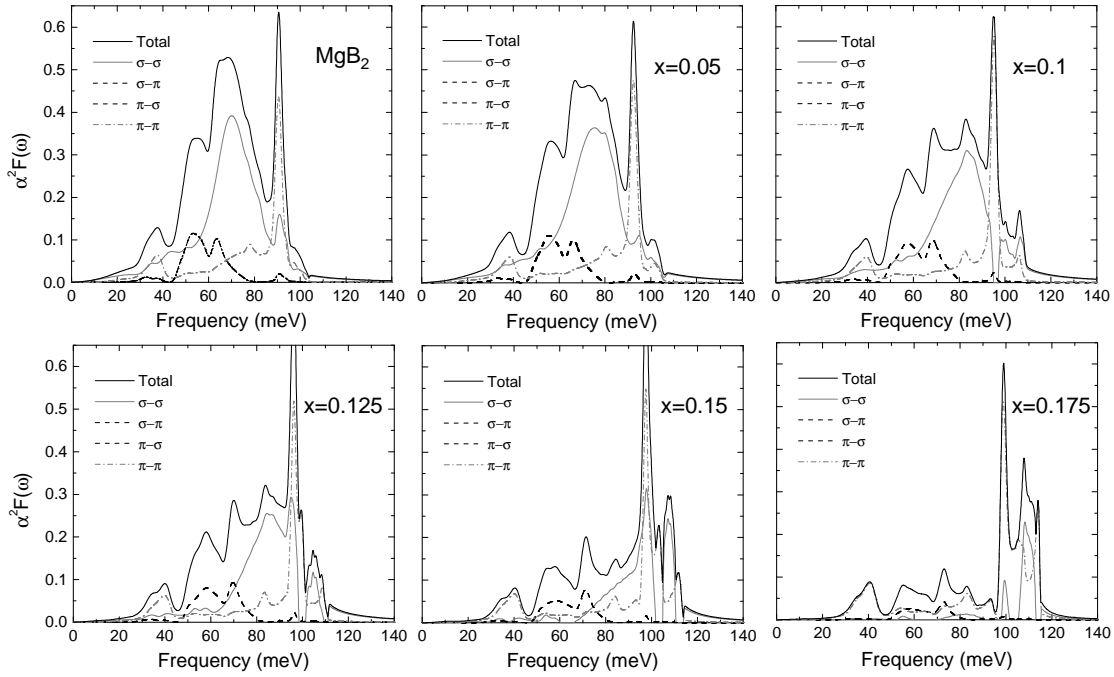
Figure 4.11: Evolution of the total and the components of the Eliashberg spectral function $\alpha^2_{ij}F(\omega)$ with $ij = \sigma\sigma, \sigma\pi, \pi\sigma, \pi\pi$, for the $MgB_{2(1-x)}C_{2x}$ alloy.

In Fig. 4.11 we show the results for the $MgB_{2(1-x)}C_{2x}$ alloy for six C-concentrations: (0.0, 0.05, 0.1, 0.125, 0.15, and 0.175). Performing the same analysis as for the Al-doped system we find that the evolution of the different contributions to $\alpha^2F(\omega)$ in C-doped MgB_2 is quite similar to the Al-doped system. That is, a strong decrease of the $\sigma\sigma$ and $\sigma\pi$ contributions with an increase of the $\pi\pi$ spectra due to basically the hardening of the E_{2g}-phonon frequency. The loss of $\alpha^2_{\sigma\sigma}F(\omega)$ at $x \approx 0.175$ correlates with the occurrence of the second ETT at the σ-band in

the electronic band structure (loss of the Fermi surface) of $MgB_{2(1-x)}C_{2x}$.

From the results of $\alpha_{ij}^2 F(\omega)$ we have obtained the e-ph coupling parameter, λ for each contribution ($\lambda_{\sigma\sigma}$, $\lambda_{\sigma\pi}$, $\lambda_{\pi\sigma}$, and $\lambda_{\pi\pi}$). In Fig. 4.12 they are shown the calculated values for the total and partial contributions of λ and $N(E_F)$ for the two alloys $Mg_{1-x}Al_xB_2$ and $MgB_{2(1-x)}C_{2x}$. The calculated values for MgB_2 are $\lambda_{\sigma\sigma} = 0.850$, $\lambda_{\sigma\pi} = 0.196$, $\lambda_{\pi\sigma} = 0.145$, $\lambda_{\pi\pi} = 0.250$, and $\lambda_{tot} = 0.672$, where each contribution λ_{ij} is normalized by the corresponding N_i and $\lambda_{tot} = (\sum \lambda_{ij} N_i)/N_{tot}$. The obtained value for λ_{tot} is very close to the experimental one by Geerk *et al.* [153] ($\lambda_{tot} = 0.650$). The partial contributions to $N(E_F)$ for MgB_2 are $N_\sigma = 0.148$ states eV^{-1}/spin and $N_\pi = 0.200$ states eV^{-1}/spin. These values are very similar to those calculated earlier by Liu *et al.* [63] and Golubov *et al.* [64].
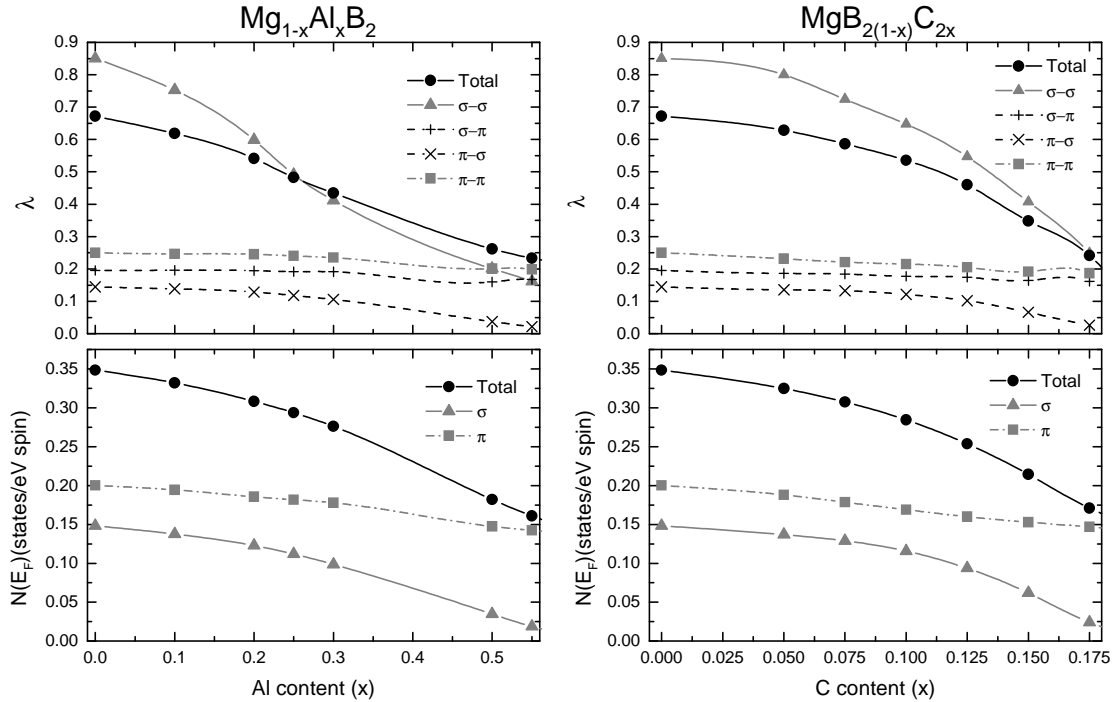
Figure 4.12: Evolution of λ_{ij} and $N_i(E_F)$ as a function of x for the $Mg_{1-x}Al_xB_2$ and $MgB_{2(1-x)}C_{2x}$. The calculated values for MgB_2 are: $N_\sigma = 0.148$ states eV^{-1}/spin, $N_\pi = 0.200$ states eV^{-1}/spin, $\lambda_{\sigma\sigma} = 0.850$, $\lambda_{\sigma\pi} = 0.196$, $\lambda_{\pi\sigma} = 0.145$, $\lambda_{\pi\pi} = 0.250$, and $\lambda_{tot} = 0.672$.

From the Fig. 4.12, we can clearly see that the main contribution to the e-ph coupling in MgB_2 ($x = 0$) is coming from the $\sigma\sigma$ component. Nevertheless, the other contributions, $\pi\pi$ and interband ($\sigma\pi$, $\pi\sigma$), are not so small to neglect them. Following the evolution of the different components of the e-ph coupling parameter as a function of x in both alloys, we observe that λ_{tot} decreases as a function of x, mainly by the effect of the reduction in $\lambda_{\sigma\sigma}$. In contrast, $\lambda_{\sigma\pi}$, $\lambda_{\pi\sigma}$ and $\lambda_{\pi\pi}$ are almost unaffected by doping. Comparing λ and $N(E_F)$ we notice that the e-ph coupling parameters follow the same behavior as the σ contribution

to the density of states (N_σ). This result indicates again the great importance of the σ-band states to the electron-phonon properties in both alloys. However, the $\pi\pi$, $\sigma\pi$, and $\pi\sigma$ contributions can not be neglected, because considering only the $\sigma\sigma$ contribution produces a value of λ_{tot} of ≈ 0.85, which is larger than the experimental value. These effects have been already discussed in the literature [63, 64, 158, 159].
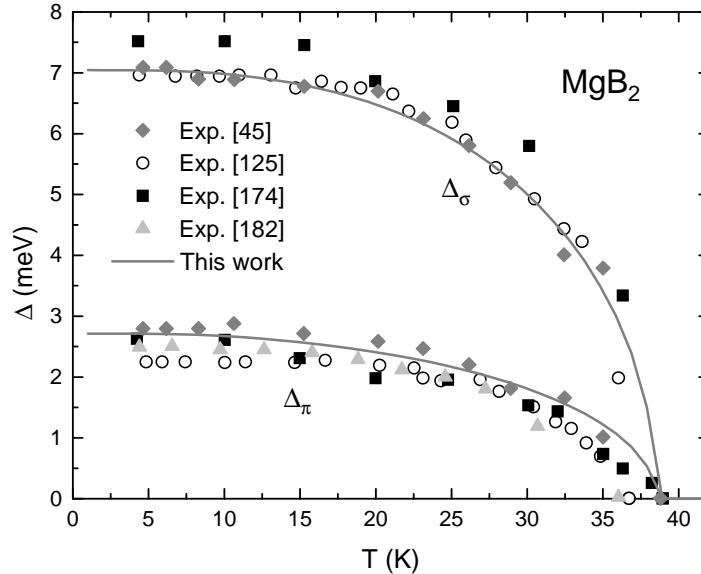

Figure 4.13: Temperature dependences of the superconducting gaps Δ_σ and Δ_π for the solution of the two-band Eliashberg gap equations and comparison with experimental data [45, 125, 174, 182]. The calculated values of the gaps at $T = 0$ K were $\Delta_\sigma = 7.04$ meV and $\Delta_\pi = 2.71$ meV.

In the case of a single-band superconductor, from the knowledge of $\alpha^2 F(\omega)$ and a value of the Coulomb pseudopotential $\mu^*(\omega_c)$, we are able to solve the Eliashberg gap equations on the imaginary frequency axis, i.e. the Matsubara frequencies (see section 2.5 and references therein) in order to obtain the superconductor gap as a function of T. However, in the cases of Al- and C-doped MgB_2 we must apply the Eliashberg gap equations in the two band model since we are dealing with two distinctive contributions (σ and π) to the gaps. Therefore, we used the $\alpha^2_{ij} F(\omega)$ ($ij = \sigma\sigma, \sigma\pi, \pi\sigma,$ and $\pi\pi$) with a proposed diagonal form for the $\mu^*(\omega_c)$ matrix. We solved the gap equations in the two band model for MgB_2. In order to reproduce the experimental value of $T_c = 38.82$ K [45, 48], we used the standard expression of the cutoff frequency, $\omega_c = 10\omega_{ph}^{max}$ and the following values for the $\mu^*(\omega_c)$ matrix elements: $\mu^*_{\sigma\sigma} = \mu^*_{\pi\pi} = 0.107$ and $\mu^*_{\sigma\pi} = \mu^*_{\pi\sigma} = 0$. The resulting temperature dependences of the superconducting gaps are shown and compared with experimental data [45, 125, 174, 182] in Fig. 4.13. The gap values obtained for MgB_2 at $T = 0$ K are $\Delta_\sigma = 7.04$ meV and $\Delta_\pi = 2.71$ meV, which are in good agreement with experimental results [45, 125, 182]. It is important to mention at

this point that the $\mu^*(\omega_c)$ values are the only non *ab-initio* parameters used in the whole series of calculations in the present study.

For the $Mg_{1-x}Al_xB_2$ and $MgB_{2(1-x)}C_{2x}$ alloys we also solved the Eliashberg gap equations in the two-band model (we obtained the T dependence of Δ_σ and Δ_π). In the alloys we applied two different schemes for the scaling of $\mu^*(\omega_c)$ with the alloy concentration. The first one was just keeping constant the matrix element values with respect to MgB_2. The second one was applying the representation $\mu^*(x) = U_c N(E_F, x)$ proposed by Gladstone *et al.* [156] for the scaling of μ^* as a function of x. For the second scheme we combined the U_c value obtained for MgB_2 from $U_c = \mu^*(0)/N(E_F, 0) = 0.154$, with the calculated values for $N(E_F, x)$(states eV^{-1}/cell). From these results, the values of the superconducting gaps and T_c are calculated.
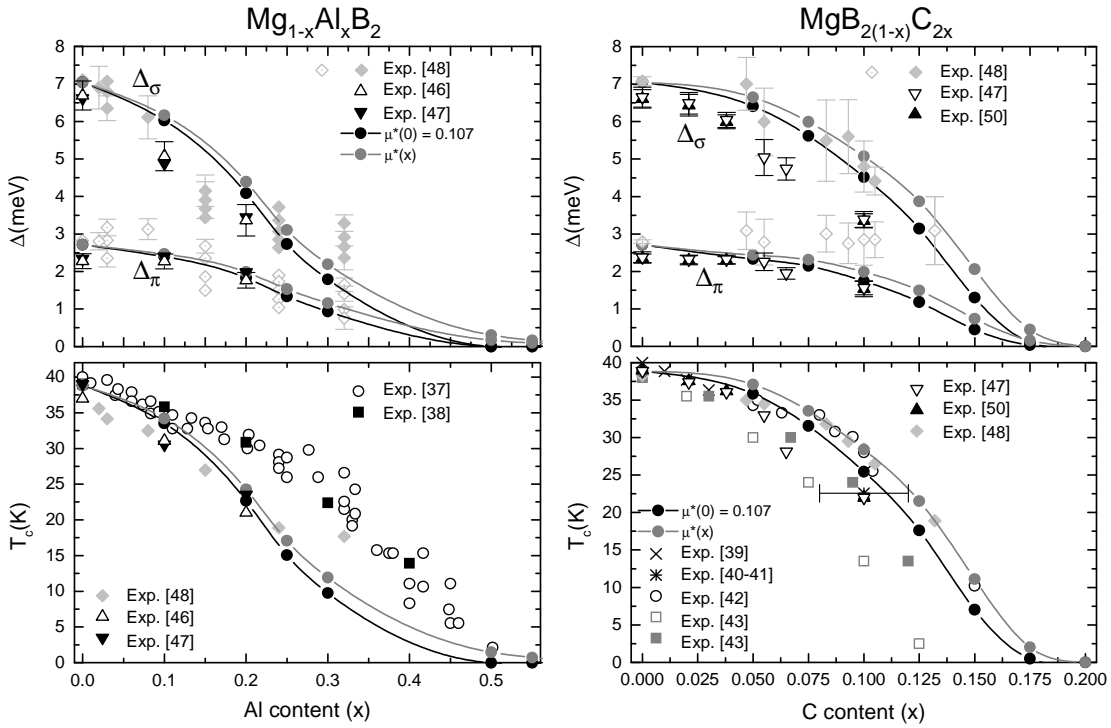
Figure 4.14: Superconducting gaps, $\Delta_\sigma(x)$ and $\Delta_\pi(x)$, and critical temperature, $T_c(x)$, for $Mg_{1-x}Al_xB_2$ and $MgB_{2(1-x)}C_{2x}$. The lines with circles are the calculated values and the symbols represent the experimental measurements [37–43, 46–48, 50].

The evolution of Δ_σ, Δ_π, and T_c as a function of x for the Al- and C-doped systems are presented in Fig. 4.14 and compared with experimental data [37–43, 46–48, 50]. Values of the superconducting gaps and λ_{ij} as function of x had been obtained previously from empirical calculations fitted to the MgB_2 experimental data and scaled with $N(E_F)$ in order to get the evolution with x [181, 183]. Then, we do not include that results in the discussion of this work since they only represent a qualitative description of the experimental data [44]. We find that the

calculations reproduce the experimental trends, that is, the decrease of the gaps and T_c as a function of x with both approaches for μ^*, although the difference between the two schemes for μ^* is small at a given x and both are quite close to the experimental data. The point to be considered is that the scaled scheme predicts the loss of superconductivity at $x \approx x_c$, being x_c the Al- and C-concentration where the ETT happens for each system ($x_c(\mathrm{Al}) = 0.57$, $x_c(\mathrm{C}) = 0.177$). Instead, the constant approach predicts that T_c goes to zero at slightly lower concentrations. The differences on the evolution of gaps and T_c between the Al- and C-doped systems are more interesting. The Al-doped system shows an inflection point in $T_c(x)$ at $x \approx 0.25$, in contrast to the C-doped system which shows a monotonic behavior of the slope. These differences indicate how important is the doped site on $\mathrm{MgB_2}$ alloys, and also that although both are electron-doped cases, their effects on the superconducting gaps and critical temperature are quite different.

In Fig. 4.14 we observe a clear dispersion of different experimental sets of data. This indicates how sensitive are the superconducting properties to the sample preparation methods and physical conditions of the procedure itself. Additionally, for these alloys it is complicated to determine accurately the real concentration in each case. Those could be some sources for the observed experimental differences. Despite of this, the calculated $T_c(x)$ follows nicely the data for lower and intermediate range of Al-content. The calculations for the gaps are also in very good agreement with the experimental data, in particular Δ_π.

In the case of the C-doped $\mathrm{MgB_2}$ system, the tendencies for Δ_σ, Δ_π and $T_c(x)$ are similar to the Al-doped case, but given the lower x, the effects of doping are stronger (gaps and T_c go to zero faster than in the Al-doped system). The comparison with experiments is very good for both gaps and T_c, as a function of x specially if takes in to account discrepancies between different experimental results, in particular for the superconducting gaps. For $T_c(x)$, despite of the differences between different experimental sets of data, all are approximately included in the error bar given by Ribeiro *et al.* [40] and Avdeev *et al.* [41]. Other experiments used these data set as benchmarks. Nevertheless, we observe the good agreement of the calculated $T_c(x)$ with practically all the experiments at $x \leq 0.05$. For higher x, the good agreement is obtained with the data sets of Kazakov *et al.* [42] and Gonnelli *et al.* [48].

In Fig. 4.15 we show the calculations and experimental data of Δ_σ and Δ_π for Al and C-doped systems [45–48, 50, 51] as a function of the critical temperature. From the theoretical point of view, we can see that both schemes for μ^* give practically the same results for the σ- and π-gaps. The advantage of plotting the values of the gaps vs. T_c as in Fig. 4.15 is that in this way it is eliminated any possible source of discrepancy concerning the concentration of the alloys in the experimental data. From the experimental data we observe a decrease of the
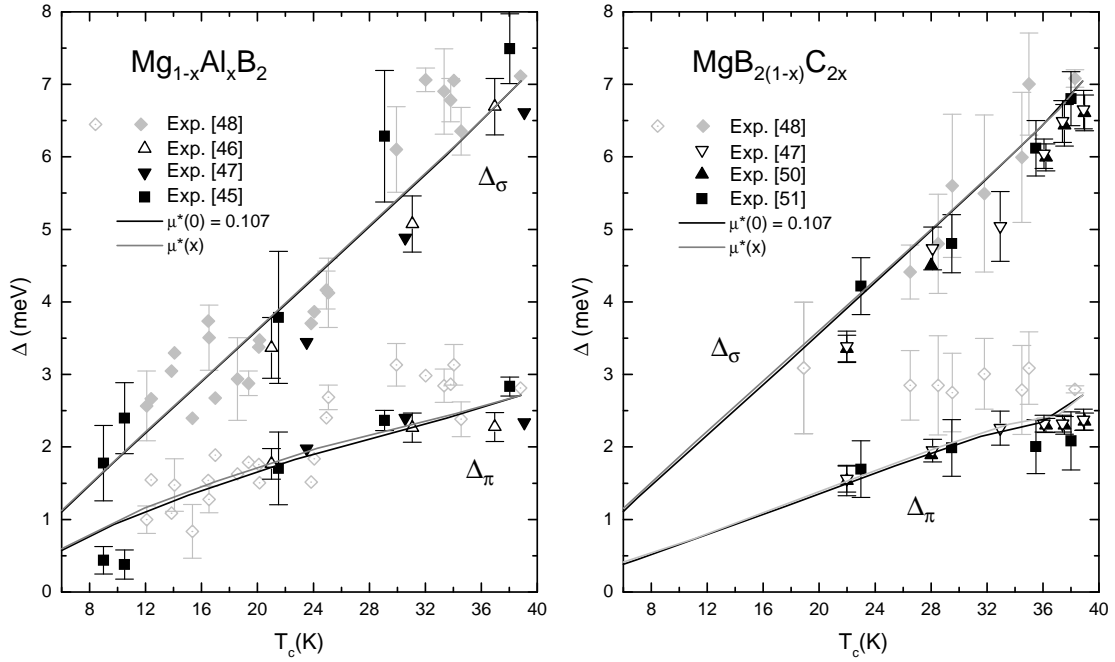
Figure 4.15: Superconducting gaps (Δ_σ and Δ_π) for Al- and C-doped MgB_2 as a function of critical temperature T_c, obtained from the solution of the Eliashberg gap equations without interband scattering (lines) compared with experimental results [45–48, 50, 51].

gaps as T_c decreases for both systems, but for the case of C-doped, there is a set of data that reports a merge of the superconducting gaps at $T_c \approx 19$ K [48], in clear disagreement with the other experimental reports [47, 50, 51]. So far there is not a consensus about the merging (or not) of the superconducting gaps in the C-doped system. Nevertheless, in both cases we can say that the agreement of the calculations with the experiments is quite good. Based on the agreement with the calculations with most of the available experimental data one may conclude that there is no clear evidence for a merging of the gaps for any of both Al- and C- doped MgB_2 systems. Therefore, the interband scattering in Al- and C-doped samples, if present, is small and their effects are negligible on the superconducting properties of $Mg_{1-x}Al_xB_2$ and $MgB_{2(1-x)}C_{2x}$.

Conclusions

- We find that the self-consistent virtual crystal approximation implemented in the mixed basis pseudopotential code reproduce the all-electron LAPW calculations of the structural, electronic, and vibrational properties for the $Nb_{1-x}Mo_x$ binary alloys and the $Mg_{1-x}Al_xB_2$ and $MgB_{2(1-x)}C_{2x}$ ternary alloys.

- For the $Nb_{1-x}Mo_x$ alloy, an electronic topological transition (ETT) was found at $x_c \approx 0.3$, where the Fermi surface at the Γ point corresponding to hole character in Nb disappears and a Fermi surface with electron character emerges.

- The experimentally observed non-monotonic behavior of the phonon frequencies at the H and N points, and the evolution of phonon anomalies in the $Nb_{1-x}Mo_x$ alloy with the Mo-concentration are reproduced by the VCA calculations.

- We find that the GGA calculations for the phonon frequencies of the H and N modes specifically in $Nb_{1-x}Mo_x$ are in better agreement with experimental data than the corresponding LDA calculations. However, LDA and GGA possess similar accuracy in describing the experimental full phonon dispersions, although with LDA typically harder spectra are obtained.

- The Eliashberg function $\alpha^2F(\omega)$ for $Nb_{1-x}Mo_x$ shifts to higher frequencies as the Mo-content increases. The total weight of $\alpha^2F(\omega)$ and the corresponding coupling constant $\lambda(x)$ exhibit a non-monotonic behavior with a strong reduction at smaller x, a minimum at $x \approx 0.7$ and increasing slightly toward $x = 1$ (Mo).

- When the $\mu^*(x)$ is scaled with $N(E_F, x)$, the calculated $T_c(x)$ for $Nb_{1-x}Mo_x$ reproduces the experimental data in the whole range of Mo-concentrations.

- We find two electronic topological transitions at the Fermi surface corresponding to the σ-band in the $Mg_{1-x}Al_xB_2$ and $MgB_{2(1-x)}C_{2x}$ alloys. The

first critical concentration $x_1(\text{Al/C}) = 0.26/0.117$ corresponds to a disruption of the tubular structure at the Γ point and the second critical concentration $x_2(\text{Al/C}) = 0.57/0.175$ corresponds to the saturation of the σ-band.

- The calculated full-phonon bands for MgB_2 are in good agreement with the experimental data available in the literature. Moreover, the GGA results are in better agreement with the experiments than LDA.

- The frequency of the E_{2g}-phonon mode in $\text{Mg}_{1-x}\text{Al}_x\text{B}_2$ and $\text{MgB}_{2(1-x)}\text{C}_{2x}$ shows a strong renormalization (hardening) in a very well defined range of Al and C concentrations (x). This transition region correlates with the x range between the two electronic topological transitions in the σ-band, indicating the relevance of the electronic structure in determining the vibrational properties of these alloys.

- The E_{2g} phonon branch exhibits a loss of dispersion around the critical concentration where the σ-band is saturated for the two studied alloys, $\text{Mg}_{1-x}\text{Al}_x\text{B}_2$ and $\text{MgB}_{2(1-x)}\text{C}_{2x}$.

- For MgB_2, using the two gap model we have obtained $\lambda_{tot} = 0.67$, which is in very good agreement with the experimental value ($\lambda_{exp} = 0.65$) deduced from tunneling measurements.

- We reproduce the experimental behavior of $\Delta_{\sigma,\pi}$ and T_c on both alloy systems neglecting the interband scattering, $\Gamma_{\sigma\pi}$. However, a deeper understanding of the role of $\Gamma_{\sigma\pi}$ is needed, considering the current controversy about the gap merging in the $\text{MgB}_{2(1-x)}\text{C}_{2x}$ alloy.

Resumen de Tesis de Doctorado

Estudio de la interacción electrón-fonón en aleaciones intermetálicas superconductoras

Omar de la Peña Seaman

Directores de Tesis
Dr. Romeo de Coss
Dr. Klaus-Peter Bohnen

Introducción

Los efectos de la interacción electrón-fonón en materiales metálicos son evidentes en muchas cantidades físicas que pueden ser detectadas y medidas en experimentos. Solo por mencionar algunos, la interacción electrón-fonón contribuye a la resistividad eléctrica y térmica, genera el mejoramiento de la masa efectiva (la cual puede ser medida a través de la capacidad calorífica electrónica), además de que juega un rol muy importante en el fenómeno de la superconductividad. Centrándonos en este último, dentro del marco de la teoría de Eliashberg las propiedades superconductoras y en particular la temperatura crítica, T_c, dependen de sólo dos cantidades para poder ser calculadas, el potencial de repulsión Coulombico apantallado μ^* y la función espectral o de Eliashberg $\alpha^2 F(\omega)$ [1–4]. Esta cantidad representa básicamente la efectividad de que fonones de una determinada energía $\hbar\omega$ dispersen electrones de una región de la superficie de Fermi a otra. Es por ello que también se le conoce como la función de acomplamiento electrón-fonón. Esta función de acomplamiento puede ser obtenida via experimentos de tunelamiento construyendo uniones metal-aislante-superconductor [5]. Este método de obtener experimentalmente $\alpha^2 F(\omega)$ no es posible realizarlo en todos los casos, particularmente en aquellos en los cuales la construcción de las uniones es compleja y también en materiales donde el acomplamiento es tan débil que la extracción de información de la señal de tunelaje es complicado [5].

Es aquí donde el enfoque de la simulación computacional puede ser una her-

ramienta muy útil para estudiar y analizar materiales sobre los cuales existe limitada información experimental o es muy complicada de extraer. Los cálculos de primeros principios pueden proveer información valiosa acerca del acoplamiento electrón-fonón de un material en cuestión, para ello es necesario conocer diferentes propiedades del sistema, tal como el espectro electrónico, el mapa completo de dispersión fonónica, y el espectro de respuesta del sistema electrónico con respecto a las vibraciones de la red. Recientemente dentro del marco de la teoría del funcional de la densidad (DFT) [7, 8] la teoría de respuesta lineal (LRT), ha demostrado ser una poderosa herramienta para el cálculo de propiedades dinámicas [9] y de acoplamiento electrón-fonón [10] en materiales. Se han realizado cálculos en materiales superconductores para los cuales existen una gran cantidad de resultados experimentales, y se ha encontrado un muy buen acuerdo en las propiedades obtenidas, demostrando la efectividad de los métodos de primeros principios [11, 12].

Sin embargo, a pesar de los avances mencionados anteriormente, para el caso de las aleaciones no existe mucha información de las propiedades vibracionales ni del acoplamiento electrón-fonón, especialmente desde el punto de vista teórico. Por mencionar un ejemplo, tenemos a laaleación $Nb_{1-x}Mo_x$, un sistema ampliamente estudiado, el cual presenta un comportamiento no monótono en T_c y en el valor de la frecuencia en puntos de alta simetría en la zona de Brillouin como función de la concentración de Mo [13–18]. El origen de este comportamiento aún no esta completamente entendido a pesar de los esfuerzos que se han realizado para estudiar esta aleación. Esto se debe parcialmente a la falta de un método y computacional eficiente para estudiar aleaciones y la evolución de diferentes propiedades en función de la concentración en un amplio rango sin sacrificar información tal como la estructura cristalina o el grupo espacial, entre otras. Por ejemplo, la evolución de las propiedades electrónicas y elásticas de $Nb_{1-x}Mo_x$ en función de x han sido estudiadas usando diferentes aproximaciones tales como la aproximación de las estructuras cuasi-aleatorias (QRS) [19], la aproximación del potencial coherente (CPA) [20–22] y la aproximación del potencial coherente Korringa-Kohn-Rostoker (KKR-CPA) [23, 24]. Sin embargo, estos estudios han estado limitados a un número reducido de concentraciones, debido a que son difíciles de interpretar y computacionalmente costosos, especialmente si se esta interesado en las regiones de muy bajas (cerca del Nb) o muy altas concentraciones (cerca del Mo). Es por ello que esta aleación es un sistema ideal para probar la aplicabilidad de un enfoque distinto en cuanto a la modelación de aleaciones para el cálculo de propiedades vibracionales, acoplamiento electrón-fonón y superconductividad. En este trabajo utilizamos un nuevo enfoque conocido como la aproximación autoconsistente del cristal virtual (VCA) [25–29].

Otro sistema de interés, el cual ha sido ampliamente estudiado a pesar de que

su descubrimiento como material superconductor fue apenas en 2001, es el MgB_2 y las aleaciones relacionadas. El compuesto intermetálico MgB_2 posee una $T_c \approx 39$ K [30] y actualmente se ha establecido que se trata de un material superconductor BCS-Eliashberg, mediado por fonones con múltiples brechas superconductoras y un fuerte acoplamiento electrón-fonón (e-ph). El acoplamiento e-ph en este material se da principalmente entre la superficie de Fermi asociada a la banda σ, que proviene de los orbitales $p_x - p_y$ del boro, y fonón específico correspondiente al modo vibracional que comprime al enlace B-B con simetría E_{2g} en Γ [31–34]. Tan pronto como las propiedades superconductoras del MgB_2 se descubrieron, la comunidad científica comenzó la búsqueda de una posible familia de superconductores relacionados con este compuesto. Los primeros estudios en esta dirección fueron las aleaciones, es decir, la sustitución parcial de uno de los elementos constitutivos del material por otros similares, tal como Mg por Al y B por C, dando lugar a las aleaciones $Mg_{1-x}Al_xB_2$ [35–38] y $MgB_{2(1-x)}C_{2x}$ [39–43], respectivamente. Las propiedades vibracionales y superconductoras de las aleaciones, como son la frecuencia del modo E_{2g}, el acoplamiento e-ph y T_c, son influenciadas por la concentración del elemento aleante de varias maneras. Por ejemplo a través de los cambios en la estructura electrónica y la densidad de estados, los cuales tienen un efecto directo en las propiedades antes mencionadas. El incremento de x (Al o C) en ambas aleaciones produce un corrimiento en la frecuencia del modo E_{2g} hacia valores altos (conocido como renormalización), una reducción del acoplamineto e-ph, T_c y de las brechas superconductoras [35–51].

Objetivo

El objetivo de esta tesis es el estudio del acoplamiento electrón-fonón y las propiedades superconductoras de las aleaciones $Nb_{1-x}Mo_x$, $Mg_{1-x}Al_xB_2$, y $MgB_{2(1-x)}C_{2x}$ a través de cálculos de primeros principios, usando para este propósito la versión auto-consistente de la aproximación del cristal virtual como un enfoque diferente para la simulación de aleaciones superconductoras. En particular, analizar la evolución de las propiedades vibracionales y superconductoras como función de x, la aparición de transiciones topológicas electrónicas y los efectos de éstas en la renormalización fonónica, el acoplamiento electrón-fonón y la temperatura crítica superconductora.

Metodología

Para este estudio computacional, se usaron cálculos numéricos dentro del marco de la teoría del funcional de la densidad [7, 8] aplicando la aproximación VCA auto-consistente [25–29]. Realizamos el cálculo de las propiedades estructurales,

electrónicas y de las frecuencias fonónicas en algunos puntos de alta simetría en la zona de Brillouin. Utilizamos el método de ondas planas aumentadas y linealizadas (LAPW) [54–56], tal como está implementado en el código Wien2k [57]. La aproximación VCA dentro del método LAPW ha sido usada con éxito anteriormente en el estudio de otros sistemas [26–29]. Adicionalmente hemos investigado las mismas propiedades implementando la aproximación VCA auto-consistente en el método de pseudopotenciales con bases mezcladas (MBPP) [58]. Éste método incorpora la implementación de la teoría de respuesta lineal (LRT) [9, 32, 59–61] para el cálculo de propiedades de la dinámica de la red de una manera muy eficiente. Por lo tanto, las propiedades vibracionales así como también el acoplamiento electrón-fonón fueron obtenidos mediante el uso de LRT a través del método MBPP. Las propiedades superconductoras fueron analizadas y discutidas dentro del marco de la teoría de Eliashberg en los modelos de una y dos brechas superconductoras citesavra2,heid,liu,kong,golu. Para ambos métodos se han utilizado las aproximaciones LDA [70, 71] y GGA [81] para el potencial de intercambio y correlación (xc) con el objetivo de analizar los efectos de correlación de gradiente sobre las propiedades vibracionales y la interacción electrón-fonón.

Resultados

Encontramos muy buen acuerdo entre ambos métodos (LAPW y MBPP) en todas las propiedades calculadas para el sistema Nb-Mo , independientemente de la aproximación usada para el funcional de intercambio-correlación (xc), LDA o GGA. En particular, con respecto a las propiedades estructurales (parámetro de red a_0 y módulo de compresibilidad B_0), reproducimos la tendencia presentan los datos experimentales para a_0 y B_0 en función de x [14, 128, 129, 132, 148], encontrándose mejor acuerdo cuando expleamos GGA. La mayor diferencia encontrada entre los cálculos GGA y los datos experimentales para a_0 es de sólo 0.5% en $x = 1$ (Mo).

Para la aleación Nb-Mo identificamos una transición topológica electrónica (ETT) en la estructura de bandas en una concentración crítica (x_c) de $\approx 30\%$ de Mo. Esta transición ocurre en Γ, en donde la superficie de Fermi correspondiente a estados con carácter de huecos ($x < x_c$) desaparace y una superficie de Fermi con carácter de electrones ($x > x_c$) emerge. Este resultado representa la primera determinación precisa (dentro de las limitaciones de VCA) de x_c para esta ETT, la cual ha sido señalada como responsable de las anomalías observadas en las propiedades elásticas de esta aleación [129].

Respecto a las propiedades fonónicas, los cálculos reproducen la evolución no-monótona de la frecuencia en los puntos de alta simetría H, y N (N_1, N_3 y N_4) observada experimentalmente tanto con la aproximación del fonón-congelado imple-

mentado en el método LAPW como con la teoría de respuesta lineal implementada en el método MBPP. Ambos métodos (con ambos funcionales xc) dan un acuerdo similar con los datos experimentales [18], indicándonos que la implementación del VCA en MBPP es confiable para el cálculo de propiedades vibracionales. Una vez demostrada la confiabilidad de la implementación, se procedió al cálculo de la estructura de bandas fonónicas para determinadas concentraciones de la aleación. Encontramos que el espectro calculado con LDA da frecuencias mayores que el obtenido con GGA, ambos funcionales reproducen los datos experimentales con el mismo nivel de precisión, existiendo solo una pequeña mejora de LDA sobre GGA en Mo. Los cálculos también reproducen la evolución de las diferentes anomalías presentes en el espectro de bandas de dispersión fonónicas en función de x, tal como la anomalía de Kohn presente en Nb y que prácticamente desaparece para $x \approx 0.5$, llevando a la aparición de la depresión en H en Mo. También se observa claramente el reordenamiento de las frecuencias en N, desde Nb hasta Mo. A partir de la estructura electrónica y el espectro fonónico se determinan los elementos de matriz del acoplamiento electrón-fonón, los cuales son elementos de entrada para en la teoría de Eliashberg de la superconductividad [10, 146].

Para la función de Eliashberg $\alpha^2 F(\omega)$ de la aleación Nb-Mo encontramos una reducción generalizada y un corrimiento del espectro a frecuencias mayores conforme se incrementa la concentración de Mo hasta $x \approx 0.7$. Sin embargo, para $x = 1$ (Mo), el espectro se incrementa un poco nuevamente. Una vez obtenida esta información, calculamos y analizamos la evolución de la constante de acoplamiento $\lambda(x)$ y $T_c(x)$. La variación de $\lambda(x)$ sigue el comportamiento de la densidad de estados al nivel de Fermi $N(E_F)$, lo cual indica que la variación de $\lambda(x)$ es determinada predominantemente por $N(E_F)$ y, en un grado menor, por la variación del acoplamiento electrón-fonón. Finalmente, encontramos que los valores experimentales de $T_c(x)$ son reproducidos por los cáculos cuando utilizamos el esquema de interpolación para $\mu^*(x)$ propuesto por Gladstone *et al.* [156].

Para las aleaciones $Mg_{1-x}Al_xB_2$ y $MgB_{2(1-x)}C_{2x}$ los cálculos reproducen las tendencias observadas experimentalmente de los parámetros de red (a_0 y c_0), en estos casos también obtuvimos un mejor acuerdo de los cálculos GGA con los datos experimentales [35, 38–43]. Comparando los resultados con los métodos LAPW y MBPP, también en estos sistemas se obsevó un muy buen acuerdo entre ellos, indicando una implementación adecuada de la aproximación VCA en el MBPP para estas aleaciones ternarias.

En la estructura de bandas electrónicas de las aleaciones $Mg_{1-x}Al_xB_2$ y $MgB_{2(1-x)}C_{2x}$ observamos la aparición de dos ETT en la superficie de Fermi asociada a la banda σ, conforme se va aumentando la concentración de Al y C, respectivamente. La primera ETT ocurre cuando el fondo de la banda σ toca el nivel de Fermi, generan-

dose la transición de una superficie abierta a una cerrada, y la segunda se da cuando la banda está totalmente saturada, es decir, la superficie de Fermi correspondiente a la banda σ desaparece. Las concentraciones a las cuales ocurren estas transiciones son $x_{c1} = 0.26$ y $x_{c2} = 0.57$ para $Mg_{1-x}Al_xB_2$ y $x_{c1} = 0.117$ y $x_{c2} = 0.175$ para $MgB_{2(1-x)}C_{2x}$. Como se puede ver, las concentraciones críticas relacionadas con la saturación de la banda σ correlacionan con la pérdida de superconductividad en las aleaciones, lo cual ocurre para $x \geq 0.5$ en el sistema con Al [35–38] y se estima en $x \geq 0.15$ para el sistema con C [39, 40, 42, 43]. Esta correlación indica que la pérdida de superconductividad en estas aleaciones está íntimamente relacionada con la saturación de la banda σ.

Para ambas aleaciones $Mg_{1-x}Al_xB_2$ y $MgB_{2(1-x)}C_{2x}$ calculamos la evolución de la frecuencia fonónica del modo E_{2g} en función de x con las dos metodologías, LAPW y MBPP y cada una con los funcionales LDA y GGA. Encontramos que ambos métodos reproducen la fuerte renormalización de la frecuencia del modo E_{2g} observada experimentalmente [32, 52, 53] y además estando en buen acuerdo entre ellos, indicando que el VCA está correctamente implementado en el método MBPP. Aplicando LRT-MBPP, obtuvimos cálculos armónicos del espectro completo de dispersión fonónico para diferentes concentraciones en ambas aleaciones. Comparando el espectro calculado del MgB_2 con datos experimentales obtenidos mediante dispersión inelástica de rayos x (IXS) [164, 165], se observa un muy buen acuerdo, lo que indica que los efectos anarmónicos no juegan un papel importante en este material. La evolución del espectro de dispersión fonónicos en función de x se muestra en ambos sistemas una fuerte reducción de la dispersión de la banda relacionada con el modo E_{2g} a medida que x aumenta, hasta que la banda queda totalmente plana en concentraciones muy cercanas a las cuales la banda σ se satura por completo.

Para ambos sistemas $Mg_{1-x}Al_xB_2$ y $MgB_{2(1-x)}C_{2x}$ se calcularon $\alpha^2F(\omega)$ y λ aplicando el modelo de dos brechas superconductoras (σ π). A partir de $\alpha^2_{ij}F(\omega)$ y utilizando una expresión diagonal de la matriz para $\mu^*(\omega_c)$, se resolvieron las ecuaciones de brecha superconductora de Eliashberg en el modelo de dos bandas sin considerar el término de dispersión entrebandas. Encontramos muy buen acuerdo entre los resultados obtenidos para $\Delta_\sigma(x)$, $\Delta_\pi(x)$, y $T_c(x)$ con los datos experimentales correspondientes [45–48, 50, 51]. Es importante enfatizar que en ambos casos no observó el colapso de las dos brechas en una sola a ninguna concentración de Al o C. En base a estos resultados, podemos concluir que el término de dispersión entrebandas, en caso de estar presente, es pequeño y sus efectos sobre las propiedades superconductoras de las aleaciones $Mg_{1-x}Al_xB_2$ y $MgB_{2(1-x)}C_{2x}$ son despreciables comparado con el efecto del llenado de la banda σ.

Bibliography

[1] G.M. Eliashberg, *Sov. Phys. JETP* **11**, 696 (1960).

[2] P.B. Allen and R.C. Dynes, *Phys. Rev. B* **12**, 905 (1975).

[3] J.P. Carbotte, *Rev. Mod. Phys.* **62**, 1027 (1990).

[4] F. Marsiglio and J.P. Carbotte, *The Physics of Superconductors*, volume I. Conventional and High-T_c Superconductors (Springer-Verlag Berlin, Heidelberg, 2003), pp 231.

[5] E.L. Wolf, *Principles of Electronic Tunneling Spectroscopy* (Oxford University Press, New York, 1985).

[6] W.L. McMillan and J.M. Rowell, *Phys. Rev. Lett.* **14**, 108 (1965).

[7] P. Hohenberg and W. Kohn, *Phys. Rev.* **136**, B864 (1964).

[8] J.W. Kohn and L.J. Sham, *Phys. Rev.* **140**, A1133 (1965).

[9] S. Baroni, P. Giannozzi, and A. Testa, *Phys. Rev. Lett.* **58**, 1861 (1987).

[10] S.Y. Savrasov, D.Y. Savrasov, and O.K. Andersen, *Phys. Rev. Lett.* **72**, 372 (1994).

[11] S.Y. Savrasov and D.Y. Savrasov, *Phys. Rev. B* **54**, 16487 (1996).

[12] A.Y. Liu, *Phys. Stat. Sol. (b)* **217**, 419 (2000).

[13] J.K. Hulm and R.D. Blaugher, *Phys. Rev.* **123**, 1569 (1961).

[14] H.J. Goldschmidt and J.A. Brand, *J. Less-Common Metals.* **3**, 44 (1961).

[15] Landolt-Börnstein, III/21a, III/21b2 (Springer, Heidelberg, 1981), and references therein.

[16] Y. Nakagawa and A.D.B. Woods, *Phys. Rev. Lett.* **11**, 271 (1963).

[17] A.D.B. Woods and B.M. Powell, *Phys. Rev. Lett.* **15**, 778 (1965).

[18] B.M. Powell, P. Martel, and A.D.B. Woods, *Phys. Rev.* **171**, 727 (1968).

[19] C. Jiang, C. Wolverton, J. Sofo, L.Q. Chen, and Z.K. Liu, *Phys. Rev. B* **69**, 214202 (2004).

[20] E. Colavita, A. Franciosi, R. Rosei, F. Sacchetti, E.S. Giuliano, R. Ruggeri, and D.W. Lynch, *Phys. Rev. B* **20**, 4864 (1979).

[21] E. Donato, B. Ginatempo, E.S. Giuliano, R. Rugger, and A. Stancanell, *J. Phys. F: Met. Phys.* **12**, 2309 (1982).

[22] C.R. Bull, J. H. Kaiser, A. Alam, N. Shiotani, and R.N. West, *Phys. Rev. B* **29**, 6378 (1984).

[23] E. Bruno, B. Giantempo, E.S. Giuliano, A.V. Ruban, and Yu.Kh. Vekilov, *Phys. Rep.* **249**, 353 (1994).

[24] S. S. Rajput, R. Prasad, R.M. Singru, S. Kaprzyk, and A. Bansil, *J. Phys.: Condens. Matter* **8**, 2929 (1996).

[25] D.A. Papaconstantopoulos, E.N. Economou, B.M. Klein, and L.L. Boyer, *Phys. Rev. B* **20**, 177 (1979).

[26] M.J. Mehl, D.A. Papaconstantopoulos, and D.J. Singh, *Phys. Rev. B* **64**, 140509(R) (2001).

[27] O. De la Peña, A. Aguayo, and R. de Coss, *Phys. Rev. B* **66**, 012511 (2002).

[28] C. Ambrosch-Draxl, P. Süle, H. Auer, and E.Ya. Sherman, *Phys. Rev. B* **67**, 100505(R) (2003).

[29] T. Thonhauser and C. Ambrosch-Draxl, *Phys. Rev. B* **67**, 134508 (2003).

[30] J. Nagamatsu, N. Nakagawa, T. Muranaka, Y. Zanitai, and J. Akimitsu, *Nature* **410**, 63 (2001).

[31] Y. Kong, O.V. Dolgov, O. Jepsen, and O.K. Andersen, *Phys. Rev. B* **64**, 020501 (2001).

[32] K.P. Bohnen, R. Heid, and B. Renker, *Phys. Rev. Lett.* **86**, 5771 (2001).

[33] T. Yildirim, O.G. Iseren, J.W. Lynn, C.M. Brown, T.J. Udovic, Q. Huang, N. Rogado, K.A. Regan, M.A. Hayward, J.S. Slusky, T. He, M.K. Haas, P. Khalifah, K. Inumaru, and R.J. Cava, *Phys. Rev. Lett.* **87**, 037001 (2001).

[34] K. Kunc, I. Loa, K. Syassen, R.K. Kremer, and K. Ahn, *J. Phys.: Condens. Matter* **13**, 9945 (2001).

[35] J.S. Slusky, N. Rogado, K.A. Regan, M.A. Hayward, P. Khalifah, T. He, K. Inumaru, S.M. Loureiro, M.K. Hass, H.W. Zandbergen, and R.J. Cava, *Nature* **410**, 343 (2001).

[36] A. Bianconi, D. Di Castro, S. Agrestini, G. Campi, N.L. Saini, A. Saccone, S. De Negri, and M. Giovannini, *J. Phys.: Condens. Matter* **13**, 7383 (2001).

[37] P. Postorino, A. Congeduti, P. Dore, A. Nucara, A. Bianconi, D. Di Castro, S. De Negri, and A. Saccone, *Phys. Rev. B* **65**, 020507 (2002).

[38] H.D. Yang, H.L. Liu, M. X. Kuo, P.L. Ho, J.M. Chen, C.U. Jung, M.S. Park, and S.I. Lee, *Phys. Rev. B* **68**, 092505 (2003).

[39] T. Takenobu, T. Ito, D.H. Chi, K. Prassides, and Y. Iwasa, *Phys. Rev. B* **64**, 134513 (2001).

[40] R.A. Ribeiro, S.L. Bud'ko, C. Petrovic, and P.C. Canfield, *Physica C* **384**, 227 (2003).

[41] M. Avdeev, J.D. Jorgensen, R.A. Ribeiro, S.L. Bud'ko, and P.C. Canfield, *Physica C* **387**, 301 (2003).

[42] S.M. Kazakov, J. Karpinski, J. Jun, P. Geiser, N.D. Zhigadlo, R. Puzniak, and A.V. Mironov, *Physica C* **408**, 123 (2004).

[43] S. Lee, T. Masui, A. Yamamoto, H. Uchiyama, and S. Tajima, *Physica C* **397**, 7 (2003).

[44] R. S. Gonnelli, D. Daghero, A. Calzolari, G. A. Ummarino, V. Dellarocca, V. A. Stepanov, S.M. Kazakov, N. Zhigadlo, and J. Karpinski, *Phys. Rev. B* **71**, 060503R (2005).

[45] D. Daghero, D. Delaude, A. Calzolari, M. Tortello, G.A. Ummarino, R.S. Gonnelli, V.A. Stepanov, N. D. Zhigadlo, J. Karpinski, and A. Palenzona, cond-mat/0608029.

[46] T. Klein, L. Lyard, J. Marcus, C. Marcenat, P. Szabó, Z. Hol'anová, P. Samuely, B.W. Kang, H.J. Kim, H.S. Lee, H.K. Lee, and S.I. Lee, *Phys. Rev. B* **73**, 224528 (2006).

[47] P. Szabó, P. Samuely, Z. Pribulová, M. Angst, S. Bud'ko, P.C. Canfield, and J. Marcus, *Phys. Rev. B* **75**, 144507 (2007).

[48] R.S. Gonnelli, D. Daghero, G.A. Ummarino, M. Tortello, D. Delaude, V.A. Stepanov, and J. Karpinski, *Pysica C* **456**, 134 (2007).

[49] H. Schmidt, K.E. Gray, D.G. Hinks, J.F. Zasadzinski, M. Avdeev, J.D. Jorgensen, and J.C. Burley, *Phys. Rev. Lett.* **88**, 127002 (2002).

[50] Z. Hol'anová, P. Szabó, P. Samuely, R.H.T. Wilke, S.L. Bud'ko, and P.C. Canfield, *Phys. Rev. B* **70**, 064520 (2004).

[51] S. Tsuda, T. Yokoya, T. Kiss, T. Shimojima, S. Shin, T. Togashi, S. Watanabe, C. Zhang, C.T. Chen, S. Lee, H. Uchiyama, S. Tajima, N. Nakai, and K. Machida, *Phys. Rev. B* **72**, 064527 (2005).

[52] B. Renker, K.P. Bohnen, R. Heid, D. Ernst, H. Schober, M. Koza, P. Adelmann, P. Schweiss, and T. Wolf, *Phys. Rev. Lett.* **88**, 067001 (2002).

[53] D. Di Castro, S. Agrestini, G. Campi, A. Cassetta, M. Colapietro, A. Congeduti, A. Continenza, S. De Negri, M. Giovannini, S. Massidda, M. Nardone, A. Pifferi, P. Postorino, G. Profeta, A. Saccone, N.L. Saini, G. Satta, and A. Bianconi, *Europhys. Lett.* **58**, 278 (2002).

[54] O.K. Andersen, *Phys. Rev. B* **12**, 3060 (1975).

[55] D.D. Koelling and G.O. Arbman, *J. Phys. F: Metal Phys.* **5**, 2041 (1975).

[56] D.J. Singh, *Plane Waves, Pseupotentials and the LAPW Method* (Kluwer Academic Publishers, Boston, 1994).

[57] P. Blaha, K. Schwarz, G.K.H. Madsen, D. Kvasnicka, and J. Luitz, *WIEN2k, An Augmented Plane Wave + Local Orbitals Program for Calculating Crystal Properties*, ISBN 3-9501031-1-2 (Karlheinz Schwarz, Techn. Universität Wien, Austria, 2001).

[58] B. Meyer, C. Elsässer, and M. Fähnle, FORTRAN90 Program for Mixed-Basis Pseudopotential Calculations for Crystals, Max-Planck-Institut für Metallforschung, Stuttgart (unplublished).

[59] S.G. Louie, K.M. Ho, and M.L. Cohen, *Phys. Rev. B* **19**, 1774 (1979).

[60] P. Giannozzi, S. de Gironcoli, P. Pavone, and S. Baroni, *Phys. Rev. B* **43**, 7231 (1991).

[61] R. Heid, K.P. Bohnen, and K.M. Ho, *Phys. Rev. B* **57**, 7407 (1999).

[62] R. Heid and K.P. Bohnen, *Phys. Rev. B* **60**, R3709 (1999).

[63] A.Y. Liu, I.I. Mazin, and J. Kortus, *Phys. Rev. Lett.* **87**, 087005 (2001).

[64] A.A. Golubov, J. Kortus, O.V. Dolgov, O. Jepsen, Y. Kong, O.K. Andersen, B.J. Gibson, K. Ahn, and R.K. Kremer, *J. Phys.: Condens. Matter* **14**, 1353 (2002).

[65] L.H. Thomas, *Proc. Cambridge Phil. Soc.* **23**, 542 (1927).

[66] E. Fermi, *Z. Physik* **48**, 73 (1928).

[67] P. Gombás, *Die stische Theorie des Atoms und hre Anwendungen* (Springer, Vienna, 1949).

[68] J.C. Slater, *Phys. Rev.* **81**, 385 (1951).

[69] R. Gàspàr, *Acta Phys. Acad. Sci. Hung.* **3**, 263 (1954).

[70] L. Hedin and B.I. Lundqvist, *J. Phys. C: Solid St. Phys.* **4**, 2074 (1971).

[71] J.P. Perdew and Y. Wang, *Phys. Rev. B* **45**, 13244 (1992).

[72] A. Dal Corso, A. Pasquarello, A. Baldereschi, and R. Car, *Phys. Rev. B* **53**, 1180 (1996).

[73] J.E. Jaffe, Z. Lin, and A.C. Hess, *Phys. Rev. B* **57**, 11834 (1998).

[74] C. Stampfl and C.G. Van de Walle, *Phys. Rev. B* **59**, 5521 (1999).

[75] F. Favot and A. Dal Corso, *Phys. Rev. B* **60**, 11427 (1999).

[76] C. Stampfl, W. Mannstadt, R. Asahi, and A.J. Freeman, *Phys. Rev. B* **63**, 155106 (2001).

[77] A. Janotti, S.H. Wei, and D.J. Singh, *Phys. Rev. B* **64**, 174107 (2001).

[78] F. Herman, J.P. Van Dyke, and I.P. Ortenburger, *Phys. Rev. Lett.* **22**, 807 (1962).

[79] P.S. Svendsen and U. von Barth, *Phys. Rev. B* **54**, 17402 (1996).

[80] J.P. Perdew and K. Burke, *Int. J. Quant. Chem.* **57**, 309 (1996).

[81] J.P. Perdew, K. Burke, and M. Ernzerhof, *Phys. Rev. Lett.* **77**, 3865 (1996).

[82] J.C. Slater, *Phys. Rev. B* **51**, 846 (1937).

[83] J.C. Slater, *Adv. Quan. Chem.* **1**, 25 (1964).

[84] D. Singh, *Phys. Rev. B* **43**, 6388 (1991).

[85] C. Elsässer, N. Takeuchi, K.M. Ho, C.T. Chan, P. Braun, and M. Fähnle, *J. Phys.: Condens. Matter* **2**, 4371 (1990).

[86] K.M. Ho, C. Elsässer, C.T. Chan, and M. Fähnle, *J. Phys.: Condens. Matter* **4**, 5189 (1992).

[87] J.C. Phillips and L. Kleinman, *Phys. Rev.* **116**, 287 (1959).

[88] M.L. Cohen and V. Heine, *Solid State Physics* **24**, 37 (1970).

[89] J. Ihm, A. Zunger, and M.L. Cohen, *J. Phys. C: Solid State Phys.* **12**, 4409 (1979).

[90] R.M. Martin, *Electronic Structure: Basic Theory and Practical Methods* (Cambridge University Press, United Kingdom, 2004).

[91] W.C. Topp and J.J. Hopfield, *Phys. Rev. B* **7**, 1295 (1974).

[92] T. Starkloff and J.D. Joannopoulos, *Phys. Rev. B* **16**, 908 (1977).

[93] D. Vanderbilt, *Phys. Rev. B* **32**, 8412 (1985).

[94] C.L. Fu and K.M. Ho, *Phys. Rev. B* **28**, 5480 (1983).

[95] M. Born and K. Huang, *Dynamical Theory of Crystal Lattices* (Oxford University Press, Oxford, 1954).

[96] P.D. De Cicco and F.A. Johnson, *Proc. R. Soc. London* **A310**, 111 (1969).

[97] R. Pick, M.H. Cohen, and R.M. Martin, *Phys. Rev. B* **1**, 910 (1970).

[98] E.N. Zein, *Phys. Lett. A* **161**, 526 (1992).

[99] S. Baroni, S. Gironcoli, and A. Dal Corso, *Rev. of Mod. Phys.* **73**, 515 (2001).

[100] M. Born and J.R. Oppenheimer, *Ann. Phys.* **84**, 457 (1927).

[101] H. Hellmann, *Einführung in die Quantenchemie* (Deuticke, Leipzing, 1937).

[102] R.P. Feynmann, *Phys. Rev.* **56**, 340 (1939).

[103] S.S. Rosenblum, W.H. Weber, and B.L. Chamberland, *Phys. Rev. B* **56**, 8412 (1997).

[104] K.P. Bohnen, R. Heid, O. De la Peña-Seaman, B. Renker, P. Adelmann, and H. Schober, *Phys. Rev. B* **75**, 092301 (2007).

[105] H. Over, Y.D. Kim, A.P. Seitsonen, S. Wendt, E. Lundgren, M. Schmid, P. Vagra, A. Morgante, and G. Ertl, *Science* **287**, 1474 (2000).

[106] K.M. Ho, C.L. Fu, B.N. Harmon, W. Weber, and D.R. Hamann, *Phys. Rev. Lett.* **49**, 673 (1982).

[107] Y. Chen, C.L. Fu, K.M. Ho, and B.N. Harmon, *Phys. Rev. B* **31**, 6775 (1985).

[108] D. Singh and H. Krakauer, *Phys. Rev. B* **43**, 1441 (1991).

[109] H.K. Onnes, *Comm. Leiden* **120b** (1911).

[110] W. Meissner and R. Ochsenfeld, *Naturwiss.* **21**, 787 (1933).

[111] C.J. Gorter, *Nature* **132**, 931 (1933).

[112] E. Maxwell, *Phys. Rev.* **78**, 477 (1950).

[113] C.A. Reynolds, B. Serin, W.H. Wright, and L.B. Nesbitt, *Phys. Rev.* **78**, 487 (1950).

[114] H. Fröhlich, *Phys. Rev.* **79**, 845 (1950).

[115] J. Bardeen, L.N. Cooper, and J.R. Schrieffer, *Phys. Rev.* **106**, 162 (1957).

[116] J. Bardeen, L.N. Cooper, and J.R. Schrieffer, *Phys. Rev.* **108**, 1175 (1957).

[117] L.P. Gor'kov, *Sov. Phys. JETP* **7**, 505 (1958).

[118] I. Giaever, *Phys. Rev. Lett.* **5**, 464 (1960).

[119] J.M. Rowell, P.W. Anderson, and D.E. Thomas, *Phys. Rev. Lett.* **10**, 334 (1963).

[120] J.M. Ziman, *Electrons and Phonons* (Oxford University Press, Oxford, 2003).

[121] W.L. McMillan, *Phys. Rev. B* **167**, 331 (1968).

[122] K.P. Bohnen, R. Heid, and B. Renker, *Adv. in Sol. State Phys.* **42**, 293 (2002).

[123] H.J. Choi, D. Roundy, H. Sun, M.L. Cohen, and S.G. Louie, *Nature* **418**, 758 (2002).

[124] W. Pickett, *Nature* **418**, 733 (2002).

[125] M. Iavarone, G. Karapetrov, A.E. Koshelev, W.K. Kwok, G.W. Crabtree, D.G. Hinks, W. N. Kang, E. Choi, H.J. Kim, H. Kim, and S.I. Lee, *Phys. Rev. Lett.* **89**, 187002 (2002).

[126] A. Floris, G. Profeta, N.N. Lathiotakis, M. Lüders, M.A. Marques, C. Franchini, E.K. Gross, A. Continenza, and S. Massidda, *Phys. Rev. Lett.* **94**, 037004 (2005).

[127] J. Geerk, R. Schneider, G. Linker, A.G. Zaitsev, R. Heid, K.P. Bohnen, and H.v. Löhneysen, *Phys. Rev. Lett.* **94**, 227005 (2005).

[128] J.A. Catterall and S.M. Barker, *Plansee Proceedings* p. 577 (1964).

[129] P. Bujard, R. Sanjines, E. Walker, J. Ashkenazi, and M. Peter, *J. Phys. F: Met. Phys.* **11**, 775 (1981).

[130] R. de Coss, A. Aguayo, and G. Murrieta, *Mat. Res. Soc. Symp. Proc.* **646**, N5.33.1 (2001).

[131] R.L. Cappelletti, N. Wakabayashi, W.A. Kamitakahara, J.G. Traylor, and A.J. Bevolo, *Phys. Rev. B* **25**, 6096 (1982).

[132] W.C. Hubbell and F.R. Brotzen, *J. Appl. Phys.* **43**, 3306 (1972).

[133] P.C. Camargo, F.R. Brotzen, and S. Steinemann, *Phys. F: Met. Phys.* **17**, 1065 (1987).

[134] J. Ashkenazi, M. Dacorogna, M. Peter, Y. Talmor, E. Walker, and S. Steinemann, *Phys. Rev. B* **18**, 4120 (1978).

[135] W.M. Lomer, *Proc. Phys. Soc. (London)* **80**, 489 (1962).

[136] L.F. Mattheiss, *Phys. Rev.* **139**, A1893 (1965).

[137] T.L. Loucks, *Phys. Rev.* **139**, A1181 (1965).

[138] C.M. Varma and W. Weber, *Phys. Rev. B* **19**, 6142 (1979).

[139] J. Zarestky, C. Stassis, B.N. Harmon, K.M. Ho, and C.L. Fu, *Phys. Rev. B* **28**, 697 (1983).

[140] J. Bostock, V. Diadiuk, W.N. Cheung, K.H. Lo, R.M. Rose, and M.L.A. MacVicar, *Phys. Rev. Lett.* **11**, 603 (1976).

[141] R. Bauer, A. Schmid, P. Pavone, and D. Strauch, *Phys. Rev. B* **57**, 11276 (1998).

[142] C.M. Perlov and C.Y. Fong, *Phys. Rev. B* **29**, 1243 (1984).

[143] D.D. Koelling and B.N. Harmon, *J. Phys. C: Solid State Phys.* **10**, 3107 (1977).

[144] V. Ozolins and M. Korling, *Phys. Rev. B* **48**, 18304 (1993).

[145] K. Kokko and M.P. Das, *J. Phys.: Condens. Matter* **10**, 1285 (1998).

[146] R. Heid, L. Pintschovius, W. Reichardt, and K.P. Bohnen, *Phys. Rev. B* **61**, 12059 (2000).

[147] F. Birch, *Phys. Rev.* **71**, 809 (1947).

[148] W. DeSorbo, *Phys. Rev. B* **130**, 2177 (1963).

[149] N. Wakabayashi, *Phys. Rev. B* **33**, 6771 (1986).

[150] J. Zarestky, C. Stassis, B.H. Harmon, K.M. Ho, and C.L. Fu, *Phys. Rev. B* **28**, 697 (1983).

[151] G.B. Arnold, J. Zasadzinski, and E.L. Wolf, *Phys. Lett.* **69A**, 136 (1978).

[152] E.L. Wolf, J. Zasadzinski, J.W. Osmun, and G.B. Arnold, *J. Low Temp. Phys.* **40**, 19 (1980).

[153] J. Geerk, M. Gurvitch, D.B. McWhan, and J.M. Rowell, *Physica C* **109**, 1775 (1982).

[154] M.J. Bostock, M.L.A. MacVicar, G.B. Arnold, J. Zasadzinki, and E.L. Wolf, *Proceedings of the Third International Conference on Superconductivity of d- and f-Band Metals* (edited by H. Suhl and M.B. Mapple, Academic Press, New York, 1980), pp 153.

[155] G.W. Crabtree, D.H. Dye, D.P. Karim, and D.D. Koelling, *Phys. Rev. Lett.* **42**, 390 (1979).

[156] G. Gladstone, M. A. Jensen, and J. R. Schrieffer, *Superconductivity* (Ed. R.D. Parks, New York, Dekker, 1969), pp 665, vol. 2.

[157] C. Buzea and T. Yamashita, *Superc. Sci. Technol.* **14**, R115 (2001).

[158] J. An and W.E. Pickett, *Phys. Rev. Lett.* **86**, 4366 (2001).

[159] J. Kortus, I.I. Mazin, K.D. Belashchenko, V.P. Antropov, and L.L. Boyer, *Phys. Rev. Lett.* **86**, 4656 (2001).

[160] I.I. Mazin and V.P. Antropov, *Physica C* **385**, 49 (2003).

[161] A.Q.R. Baron, H. Uchiyama, S. Tsutsui, Y. Tanaka, D. Ishikawa, , J.P. Sutter, S. Lee, S. Tajima, R. Heid, and K.P. Bohnen, *Physica C* **456**, 83 (2007).

[162] A. Floris, A. Sanna, M. Lüders, G. Profeta, N.N. Lathiotakis, M.A.L. Marques, C. Franchini, E.K.U. Gross, A. Continenza, and S. Massidda, *Physica C* **546**, 45 (2007).

[163] J. Kortus, *Physica C* **546**, 54 (2007).

[164] A. Shukla, M. Calandra, M. d'Astuto, M. Lazezeri, F. Mauri, C. Bellin, M. Krisch, J. Karpinsky, S.M. Kazakov, J. Jun, D. Daghero, and K. Parlinski, *Phys. Rev. Lett.* **90**, 095506 (2003).

[165] A.Q.R. Baron, H. Uchiyama, Y. Tanaka, S. Tsutsui, D. Ishikawa, S. Lee, R. Heid, K.P. Bohnen, S. Tajima, and T. Ishikawa, *Phys. Rev. Lett.* **92**, 197004 (2004).

[166] A.F. Goncharov, V.V. Struzhkin, E. Gregoryanz, J. Hu, R.J. Hemley, H.K. Mao, G. Lapertot, S.L. Bud'ko, and P.C. Canfield, *Phys. Rev. B* **64**, 100509 (2001).

[167] J. Hlinka, I. Gregova, J. Pokrny, A. Plecenik, P. Kus, L. Satrapinsky, and S. Benacka, *Phys. Rev. B* **64**, 140503R (2001).

[168] J.W. Quilty, S. Lee, A. Yamamoto, and S. Tajima, *Phys. Rev. Lett.* **88**, 087001 (2002).

[169] H.J. Choi, M.L. Cohen, and S.G. Louie, *Physica C* **385**, 66 (2003).

[170] M. Calandra, M. Lazzeri, and F. Mauri, *Physica C* **456**, 38 (2007).

[171] Y. Wang, T. Plackowski, and A. Junod, *Physica C* **355**, 179 (2001).

[172] F. Bouquet, R.A. Fisher, N.E. Phillips, D.G. Hinks, and J.D. Jorgensen, *Phys. Rev. Lett.* **87**, 047001 (2001).

[173] H.D. Yang, J.Y. Lin, H.H. Li, F.H. Hsu, C.J. Liu, S.C. Li, R.C. Yu, and C.Q. Jin, *Phys. Rev. Lett.* **87**, 167003 (2001).

[174] P. Szabó, P. Samuely, J. Kačmarčík, T. Klein, J. Marcus, D. Fruchart, S. Miraglia, C. Marcenat, and A.G.M. Jansen, *Phys. Rev. Lett.* **87**, 137005 (2001).

[175] F. Giubileo, D. Roditchev, W. Sacks, R. Lamy, D.X. Thanh, and J. Klein, *Phys. Rev. Lett.* **87**, 177008 (2001).

[176] X.K. Chen, M.J. Konstantinovi, J.C. Irwin, D.D. Lawrie, and J.P. Franck, *Phys. Rev. Lett.* **87**, 157002 (2001).

[177] S. Tsuda, T. Yokoya, T. Kiss, Y. Takano, K. Togano, H. Kito, H. Ihara, and S. Shin, *Phys. Rev. Lett.* **87**, 177006 (2001).

[178] E. Bascones and F. Guinea, *Phys. Rev. B* **64**, 214508 (2001).

[179] F. Bouquet, Y. Wang, R.A. Fisher, D.G. Hinks, J.D. Jorgensen, A. Junod, and N.E. Phillips, *Europhys. Lett.* **56**, 856 (2001).

[180] O. De la Peña Seaman, *Estudio de las propiedades estructurales y electrónicas de aleaciones superconductoras basadas en el MgB$_2$*, Master's thesis, Departamento de Física Aplicada, Cinvestav-Mérida (2004).

[181] J. Kortus, O.V. Dolgov, R.K. Kremer, and A.A. Golubov, *Phys. Rev. Lett.* **94**, 027002 (2005).

[182] H. Schmidt, J. F. Zasadzinski, K.E. Gray, and D.G. Hinks, *Phys. Rev. Lett.* **88**, 127002 (2002).

[183] G.A. Ummarino, R.S. Gonnelli, and A. Bianconi, *J. of Supercond.: Inc. Novel Magnetism* **18**, 791 (2005).